UNVEILING THE PHOTOPHYSICS IN SOLID-STATE ORGANIC MATERIALS:

A STUDY ON BODIPY, PORPHYRIN, AND PBI BASED MATERIALS

by

Alexander James King

A dissertation submitted in partial fulfillment
of the requirements for the degree

of

Doctor of Philosophy

in

Materials Science

MONTANA STATE UNIVERSITY
Bozeman, Montana

May 2024

DEDICATION

I want to dedicate this document to all of the people in my life who have helped me fulfill my dream of becoming a scientist and my sixteen-year-old self for falling in love with the mathematical connection to the physical world.

ACKNOWLEDGEMENTS

I would like to thank my family for inadvertently pushing me to be a chemist and to pursue my dreams. I would like to dedicate this document to my former boss Sunil Upadhayay who truly thought I could become more than just a bench-top chemist even at the cost of losing a colleague. I would like to thank my past scientific mentors, Doctor Hannah Rhoda, Doctor Viktor Nemykin, Doctor Paul Kiprof, and Doctor Steven Berry. I would like to thank Lauren Hines who was a great friend and support to me throughout my early years of this Ph.D. program, especially during COVID-19 and the emotional and mental toll that time took. I would like to thank Erik Grumstrup for his mentorship and guidance over the past five years. Finally, I would like to thank Kathryn Rose Zimlich. She has been such a support during my time here at MSU and deserves so much recognition for her emotional support and scientific contributions.

TABLE OF CONTENTS

TABLE OF CONTENTS CONTINUED

TABLE OF CONTENTS CONTINUED

LIST OF TABLES

Table Page

LIST OF FIGURES

Figure Page

LIST OF FIGURES CONTINUED

Figure Page

LIST OF FIGURES CONTINUED

Figure Page

LIST OF FIGURES CONTINUED

Figure Page

LIST OF FIGURES CONTINUED

Figure Page

ABSTRACT

Organic semiconductors have applications in optoelectronics, light harvesting, and sensing as soft matter materials. One of the biggest challenges to overcome with organic-based materials is structural heterogeneity that arises from the self-assembly of monomers upon solid-state deposition. In this work we have investigated solid-state organic semiconductors with three levels of solution-phase processing: i) materials prepared from drop casting with no solution-phase processing on BODIPY systems ii) films prepared from pre-aggregation of the monomers with porphyrin systems iii) films prepared from aggregated monomers that were covalently stapled with perylene bisimide systems. In the BODIPY systems, we found that: i) the electronic states are highly coupled with a major redshift from 583 nm in the solution to 614 nm in the solid. ii) Through interpretation of the broadband transient absorption spectrum, the initial excited state is delocalized and localizes within the first 10 femtoseconds. iii) Using two color pump probe, we measured ultrafast diffusion at 14.37 ± 2.79 cm^2s^{-1} that abruptly halts after 10 ps. In the porphyrin systems with level 2 solution-phase processing, we have also shown that the lifetime of the excited state is correlated with the degree of structural order. The monomer exhibits the longest lifetime with an average lifetime of 1.26 ns, the aggregate is much shorter with a lifetime of 349 ps, and the films show substantially faster relaxation, with the film fabricated from the monomer having a 72.56 ps average lifetime, and the film composed of the aggregate having a 26 ps average lifetime. These results suggest that the lifetime decreases as the order and electronic coupling of the system increases, so much so that the lifetime is two orders of magnitude different. In the perylene bisimide systems, we did a direct spectroscopic comparison between thin films formed from noncovalent assemblies and from covalently tethered molecular assemblies. This indicates that interchromophore coupling is enhanced in the covalently tethered film. We saw a 73% increase in excited state transport compared to the control film, as well as a shorter and more homogenous excited state lifetime. Covalent tethering proves to be the best strategy for generating homogeneous materials.

CHAPTER ONE

INTRODUCTION

Nature has evolved photosystems over billions of years in flora to efficiently convert photonic energy from the sun into chemical energy.[1] With just a fraction of the time plants have had to evolve, replication of a plant's photosystem through molecular design has been met with limited success. Synthetic approaches for creating organic materials often result in structurally and electronically ill-defined domains, as compared to the robust spatial organization of photosystem biochemical complexes.[2] Artificial photosynthetic systems heavily rely on the bottom-up self-assembly synthetic method that is driven by noncovalent interactions and solvophobic forces,[3] leading to significant structural heterogeneity, poor energy transport, and unpredictability in the final structure.[4-7] Although there are deposition techniques to mitigate the problems that arise from bottom-up self-assembly,[8-10] the most promising work on producing homogeneous structures is semicrystalline at best upon solid-state deposition.[11]

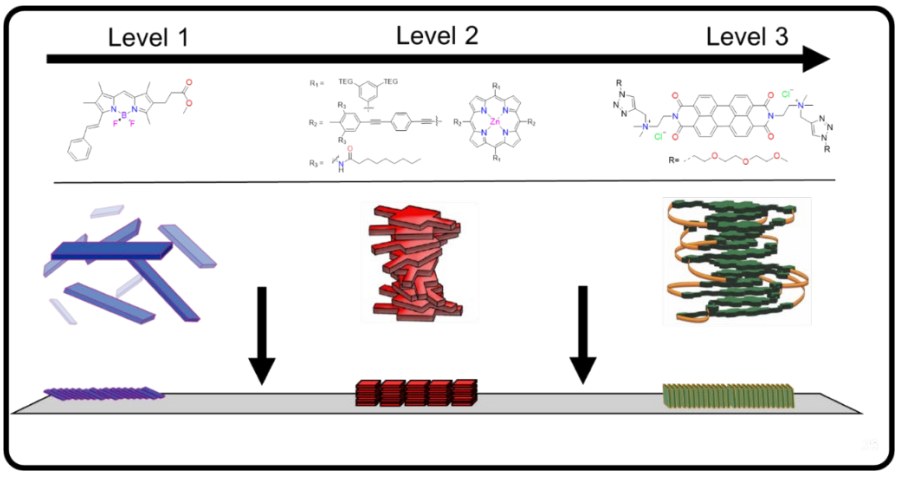

Figure 1.1: Three levels of solution-phase processing prior to solid-state deposition.

To elucidate the structure-function relationship of heterogeneity and its impact on excited state dynamics in organic semiconducting materials, we have designed a systematic approach for achieving homogeneous materials. These methods are described as three levels of solution-phase processing techniques prior to solid-state deposition (fig 1.1). At level 1 there is no solution-phase processing. Level 2 consists of treating the dissolved monomers with an antisolvent to force the monomers into aggregation. At level 3, the aggregate is covalently stapled together, locking the aggregate's conformation and orientation. Because of the synthetic challenges of covalently stapling and aggregation, we have selected three families of molecules to study the three levels.

This chapter discusses the necessary background information to understand structural disorder, electronic coupling, and transport mechanisms in organic materials. The second chapter focuses on the experimental techniques used to study organic materials and correlate heterogeneity with ultrafast photophysical properties. In the third chapter, we investigated a *bo*ron *dipy*rromethene (BODIPY) molecule that was crystallized using a simple drop cast method, which resulted in ordering purely from self-assembly upon solvent evaporation; this corresponds to level 1 as described above. The fourth chapter focuses on the pre-aggregation of a zinc porphyrin (PZn) molecule in the solid-state and solution-phase; processing level 2. Finally, the fifth chapter focuses on the solid-state properties of *p*erylene *b*is*i*mide (PBI) assemblies that were pre-aggregated in solution, and then chemically locked in place to lock in the final structure; processing level 3.

Using ultrafast microscopies and spectroscopies, we were able to characterize the structural heterogeneity that arises from drop casting organic materials. In an attempt to mitigate structural heterogeneity, we devised a systematic approach to solution-phase processing before solid-state deposition. Of the three levels described above, level 3 (corresponding to covalently locking

monomers into an aggregate) is the most effective at reducing the structural and energetic heterogeneity in thin film materials. To improve the homogeneity of solid-state organic materials, solution-phase processing such as pre-aggregation or covalent locking is recommended.

Background

1.1: Effects of Disorder in Organic Materials

The overarching theme of this dissertation is to study and document the effects of disorder imposed via drop casting methods in organic semiconductors. In molecular solids, the distribution of orbital energies across the system is referred to as global energetic disorder.[12] Examples of thermally driven conformational disorder that fluctuate over time include methyl rotations,[13] hydrogen bonding,[14] and dipole orientation.[15] These examples are known as dynamical disorder.[16] The effective energetic landscape affects excited state dynamics and transport in cases where the electronic coupling is high (J- and H-type coupling)[17-19] and thus dynamical disorder must be considered when designing functional organic materials.

Static, or structural disorder, can also significantly impact the excited state functionality and is often introduced during solid-state deposition. Drop casting remains one of the cheapest and most time-efficient techniques to deposit molecular precursors.[20] This method involves taking a solution that contains dissolved or suspended particles and "dropping" the solution onto the surface of a substrate. The solvent (or dispersant) evaporates creating a "coffee ring" pattern, as first interpreted by Deegan.[21] Even though the evaporation processes lead to a highly complex formation that is dependent on concentration, evaporation rate, height, radius, and contact angle of the solvent droplet, a majority of crystallites and microstructures are deposited at the forefront

of solvent evaporation. Thus, this method induces significant irreproducible structural heterogeneity.

The function of organic semiconductors is impacted by structural heterogeneity but often the extent of it is not clear. Most characterization techniques measure bulk properties such as conductivity/charge mobility,[22] photo-conversion-efficiency,[23] and a multitude of spectroscopies.[24] These bulk measurements do give insight into material properties but fail to capture the microscopic effects of structural heterogeneity. Utilizing ultrafast microscopies and spectroscopies, we were able to probe smaller spatial scales that bulk measurements fail to resolve. With higher spatial resolution, the microscopic photophysics of organic materials can be directly correlated to structural heterogeneity that is formed by drop casting methods. In the next section, we will discuss the effects of structural order (or disorder) of the molecules and the implications on material energetics.

1.2: Electronic Coupling

Couplings of individual molecular chromophores that occur upon aggregation can result in new electronic functionalities such as long-range energy transport. This coupling occurs through multiple molecular transition dipole moments and is mediated through entropy and van der Waals forces, altering the energetic domain of the monomeric chromophore.[25] In specific synthetic conditions that are regulated by the solvent environment, molecular chromophores will tend to arrange themselves in a noncovalently bound structure to achieve a minimum energy configuration, i.e., a molecular aggregate. Due to the energy stabilization of the molecules in the aggregate, the molecules develop coherent transition dipole moments, and the electronic

excitations are extended over multiple molecules to form delocalized Frenkel excitons, as first reported by Kasha et al.[26]

In ideal cases, aggregation can generally be broken down into two categories: J-type and H-type aggregates. The two classifications of aggregates originate from their spectral shifts relative to the monomer absorption spectrum: a bathochromic shift for J-aggregates and a hypsochromic shift with depletion in the emission shift for H-aggregates.[27] The discovery of J-type aggregation was independently reported by Edwin E. Jelley in 1936 (whom the classification was named after)[28] and Von. G Schiebe in 1938.[29] Although H-aggregation was well described by Kasha's exciton model in 1963,[26] it wasn't until 1970 that publications around synthetic H-aggregates started to emerge.[30, 31]

1.2.1: The Nature of Excitonic Coupling in Aggregates.

The theoretical description of coherent coupling and transport between aggregated monomers was spearheaded by Spano et al. and was built from the foundation of J-type and H-type couplings.[32] In the most ideal cases, when the molecular transition dipole moments of coupled molecules are aligned parallel to each other, the resulting coupling is destabilized, increasing the energy of the transition. When the molecular transition dipole moments are aligned perpendicular to each other, the coupling is stabilized, resulting in a lower energy transition which gives rise to the changes in the absorption spectra for J- and H-type aggregates.

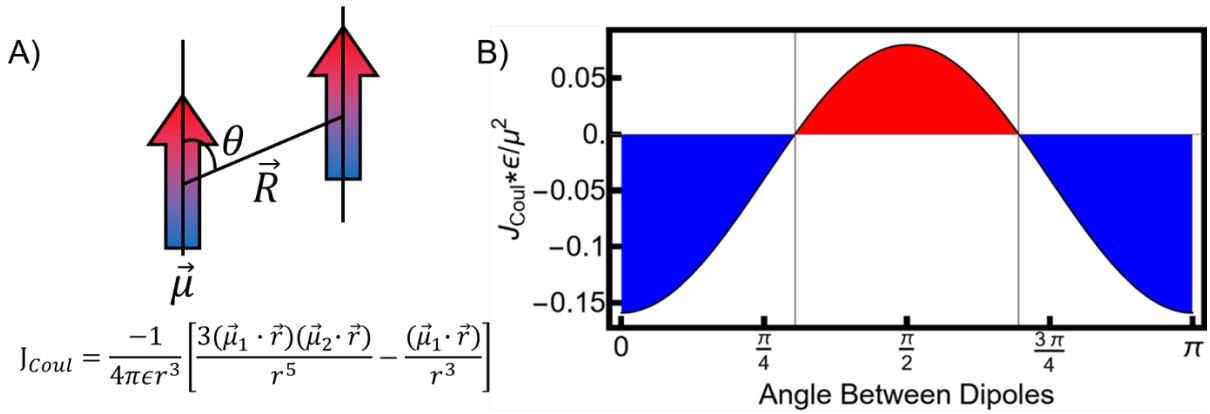

Figure 1.2.1: A) The relative orientation of transition dipole moments Coupling energy, J_{Coul}, of two point-dipoles as a function of the angle from eq. 1.1. B) The region in blue is representative of J-aggregates and the red region is representative of H-aggregates.

To further describe the spectral shifts, we can turn to Kasha's model to understand how the spatial dependence of the monomers impacts the absorption spectrum. This model considers the long-range Coulomb coupling between *N* chromophores that can be approximated by treating the chromophores as point-dipoles[33] (fig. 1.2.1A). Here, the interaction between any two dipoles (μ) can be described by their separation distance (*R)*, and their relative orientation angle (θ). The dipole coupling energy (J_{Coul}) can be calculated using the vector form (in Fig. 1.2.1 A) or as follows:

$$J_{Coul} = \frac{\mu^2(1-3cos^2(\theta))}{4\pi\epsilon R^3}. \qquad \textit{eq. 1.1}$$

In the simplest cases where distance *R* is fixed, the coupling energy can easily be described as a function of the angle between the dipoles. Figure 1.2.1B depicts the energy as a function of angle; when the dipoles are aligned vertically, head-to-tail (θ = 0, π), the coupling energy becomes negative and coupling is J-like (blue region), whereas if they are aligned side-by-side ($\theta = \pi/2$), the coupling energy becomes positive, and the coupling is considered H-like (red region).

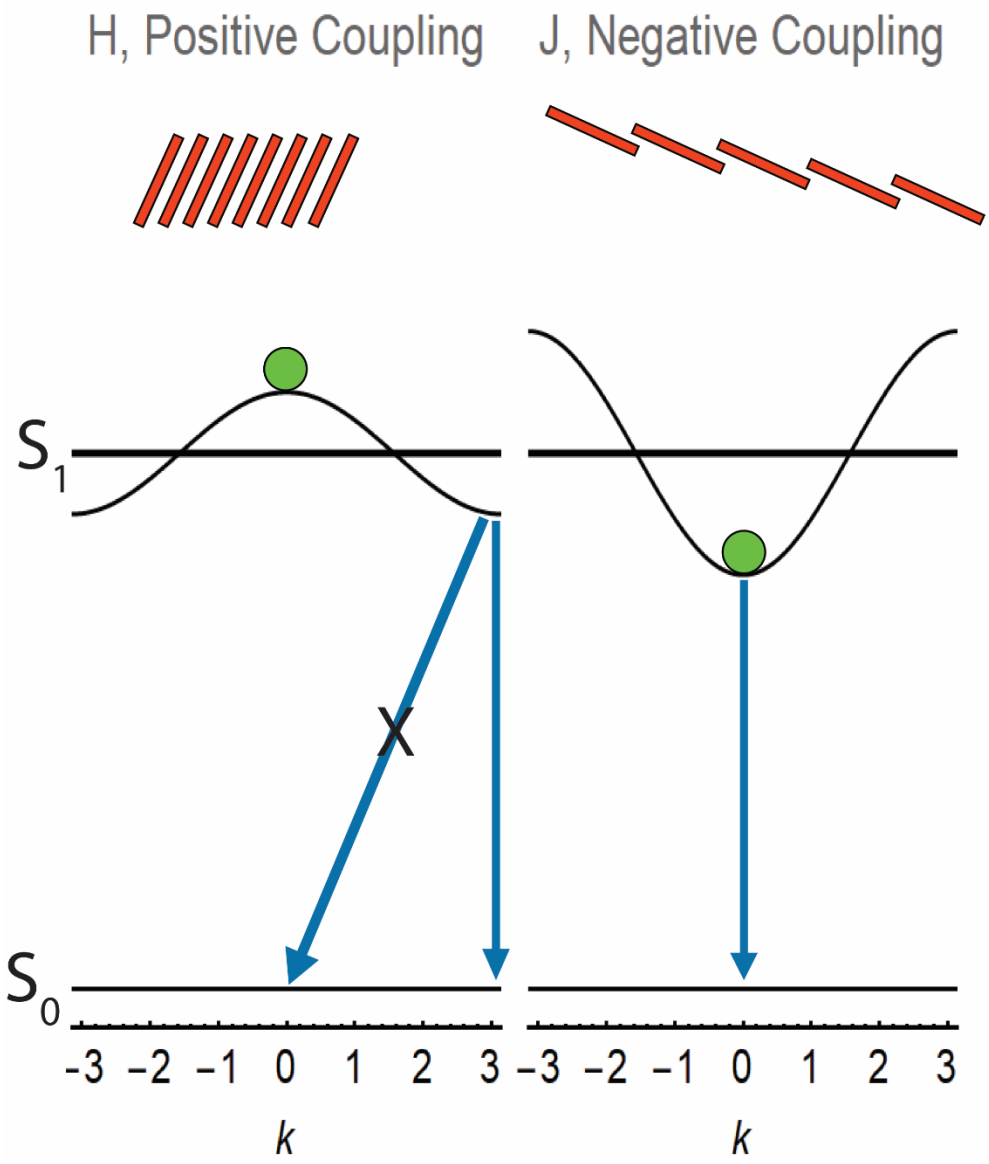

Figure 1.2.2: Kasha's model for the energic landscape of H- (right) and J- (left) aggregates. The arrows denote that in J-aggregates the relaxation is optically allowed, while in H-aggregates the relaxation is optically forbidden.

The energetic landscape of the aggregate is strongly dependent on the dipole coupling energy term, J_{Coul}. In Kasha's model for molecular aggregates, the energy of the first excited state, E_{S1}, is perturbed by multiple dipole-dipole transitions.[33-35] The total excited perturbation energy

(E) of the aggregate is defined as the energy of the first excited state of the monomer perturbed by the wave vector (k) and the dipole coupling energy ($2J_{coul}\cos(k)$):

$$E = E_{S1} + 2J\cos(k) \qquad k = 0, \pm\frac{2\pi}{N}, \pm\frac{4\pi}{N} \ldots \pi, \qquad \textit{eq. 1.2}$$

where k is the wave vector that depends on the number of monomers, N. J-aggregates are defined when the monomers are aligned "head-to-tail", and the perturbation energy becomes negative relative to E_{S1} (at k=0). H-aggregates are defined when the monomers are aligned "side-by-side", and the perturbation energy becomes positive relative to E_{S1} (at k=0). In J-aggregates, at k=0 there is a local minimum in the energy landscape, thus after excitation, the excited state is optically allowed to relax to the ground state. H-aggregates have a local maximum at k=0 and due to Kasha's rule, the exciton must relax to the band edge before relaxing back down to the ground state, thus making the relaxation optically forbidden (fig. 1.2.2).[33]

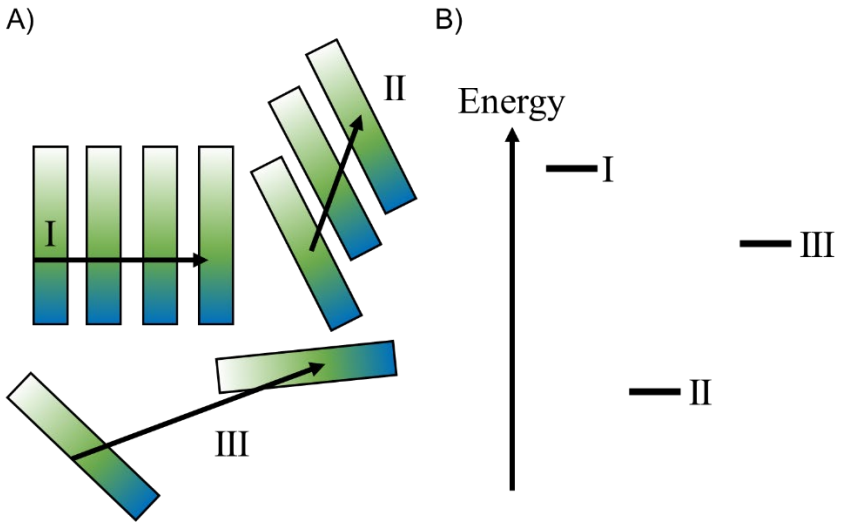

Figure 1.2.3: A cartoon representation of heterogeneous crystallized monomers in a drop cast material (A) and the corresponding energies of regions within the figure (B).

From the discussion above, the energy of the first excited state heavily relies on i) the distance of the monomers, ii) the angle between the monomers, and iii) N number of repeating monomers. In an imaginary scenario, where we have a region of molecular crystals in a drop cast material, there exist molecular orientations that are ordered H-like, J-like, and isolated monomers with no order, as depicted in Figure 1.2.3 A. Moving along region I in this figure, the coupling of the monomer spanning four units is H-like, region II corresponds to J-like coupling with three monomer units, and finally region III has little coupling between the monomers as there are no repeating monomers, and the distance/angle between the two monomers has minor contribution to the coupling term. In this imaginary scenario, all three regions will have their own localized energies that are very different from each other (fig. 1.2.3.B). Although this thought experiment does not capture every coupling interaction that is possible, it is evident that just from equations 1.1 and 1.2, minor perturbations in the crystal structure have major effects on a material's global energy landscape.

1.3: Exciton Transport in Organic Materials

When considering the use of an organic semiconductor in a functional optoelectronic material such as in photovoltaics, photodetectors, or photocatalysts, it is essential to understand the fundamental principles of energy transport.[36] In organic materials, the primary mechanism of energy transport is excitonic, resulting in slow transport and very limited diffusion lengths around 5-10 nm.[2, 37] Generally, the ground state consists of an electronically neutral state; in the excited state, the excited molecule imposes reorganization and partial polarization of the electronic configuration(s). This response is an exciton (or polaron if the polarization is strong).[38, 39] An exciton is a quasi-particle of a coulombically bound negatively charged excited electron and the positive hole it leaves behind. The electron-hole pair is often localized to a single molecule because the energy to separate the two charges (the binding energy) is often too high to perform charge transfer; around 0.3-0.5 eV.[40-42] As a result of the high binding energy, transport is excitonic and can be described by either Förster resonance energy transfer (FRET) or Dexter energy transfer. Dexter energy transfer requires significant wavefunction overlap between donor and acceptor molecules and the rate of transfer falls off exponentially. This process usually happens on length scales <1nm.[43, 44] FRET on the other hand can be understood as a long-range interaction coupling of the dipoles,[44] and because the rate of transfer decays as r^{-6}, the interaction distances are on the order of 1-10 nm.[45-47]

1.3.1 Dexter Energy Transfer

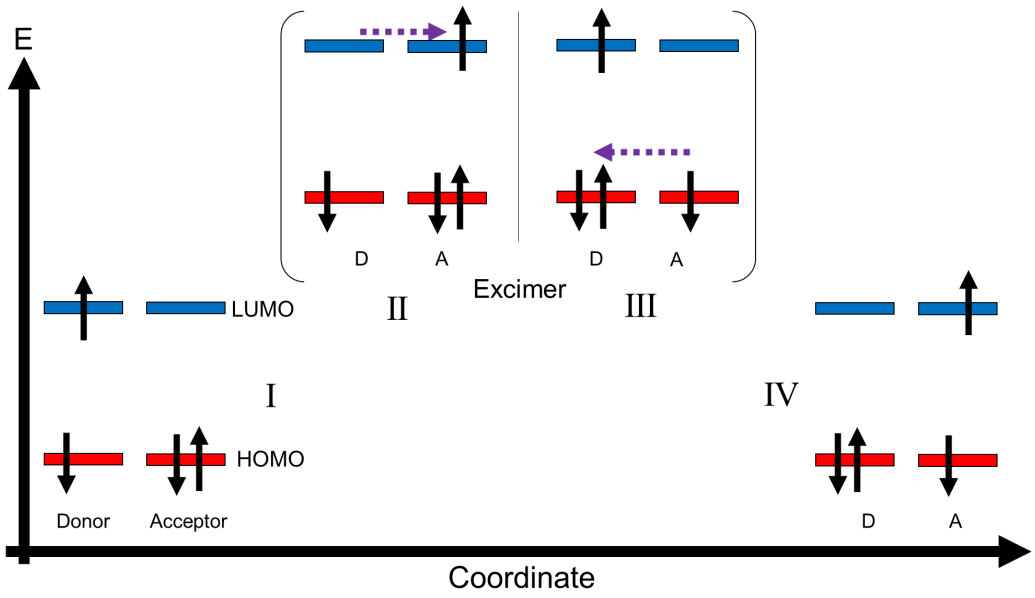

Figure 1.3.1: Simple model for Dexter energy transfer for singlet excitons, the different states of this process are represented by Roman numerals I-IV.

Dexter energy transfer is a method in which excitons move from monomer to monomer in an organic material. After excitation, the exciton is localized to a single molecule and can make an occasional "hop" to neighboring sites.[48] The mechanism of hopping can be understood as arising from two single electron transfer events (Fig. 1.3.1) in a single-step or two-step process.[49] The first scenario considers multiple single-particle interactions. State I is generated by one electron on the donor molecule being promoted to the Lowest Unoccupied Molecular Orbital (LUMO) from the Highest Occupied Molecular Orbital (HOMO). An electron (or hole) then "hops" to the neighboring acceptor molecule state II (III), generating a virtual charge transfer state, that is higher in energy. State II/III is then stabilized via another electron (or hole) transfer resulting in state IV

and the energy transfer is complete.[33] Scenario two arises from a two-particle interaction where the transfer occurs directly from state I to IV.

The rate of Dexter hopping is often empirically modeled using the temperature-dependent Miller-Abrahams hopping rate (k_{Hop}):[50]

$$k_{ij} = \nu \, Exp\left[-2\alpha r_{ij}\right] \begin{cases} Exp\left[\frac{-\Delta E_{ij}}{kT}\right] & \Delta E_{ij} > 0 \\ 1 & \Delta E_{ij} \leq 0 \end{cases}, \qquad \textit{eq 1.3}$$

where ν is the attempt to hop frequency, α is the inverse delocalization length exciton, r_{ij} is the distance of the hop, and E_{ij} is the energy difference between the initial and final state of the hop (further described in Chapter 5/appendix C). If we consider that the energy from monomer to monomer is dependent on the coupling described with equations 1.1 and 1.2, the hopping rate from the monomer significantly decreases with large variations in the energy landscape. If the exciton is moving from a low energy state to a higher state, the probability that the transfer occurs decreases exponentially as a function of the hop distance. If the energy landscape is homogeneous (i.e., the change in energy from site-to-site is 0) then the temperature-dependent exponential vanishes from the rate equation. Thus, it is evident that ordered systems can exhibit significantly faster transport than that of disordered systems.

1.3.2 Exciton Diffusion

On the molecular scale, it is clear how excitons transport from molecule to molecule. However, when considering a material, nearest neighbor hopping events that occur from single Dexter hopping events tend to lead to highly complex models because the interaction and its effects (e.g., polarons, charge transfers, etc..) must be considered for every molecule. To translate from the nanoscopic to the observable mesoscopic level, heavy computational resources and theory

parameterizations are required.[37] Instead, diffusion is often used as a measure of the random motion of excitons as they transfer from molecule to molecule. Diffusion is often defined as an area of high concentration of particles that disperse over time to become less concentrated (Fick's second law of diffusion). Fick's second law can be rewritten such that it accounts for exciton motion:

$$\frac{dn}{dt} = D\nabla^2 n - \frac{n}{\tau} + k_{ex,} \qquad Eq.1.4$$

where n is the exciton density, τ is the exciton lifetime, ∇ is the Laplace operator, k_{ex} is the rate of generated excitons, and D is the diffusion coefficient that determines how fast excitons can diffuse throughout a material.[38] The first term in eq. 1.4 represents exciton motion by diffusion, the second is the rate of recombination, and the third is the rate of excitation. Generally, the third term is often left out of the expression as most experiments are designed such that there is not a continuous rate of excitation, but rather that the excitation is instantaneous. From the diffusion coefficient and the exciton lifetime, the diffusion length can be calculated as:

$$L_D = \sqrt{2XD\tau}, \qquad Eq.1.5$$

where X is the spatial dimensions of diffusion (i.e., 1-, 2-, or 3-dimensional).

Diffusion itself is a random walk similar to the Miller-Abrams model for energy transfer. When measuring diffusion, we can detect the ensemble of single exciton hopping events and quantify their motion without the complexities of particle-particle interactions that Dexter energy transfer attempts to describe. As a final note on this section, the diffusion definitions above are relevant and sufficient for our work to quantify heterogeneity in organic films, but they are a simplified viewpoint. There are higher levels of theory that account for highly complex interactions

such as triplet formation, Frenkel delocalization, and charge transfer states which describe the diffusive motion of excited states in more detail.[41, 51-53]

1.3.3: Excited State Relaxation

Considerable progress has been made in understanding the electronic structure and energy transport mechanisms in aggregated dyes. However, the excited state lifetime, which is an essential parameter to many applications, has not been explored in the same detail.[54] There have been several studies showing the importance of the radiative and nonradiative decay processes in organic aggregates and these studies show that the non-radiative component ultimately dictates the lifetime of the excited state.[54-56] Determining the impact that the nonradiative decay has in excited state decay is often hard to explore because organic aggregates result in very fast relaxation lifetimes (<250 ps)[54] and need ultrafast instrumentation to disentangle these fast lifetimes from the instrument response function. A systematic study of the nonradiative lifetime was performed on monomers, dimers, trimers, and tetramer aggregates by Huff et. al.[54] This study shows that the excited state lifetime is reduced from 1300 ps down to 30 ps as aggregation increases from the monomer to the tetramer. Their overall conclusion was that the strength of coupling energy (J_{coul} as discussed in section 1.2.1) and distance between the monomers are the major contributors to the lifetime time decreasing by two orders of magnitude. Although this study shows a correlation, the lifetime of the excited state is often challenging to disentangle as it is a complex interplay of many processes including exciton delocalization, exciton transport, charge transfer, and electron-phonon coupling.[57,58]

1.4: Family of Molecules

To determine the effects of aggregation and the overall structural heterogeneity of solid-state organic materials we turned to three families of molecules: BODIPYs, porphyrins, and PBIs. In this section, a brief description of the molecules used in the following chapters will be provided. The reader can briefly familiarize themselves with these molecules that will be discussed throughout this document.

1.4.1: BODIPY:

The family of 4-bora-3a,4a-diaza-s-indacene (boron dipyrromethene, BODIPY) is a class of highly fluorescent chromophores that first appeared in the literature in 1968.[59, 60] BODIPYs have found their way into many applications such as biological imaging[61] and light harvesting materials.[62] What makes this class of molecules appealing for these applications is their high photo-stability, robust fluorescence intensity, narrow emission bands, large extinction coefficients, and fluorescence quantum yields.[60, 63] Additionally, the photophysical and physical properties (e.g. solvent solubility) of BODIPY are highly tunable, thus making it suitable for very specific applications.[36] The tunability of BODIPY comes from the ease of functionalization of the core. When substituting the BODIPY core, it is common to use the naming convention based on either the numbering scheme or by the alpha, beta, and/or meso position as depicted in Fig 1.4.1.1. Functionalization often occurs as a one-pot synthesis with pre-substituted precursors. General methods for chemical synthesis include the acid-catalyzed condensation of an aldehyde with two pyrroles.[64] This condensation reaction is typically carried out in dichloromethane (DMC) or tetrahydrofuran (THF) with trifluoroacetic acid (TFA) and is then oxidized using DDQ. This reaction is then treated with BF_3Et_2/Et_3N to yield the BODIPY molecule.

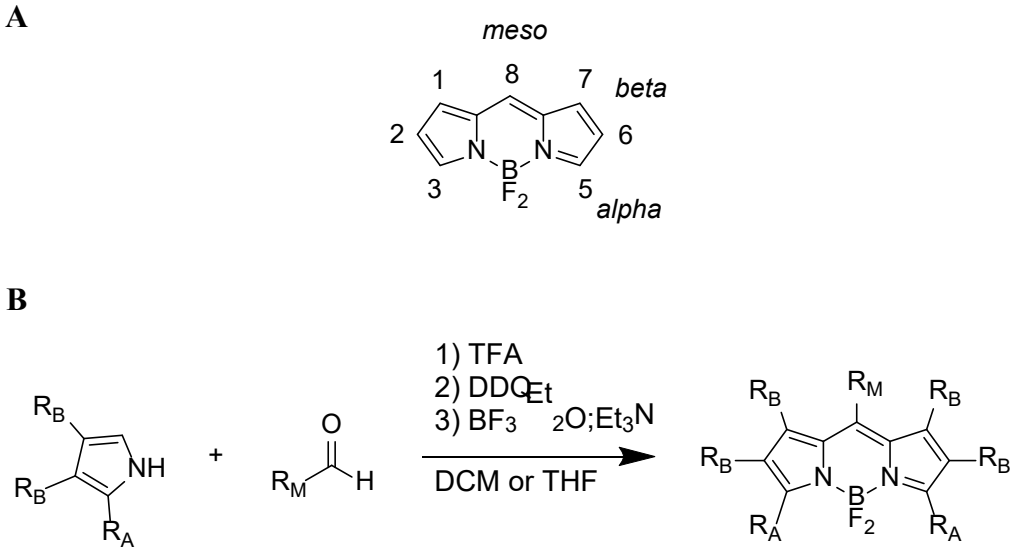

Figure 1.4.1.1: A) The BODIPY core with a numbering scheme shown. 3,5 positions are commonly referred to as the *alpha* position, 2,6 and 1,7 are the *beta* positions and 8 is the *meso* position. B) General reaction scheme for BODIPYs.

BODIPYs and their analogs have been well characterized throughout the years. Typical photophysical properties involve high extinction coefficients around 70,000-80,000 $M^{-1}cm^{-1}$ at the maximum absorption wavelength,[65] narrow absorption bands with a full width half max around 30-50 nm,[65] and high fluorescence quantum yields around 0.50-0.70.[65] The electronic structure of BODIPYs can be generalized as having a main narrow absorption band consisting of a S_0-S_1 π-π* transition around 480 nm with a shoulder (the 1-0 vibronic transition) and a broad/low-intensity band consisting of a S_0-S_2 π-π* transition at ~350 nm.[66] Since the BODIPY platform can be heavily modified, these are general characteristics for simple BODIPY molecules. When considering changing the electronic structure to achieve broader and/or redder absorption, three simple rules can be applied to reduce the HOMO-LUMO gap:[67] i) introducing electron-withdrawing groups at the meso-position,[68] ii) introducing electron-donating groups at the alpha-positions,[69] iii) and extension of the core's π-system.[70]

Recently, there has been interest in the solid-state properties of BODIPY molecules. To date, solid-state BODIPY-based materials have found their way into BODIPY-based metal-organic frameworks (BMOF),[71, 72] BODIPY aggregates,[73] fibers,[74] disks,[75] nanorods,[75] and solid powders.[76] Solid-state BODIPYs have been characterized, but in-depth literature on the photophysical properties remains sparse. This is in part due to the negative consequences of solid-state deposition such as aggregation in the solution-phase not always translating to solid-state long-range order,[77-79] the difficulty of characterizing the materials with photostability,[80] and/or heavy substitution compromising the indacene backbone.[79] Although a challenging molecule to study in the solid-state, there is still interest in studying solid-state BODIPYs because of their facile tunability and potential application in light-harvesting materials.

1.4.2: Porphyrins:

Porphyrins are macrocycle molecules that consist of four pyrrole rings linked through methene bridges. Due to their presence in nature as heme [81] or chlorophyl[82] like molecules, porphyrins have been used in a variety of applications including sensors,[83] photocatalysts in organic synthesis,[84] and energy harvesting as a "green" resource.[85] Figure 1.4.2.1. A showcases the core and the respective naming scheme. The *meso* position occurs at 5,10,15, and 20 positions, while the *beta* position occurs on the terminal pyrrole rings. Since the alpha position occurs in the inner core, it is not often referred to in substitutional naming conventions. Similar to the BODIPY platform, this macrocycle is highly tunable through chemical synthesis. The core can be modified via two methods: i) post-core synthesis, in which functional groups are added after the core is made, and ii) pre-core synthesis, where the pyrrole and/or aldehyde is modified with functional groups to produce the final modified porphyrin. Figure 1.4.2.1.B is a general scheme that depicts

the ease of synthesis, recreated from Hiroto et al.[86] Additionally, porphyrins can be synthesized as either freebase (metal free) or with a metal center. When novel porphyrin molecules (metalated and freebase) are characterized, tetraphenyl porphyrin (TPP) is used as a comparison benchmark due to the simplicity and symmetry of the molecule; Zinc TPP (ZnTPP)[87] is used for metalated compounds, and the free base TPP (H_2TPP).[88]

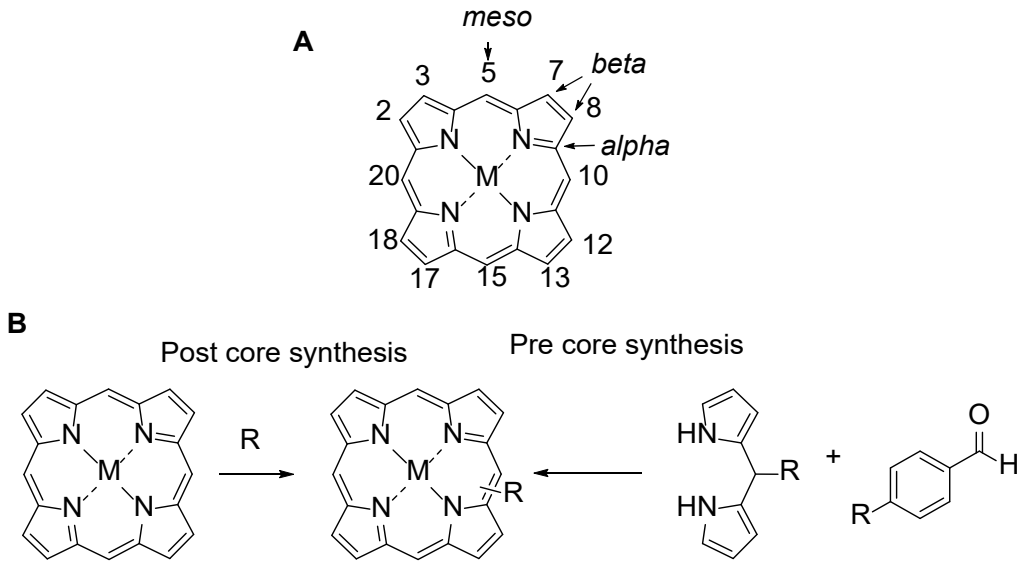

Figure 1.4.2.1: A) The numbering convention for the porphyrin core with positions 3,10,15,20 referred to as the *meso* position, *beta* positions on the outer pyrrole ring, and *alpha* positions on the inner pyrrole ring. B) Example of post-core synthesis, where functional groups "R" are added after the porphyrin core is synthesized, and "pre-core synthesis" where the functional groups are introduced into the precursors.

The electronic absorption spectra of both the metal and metal-free porphyrins can be highly complex based on the derivative. However, most porphyrins will have an absorption spectrum that has a high-intensity Soret (or B) band at ~420 nm that consists of a S_0-S_2 π-π* transition. At lower energies of 500-700 nm, there are 2-4 weaker intensity bands called the Q bands, which consist of a S_0-S_1 π-π*transition. The observation of 2 or 4 Q bands can be attributed to the symmetry of the

molecule. The metal-free di-protonated porphyrin has C_{2v} symmetry. When a metal center is added, the symmetry is increased and there is a 4-fold rotational axis and a mirror plane, thus making the overall symmetry D_{4h}. The increase in symmetry results in the LUMO and LUMO+1 becoming degenerate in energy. [89, 90] Additionally, when a metal center is added, the vibronic coupling modes become more pronounced.[91-94] This phenomenon is well documented and typically explained using Kohn-Sham MO energy diagrams[95] or Gouterman orbitals.[96] Although the molecular orbitals and energetic states are complex and vary based on the porphyrin derivative, for this document, the Q band consists of the $S_1 \leftarrow S_0$ transition with $Q_x(0\text{-}1)$, $Q_y(0\text{-}1)$, $Q_x(0\text{-}0)$, and $Q_y(0\text{-}0)$ sub-band transitions.

1.4.3: PBIs:

Amongst the organic semiconductor community, the family of perylene bisimide, PBI, (or diimide, PDI) molecules are considered one of the best n-type semiconductors.[97] These red color pigments have very good chemical, thermal, and light stability.[98] Because of these desirable properties, PBIs have been utilized in coatings (automotive paint),[99] fluorescent switches,[100] solar cells,[101] light absorption sensors,[102] organic field effect transistors,[103] and organic light-emitting diodes.[104] In addition to their stability, their high extinction coefficients (>50,000 $M^{-1}cm^{-1}$) and fluorescence quantum yields (~1) make them suitable for the aforementioned applications.[105-107]

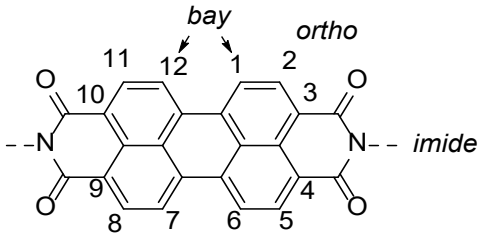

Figure 1.4.3.1: Naming scheme for perylene bisimide.

The PBI core consists of a central conjugated five-membered ring core with two terminal imide groups and can be named based on substitutions at the *bay*, *ortho,* and/or *imide* positions or by the numbering scheme as seen in Figure 1.4.3.1.[108] Although there are many synthetic routes to synthesize this class of molecule, it is easily synthesized from the condensation between 3,4,9,10-perylene tetracarboxylic dianhydride (PTCDA) and an amine precursor. However, due to the high yields of the PBI core, the core is often purchased rather than synthesized.[109]

PBI molecules can form supramolecular assemblies through the π-π interaction through the cores. Often, the π-π interaction of the cores has an interlayer spacing of 3.4–3.5 Å.[110] The interaction between the cores causes H-type coupling that leads to a blue shift in the absorption and emission spectra, as described previously in section 1.1.1.[27] Although there are cases of J-type coupling,[27, 111, 112] coupling does not involve the self-assembly of the cores, but rather polymerization using functionalized cores.

CHAPTER TWO

METHODS AND METHODOLOGY ON PUMP PROBE MICROSCOPY

Bulk measurements fail to result in microstructure characterization and evaluation of structural heterogeneity. Ultrafast microscopies can be used to measure the excited state dynamics and optical properties of organic-based semiconducting materials with submicron spatial resolution and evaluate structural heterogeneity. For the experiments in this work, a majority of the instrumentation relies on a homebuilt two color pump probe microscope (unless otherwise stated in the chapters and appendices). The purpose of this chapter is to give a detailed description of the main instrumentation technique and the types of measurements the pump probe microscope is capable of.

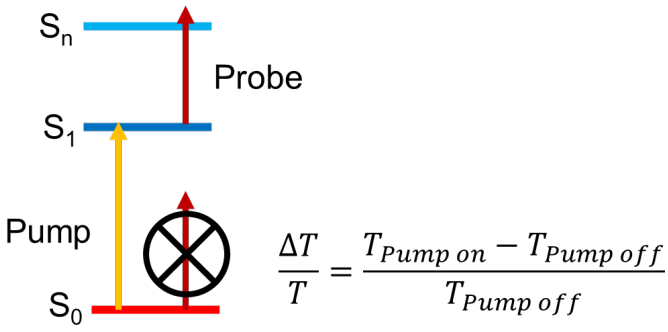

Figure 2.1: Simplified energy level diagram for excited state absorption and the calculation of observable signal.

The underlying physical process for two color pump probe microscopy relies on ultrafast transient absorption (TA), which generally produces a signal comprised of three main processes: ground state bleach/GSB, stimulated emission/SE, and excited state absorption/ESA. However,

the organic materials studied in this dissertation are non-absorptive in the ground state in the near-infrared, and the probe wavelengths are chosen only to monitor the excited state absorption band. For ESA, when the probe reaches the material, the energy gap is too large for the absorption of the photon (the probe is nonresonant with the material). The pump conversely is resonant and has the energy to promote the material into the excited state. When the material is in an excited state, new energic pathways open up such that the probe can be resonant with the material and further excite the material higher in energy, resulting in a loss of probe photons. To quantitatively measure this process, probe photons are measured when the pump is and is not present. This results in a change in transmission (T) calculated by $\Delta T = T_{\text{pump on}} - T_{\text{pump off}}$. For excited state absorption, ΔT is always negative.[113] Although this document covers pump probe microscopy at a level necessary for this work, the following citations are an excellent resource for understanding the advanced theoretical details and physics behind the instrumentation.[114-116]

2.1 Pump Probe Microscope

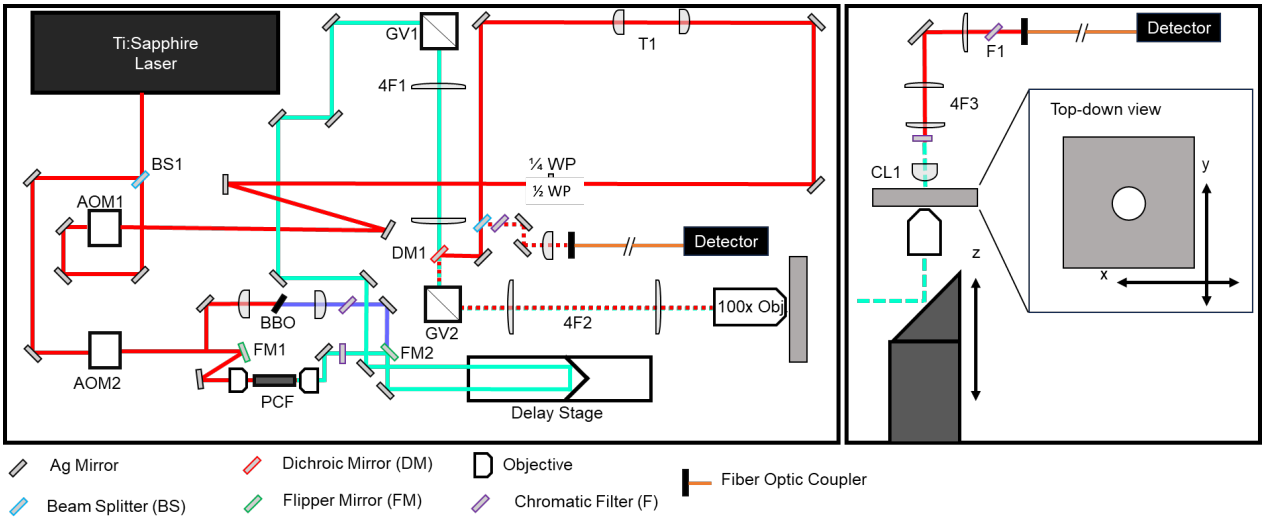

Figure 2.1.1: Schematic of a pump probe microscope. The left panel corresponds to a top-down view of the entire table. The right panel corresponds to a side view of the vertical stage. Abbreviations in the Figure that are not listed in the legend include waveplate (WP), galvanometer mirror (GV), four focal length system (4F), telescope (T), photonic crystal fiber (PCF), beta barium borate (BBO), and condenser lens (CL).

2.1.1: Instrumental Overview

Pump probe microscopy (PPM) experiments were performed on a home-built system depicted in Figure 2.1.1. The fundamental beam originates from a Spectra Physics MaiTai laser (~80 fs pulse width, 80 MHz repetition rate, 800 nm fundamental) and is split into the pump and probe lines using a plate beam splitter. The pump line is passed through an acoustic optic modulator (AOM) to reduce the repetition rate of the pulse train from 80 MHz and modulate with a 50% duty cycle. The modulated pump is focused through a photonic crystal fiber (PCF) to generate a white light supercontinuum which is passed through a bandpass filter to select the pump wavelength (+/- 5 nm). The spectrally filtered pump is coupled to an optical delay stage to achieve a temporal delay from that of the probe line. The pump line is coupled, via a pair of galvanometer (GV) mirrors,

through a 4-f telescope and combined with the probe with a dichroic beamsplitter. The probe line is first modulated from 80 MHz via an AOM to match the repetition rate of the pump. The combined beams are sent onto a set of GV mirrors, through a 4-f telescope, and coupled into the back aperture of a 100x plan apo objective to focus onto the sample. The two beams are collected with a condenser and the pump beam is filtered out using a long-pass filter. The probe is focused on an amplified silicon photodiode. The amplified photodiode (APD) signal is split (Mini Circuits ZFRSC-2050+). One output is sent to a Stanford Research lock-in amplifier to demodulate the signal (ΔT). The other is coupled to a National Instruments (data acquisition) DAQ card for the reference (T). The resulting measured signal is tabulated as $\Delta T/T$.

2.1.2: Pump Path

The pump beam starts at BS1 where the fundamental beam is split into two lines. The beam from BS1 is reflected and directed to the acousto-optic modulator at AOM2 (description of the AOMs is in section 2.1.5), allowing for the modulation and control of the pulse repetition rate. When the flipper mirror (FM1) is faced down, the beam is redirected on an alternative path toward a photonic crystal fiber (PCF) to generate a broadband continuum for variable excitation. The excitation wavelength can be selected using a bandpass filter (F1). Since the polarization of the beam is not well retained after continuum generation, a polarizing cube is placed in the line to filter out unwanted polarizations. If FM1 is faced up, then the beam is directed into a Beta Barium Borate (BBO) crystal that frequency doubles the fundamental beam (e.g., 800 to 400 nm). The remaining fundamental beam is filtered out using a bandpass filter at F2. Flipper mirror 2 (FM2) is left up when the PCF is in use and put down when the BBO is in use. The use of a BBO crystal often is beneficial because of the narrow pulse duration and the loss of pump intensity is much less

than that of a continuum generation. However, organic materials often have complex absorption spectra, and variable excitation via the PCF is ideal. Regardless of which beam path is in use, both beams are configured such that the pump line is sent on to the delay stage to achieve controllable pump probe delay. This delay stage moves forward to achieve a time delay between the pump and probe pulses with ~4 micrometer precision which results in a minimum temporal step size of 13 fs. The beam is then sent onto a set of galvanometer mirrors (GV1) and through a four-focal length system (4F1) before being spatially recombined with the probe beam at DM1. Since only the pump is on GV1, the acquisition of spatially offset scans is possible. After DM1 the pump is set onto GV2. Since this set of galvanometer mirrors contains the pump and probe beams, GV2 allows for the acquisition of spatially overlapped scans for excited state imaging. The beams are then sent through the 4-F2 system before being coupled on the back aperture of the objective and focused on the sample.

2.1.3: Probe Path

The probe beam originates where the pump beam is reflected at BS1 except this portion of the beam is transmitted through the optical element. To control the repetition rate of the probe, the beam is focused into the AOM1 system. The beam is sent on a long path to match that of the probe, such that temporal pulse overlap is achieved at the sample. If the PCF is used to generate the excitation wavelength, there is a ¼ waveplate (WP) to rotate the polarization of the beam and a telescope (T1) to match the focus of the pump beam. The probe beam is then coupled with the pump beam at DM1. The remainder of the probe path is the same as described above (2.1.2).

2.1.4: Post Sample Beam Path

After the beam interacts with the sample, the beam is simultaneously transmitted through the sample and reflected along the incident path. The sections below describe the respective pathways to the detector.

2.1.4.1 Transmissive Detection

The right panel in Figure 2.1.1 depicts the detection line after interacting with the sample. After the sample, the beam rapidly starts to expand due to the tight focus of the objective. This light is captured using an achromatic condensing lens (CL1) and collimated thereafter. After this lens, the pump beam is filtered out using either an edge pass, band pass, or dichroic mirror; the beam then passes through the final 4F system (4F3) before being focused on a fiber optic coupler or directly onto a silicon photodiode.

2.1.4.2 Reflective Detection

The sample and substrate of the sample reflect the beam along the incoming beam path until the beam hits a 30:70 BS. The reflected beam is picked off with this beam splitter, spectrally filtered, and focused on the fiber optic coupler or silicon photodiode. This line is useful when measuring diffusion on purely inorganic samples, like silicon, with high extinction coefficients at the probe wavelength.

2.1.5: Acousto-Optic Modulator

The AOMs used in this PPM instrument serve two purposes: i) reduce the repetition rate of the fundamental beam in the event there are lingering thermal effects, or the excited state lifetime is longer than the fundamental time delay between pulses, 12.5 ns. ii) Modulate the pump

such that we can measure $\Delta T = T_{pump\ on} - T_{pump\ off}$. The Ti:Sapphire laser has an electronic output reference signal at 40 MHz; this electronic signal can be divided by a delay generator to reduce the repetition rate. In the example in Figure 2.1.5.1.B2, the signal is divided by 5 to produce an 8 MHz electronic signal, this electronic signal is then sent to the AOM to reduce the laser pulse repıation rate to 8 MHz. To modulate the pump for the measured $\Delta T/T$ signal, a function generator is used to generate a 120 kHz square wave. The square wave signal is then multiplied with the 8 MHz reference signal to produce the 8 MHz on 120 kHz electronic signal, and this is then sent to AOM2 on the pump line. Figure 2.1.5.1 depicts the laser diagram and pulse picking.

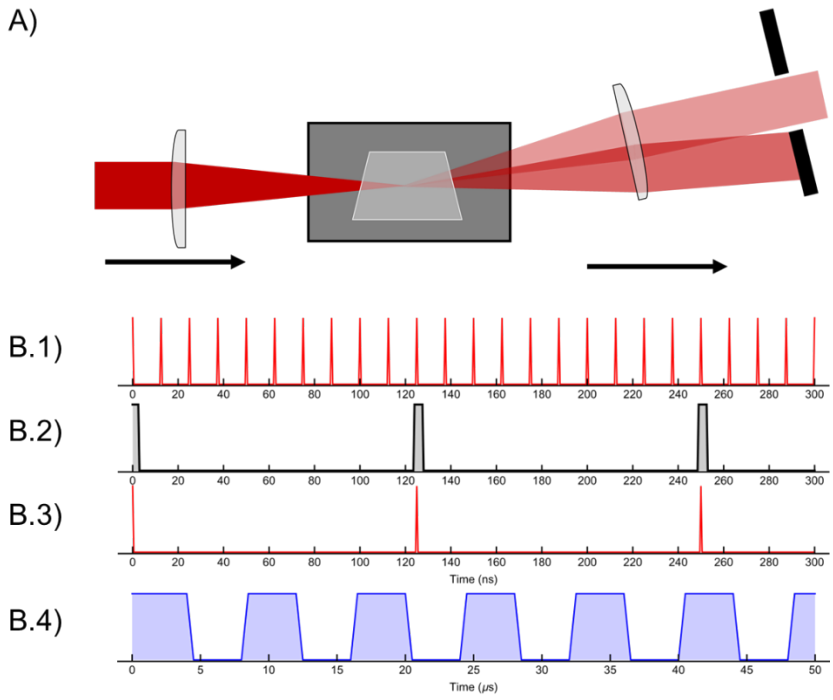

Figure 2.1.5.1: A) Diagram of the left fundamental being modulated by the acoustic crystal and the modulated beam is spatially filtered using a beam block. B.1) The 80 MHz fundamental pulse train. B.2) The electronic pulse generated from the delay generator is sent to the AOM receiver. B.3) The 8 MHz pulse train after the AOM has pulse picked. B.4) The 120 kHz square wave function is used to modulate the pump for pump on and pump off duty cycles.

2.2: Classification of Measurements

The pump probe microscope allows for three classes of measurements that permit the spatiotemporal evaluation of the excited state of a material. These measurements are: i) excited state kinetics, ii) spatially overlapped imaging, and iii) spatially separated imaging. This section will cover how these measures are taken and their importance.

2.2.1 Kinetic Lifetime Measurements

Kinetic lifetime measurements allow for the temporal evaluation of the excited state decay in a material. This process starts by promoting the material into the excited state at a specified location. The probe interacts with the excited material and can be absorbed since new excitation pathways become accessible in the presence of the pump. The signal intensity is proportional to the number of excited states generated from the pump (e.g., the excited state population). The probe can be delayed from the pump arrival time such that the material is sampled sometime after photoexcitation. By measuring the signal intensity as a function of pump probe delays (Δt), the material's excited state decay can be measured. One advantage to using a microscope objective is that beams can be tightly focused on the sample, allowing kinetic information to be extracted from various locations of a material with diffraction-limited spatial resolution.[116]

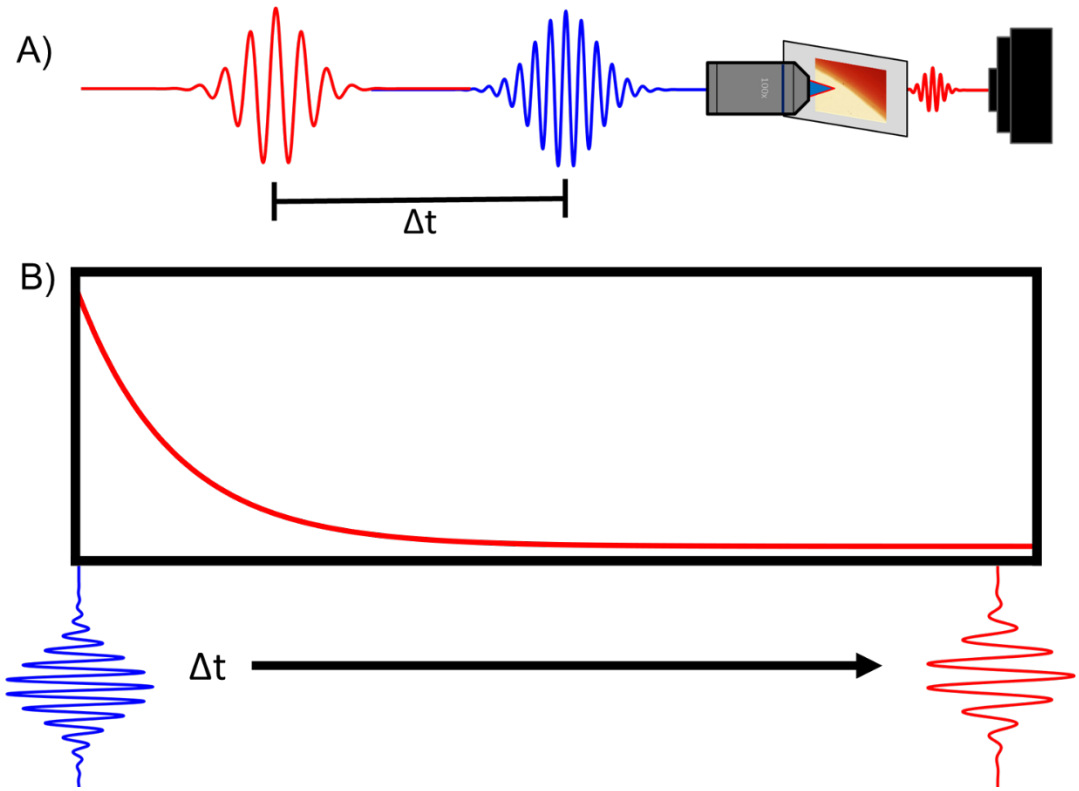

Figure 2.2.1.1: Panel A is a cartoon representation of a pump probe microscope. The pump probe delay, Δt, is depicted by the time separation of the two pulses (red and blue). Panel B corresponds to an example of typical kinetic data. Kinetic data is achieved by temporarily controlling the delay between the pump and probe pulses.

The excited state population relaxes to the ground state over time and can be described mathematically by a differential equation:

$$\frac{\partial N(t)}{\partial t} = -kN(t), \qquad \textit{eq 2.1}$$

where the change in the number of excited states (N) per change in time is equal to the rate of decay (k) multiplied by the number of excited states at a given time. In the simplest cases, the solution to eq 2.1 becomes an exponential decay by the following:

$$\int_{N_0}^{N(t)} \frac{1}{N(t)}\,\partial N = \int_{t=0}^{t} -k\,\partial t$$

$$\ln\big(N(t)\big)\Big|_{N_0}^{N(t)} = -kt$$

$$N(t) = N_0 Exp[-kt]. \qquad \textit{eq 2.2}$$

In multilevel decay systems that often are present in most materials, the population decays as a function of multiple relaxation rates, and eq 2.1 becomes: $\frac{\partial N(t)}{\partial t} = -k_1 N(t) - k_2 N(t) - \cdots$. Thus, it becomes relevant to describe the total excited state population as the summation of exponential decays from given states (N_i):

$$N(t) = N_1 Exp[-k_1 t] + N_2 Exp[-k_2 t] + \cdots. \qquad \textit{eq 2.2}$$

Equation 2.2 expresses the excited state population that is determined by the rate of relaxation from a given state. However, it is more common to express the excited state relaxation in terms of the lifetime of the excited state (τ) rather than the rate:

$$\tau_i = \frac{1}{k_i}$$

$$N(t) = N_1 Exp\left[\frac{-\tau_1}{t}\right] + N_2 Exp\left[\frac{-\tau_2}{t}\right] + \cdots. \qquad \textit{eq 2.3}$$

Without spectroscopic techniques to determine which of the excited states the population decays from, as a consequence, the observed lifetime is often reported as the average lifetime,[117] $\langle\tau\rangle$, that accounts for the contributions (N_i, the exponential prefactor) of each of the decay processes:

$$\langle\tau\rangle = \frac{N_1\tau_1 + N_2\tau_2 + \cdots}{N_1 + N_2 \ldots}. \qquad \textit{eq 2.4}$$

2.2.2 Spatially Overlapped Imaging

The second class of measurement is spatially overlapped imaging. In this measurement, the pump and probe beams are spatially overlapped on the sample at a set delay time, and raster scanned over the sample. By measuring the $\Delta T/T$ as a function of beam location, a spatial map of

the excited state can be generated with a resolution that is only limited to the convolution of pump and probe ($\sqrt{\frac{\lambda_{Pump}^2+\lambda_{Probe}^2}{2NA}}$). The diffraction-limited spatial resolution allows for the ability to probe structure-function relationships in materials with microscale spatial resolution, such as the excited state properties at heterojunctions and crystal deformations that are unresolvable by bulk measurements.[116]

2.2.2.1 Excited State Lifetime Imaging

Excited state lifetime imaging is similar to the well-developed technique of fluorescence lifetime imaging microscopy (FLIM), with the advantage that measurements can be taken on non-emissive materials. FLIM typically uses time-correlated single photon counting (TCSPC) to measure kinetic decay with high spatial resolution.[118] The radiative lifetime is plotted as a function of location to generate a spatial map of lifetimes.

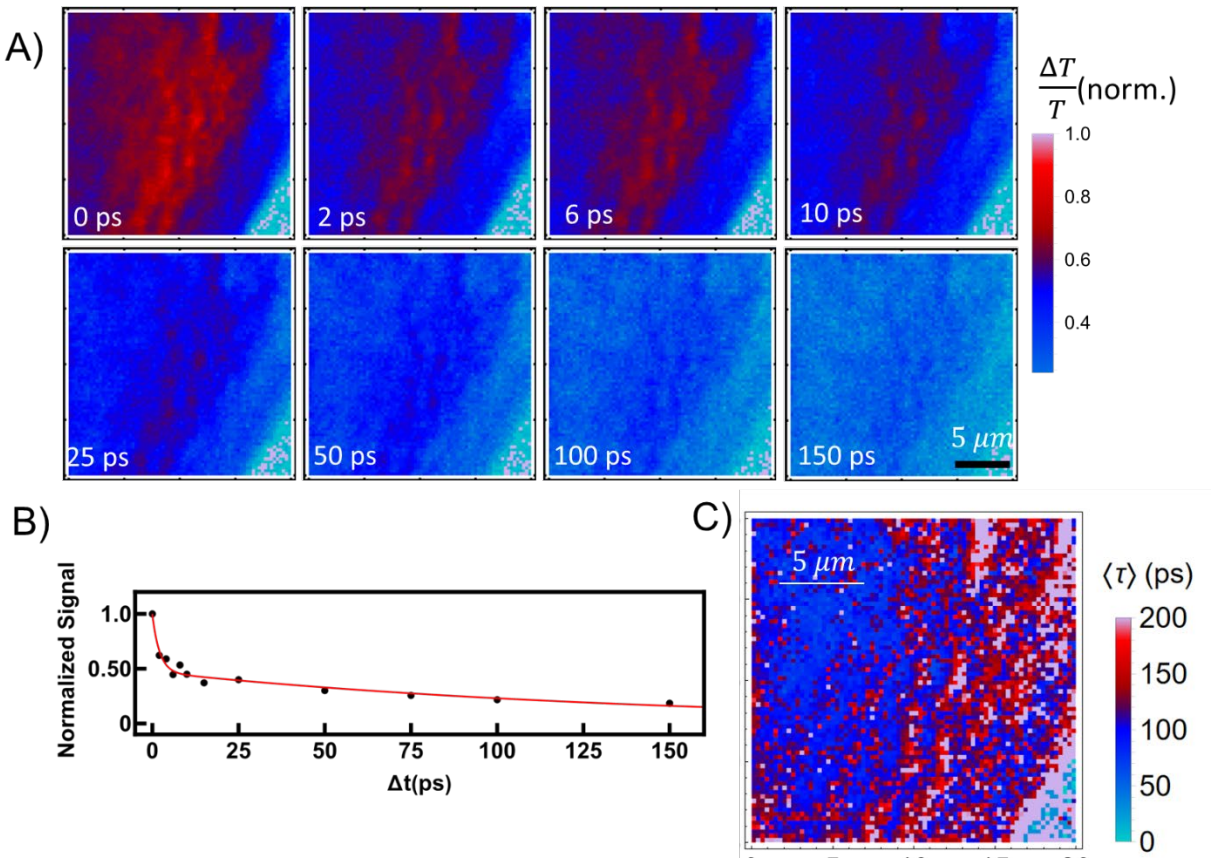

Figure 2.2.2.2: This figure is an example ESLIM data set. A corresponds to the ΔT/T signal at an ROI and a series of time delays. Panel B corresponds to a single pixel location's signal intensity at various pump probe time delays. Panel C corresponds to the average lifetime that was fit at the corresponding pixel.

Excited state lifetime imaging (ESLIM) can be used to map the lifetime across a domain or region of interest via a series of pump probe spatially overlapped images at increasing delay times (fig.2.2.2.2A). Each pixel in the image stack is extracted and tabulated with the corresponding time delay, and the extracted data set is then fit to an exponential decay function. The lifetime (or average lifetime for multiexponential fits, $\langle\tau\rangle$)[119] fit at each pixel can be spatially mapped to yield an excited state lifetime image. Although the advantage of this technique is the high spatial resolution, the main limitation is the temporal resolution. To generate enough time points to generate a sufficient fit, a considerable amount of lab time must be dedicated to

continuous data acquisition. Because ESLIM measurements can take upwards of 50 minutes, it is important to note that this timescale can introduce environmental perturbations such as sample or focus drift.

2.2.3 Spatially Separated Imaging

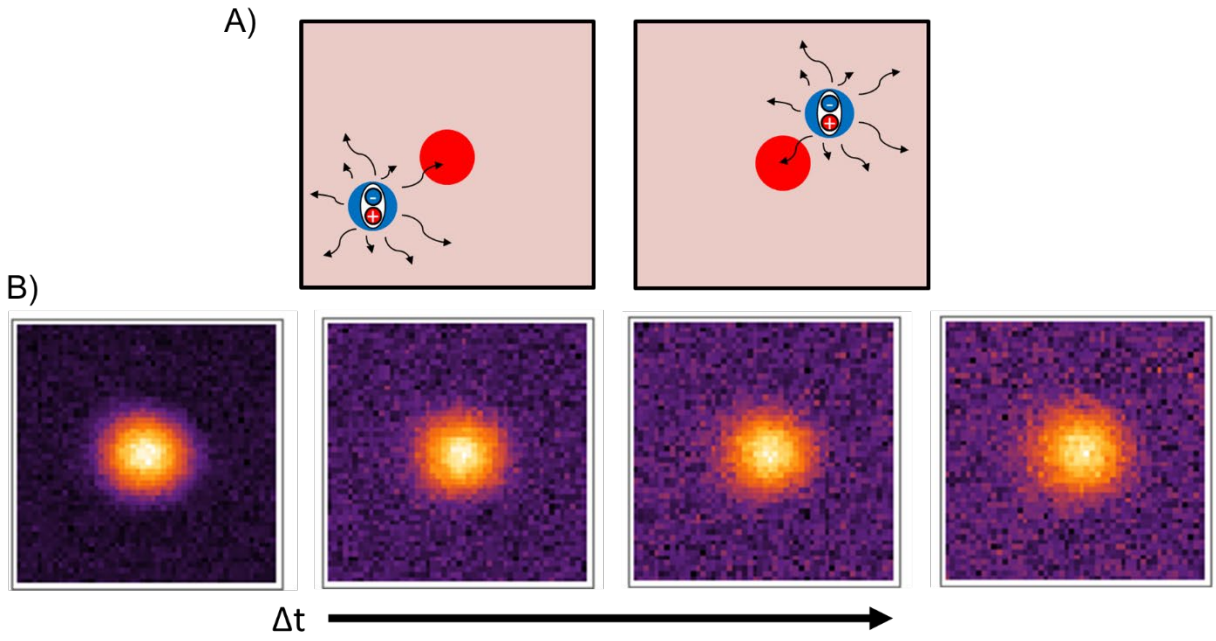

Figure 2.2.3.1: A) A cartoon representation that depicts a region of interest on a material where excitons are generated via the pump at various locations and diffuse into the probe. B) Example diffusion data set.

Spatially separated imaging provides a means to measure a material's transport properties and quantify the diffusion coefficient. To do this, the probe is held at a specified fixed location on the sample and the pump is raster scanned over the probe. The pump generates excitons in the material that diffuse in all directions, however, only the excitons that interact with the probe are detected (Figure 2.2.3.1A). Because the pump is raster scanned over the probe, a spatial map of the excitation can be obtained. If this measurement is done at increasing pump probe time delays,

the spatial evolution of sample excitation can be tabulated, and a diffusion coefficient can be calculated. (Fig. 2.2.3.1B).[116]

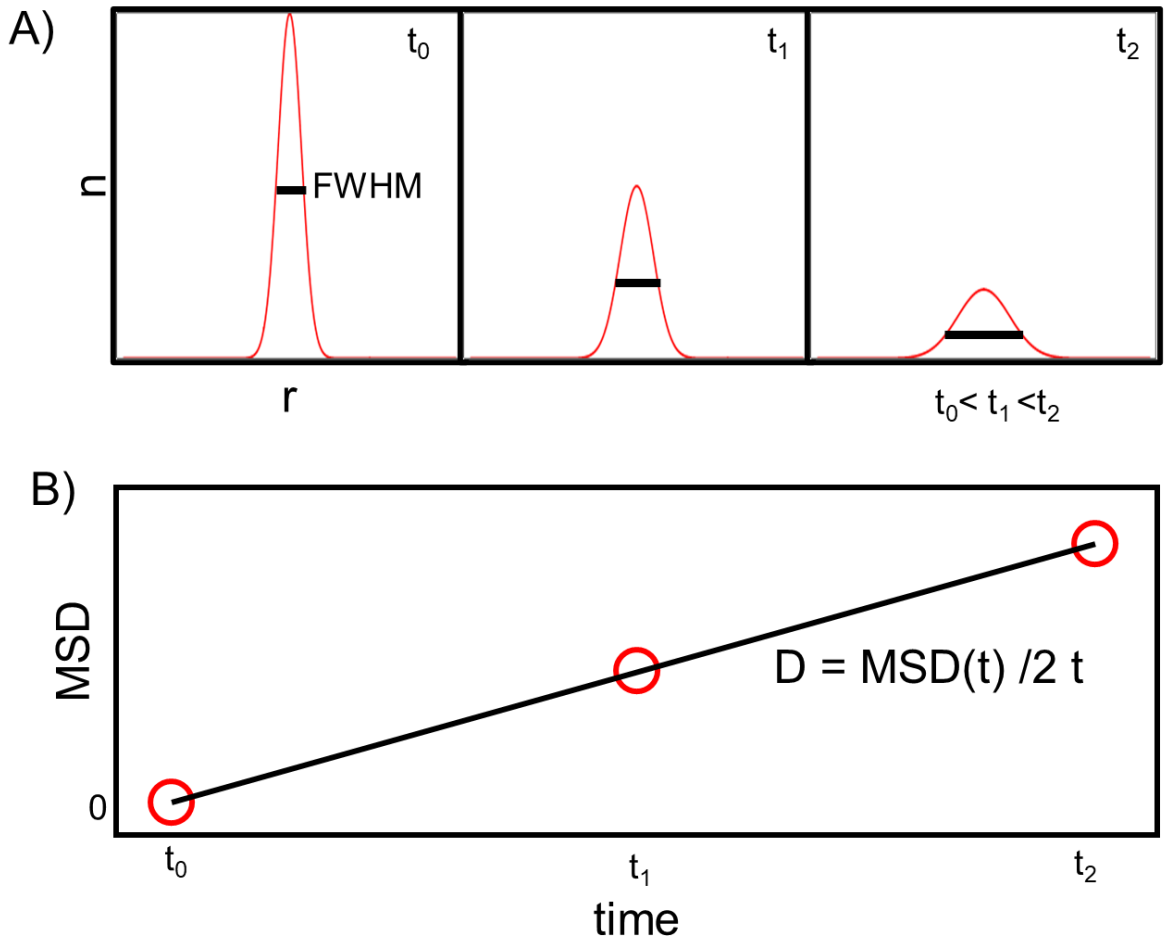

Figure 2.3.3.2: A) is a cartoon representation of the number of excitons, n, versus a distance, r. The three panels correspond to increasing time delays of that profile. B) is a cartoon representation of the mean squared displacement from the FWHM at t_0. The linear fit's slope is used to determine the diffusion coefficient.

To determine the diffusion coefficient,[120-122] the image stack of spatially separated spots is split into angular cross-sections, centered at the middle of the spot. At each time point, these are

extracted and normalized. Since the population of excitons generated from a typical laser pulse is Gaussian in shape, the pixel data can be fit to a Gaussian function:

$$\frac{\Delta T(x)}{T} = Exp[-\frac{x^2}{2b^2}] \qquad \textit{eq. 2.5}$$

Where x is the distance in the image stack and b is the fitting parameter. The FWHM of the Gaussian functions are determined by FWHM= $2\sqrt{2ln2}\,b$. Under a linear diffusion regime, the growth of the FWHM (following immediate excitation from the laser pulse) increases proportionally with time. The mean squared displacement (MSD) is a measure of Gaussian growth. The MSD is calculated by:

$$\mathrm{MSD(t)} = \big(\mathrm{FWHM(t)} - \mathrm{FWHM(t=0)}\big)^2 \qquad \textit{eq 2.6}$$

By correlating the mean squared displacement versus time, the rate of growth (the diffusion coefficient, D) is calculated using linear least squares fit:

$$D = MSD(t)/2t \qquad \textit{eq.2.7}$$

The fitting method described above is summarized in Figure 2.3.3.2.[123, 124]

CHAPTER THREE

ULTRAFAST EXCITONIC TRANSPORT AND STRONG ELECTRONIC COUPLING IN SELF-ASSEMBLED ALPHA-STYRYL-BODIPY NANORIBBONS

Contribution of Authors and Co-Authors

Manuscript in Chapter 3

Author: Alexander J. King
Contributions: Formal analysis, investigation, methodology, software, writing-original draft, writing-review & editing.

Co-Author: Austin A. Phillips
Contributions: Synthesis and purification of BODIPY monomers

Co-Author: Kathryn R. Zimlich
Contributions: Collected confocal emission images

Co-Author: Skyler R. Hollenbeck
Contributions: Built functional broadband pump probe instrument

Co-Author: Nicholas J. Borys
Contributions: Project administration on the time-resolved photoluminescence instrument.

Co-Author: Christopher M. Lemon
Contributions: Conceptualization, funding acquisition, writing-review & editing.

Co-Author: Erik M. Grumstrup
Contributions: Conceptualization, formal analysis, funding acquisition, methodology, project administration, software, supervision, writing-original draft, writing-review & editing.

Manuscript Information

Alexander J. King, Austin A. Phillips, Kathryn R. Zimlich, Skyler R. Hollenbeck, Nicholas J. Borys, Christopher M. Lemon*, Erik. M. Grumstrup*

ACS Nano Letters

Status of Manuscript:
☒ Prepared for submission to a peer-reviewed journal
☐ Officially submitted to a peer-reviewed journal
☐ Accepted by a peer-reviewed journal
☐ Published in a peer-reviewed journal

ACS Nano Letters

Abstract

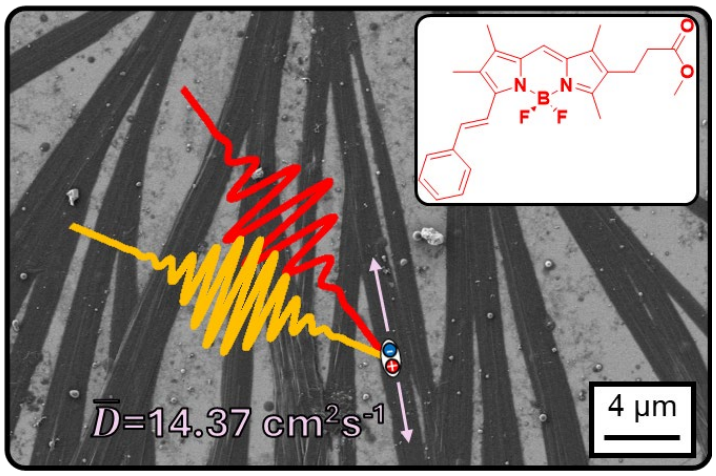

BODIPY based materials have found their way into many applications including photovoltaics, OLEDs, and thermochromic materials, however, the photophysical properties of condensed phase BODIPY systems are challenging to investigate. Exciton transport in aggregates composed purely of BODIPY remains elusive. We have synthesized self-assembled BODIPY nanoribbons and investigated their excited states and exciton transport properties at short time scales through ultrafast spectroscopies and microscopies. In this work, we show that: i) the electronic states are highly coupled with a major redshift from 583 nm in the solution to 614 nm on the ribbon. ii) through interpretation of the broadband transient absorption spectrum, the initial excited state is highly delocalized and localizes within the first ten femtoseconds. iii) Using two color pump probe, we measured ultrafast diffusion at 14.37 ± 2.79 cm^{2}s^{-1} that abruptly halts after 10 ps, which is consistent with the exciton trapping that was measured in broadband experiments.

Manuscript

Introduction

Over the past thirty years the family of molecules 4,4-difluoro-4-bora-3a, 4a-diaza-s-indacene (BODIPY) has been studied in great detail, not only to understand the family's fundamental photophysics, but also for its application in optoelectronics and biological systems.[125] In its solid-state, BODIPY-derived materials have been used as a hole transport layer in photovoltaics[126], organic light-emitting diodes (OLEDs)[127], and thermochromic materials[128]. As an organic semiconductor, pure BODIPY aggregates tend to have high electronic coupling in the solid-state that leads to new fast relaxation pathways.[129] Although significant attention in the literature is given to the synthetic approaches to reduce fast relaxation,[130] little is known about the photophysics of electronically coupled BODIPY materials.[129] In an attempt to understand the coupling effects, the photophysics of solution-phase J-coupled dimers, molecular J-aggregates, and excimers has been studied to some extent,[131-135] however, there is a major knowledge gap when it comes to solid-state exciton relaxation lifetimes, excited state relaxation pathways, and transport rates in these strongly coupled BODIPY materials.

In this work, recrystallization of the molecular BODIPY resulted in a serendipitous discovery of a gold fibrous material, indicating that the monomers self-orient themselves with long-range order. It was discovered that upon solid-state deposition via drop casting, the monomers crystallize into long and flat ribbon-like structures. We characterized these self-assembled ribbons via microscopic techniques including ultrafast microscopies to investigate excitonic transport in the ribbons, ultimately revealing their high structural and energetic order, electronic coupling, and fast diffusion rates.

Synthesis and Characterization

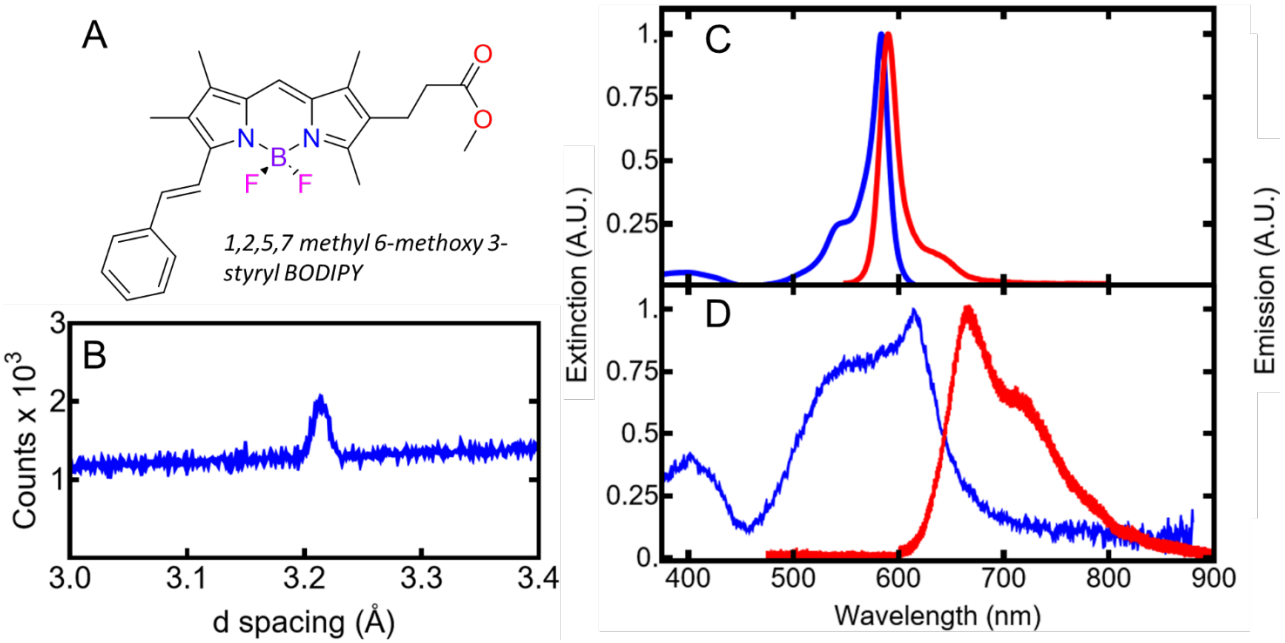

Figure 3.1: A) Molecular structure of the alpha-styryl BODIPY. B) XRD pattern of the thin film. The ground state absorption (blue) and emission (red) for solid-state wires (C) and solution-phase (D).

To prepare the BODIPY nanoribbons, the molecular BODIPY was dissolved in toluene (50 μM) and dropped onto a borosilicate microscope slide. The solvent was then allowed to evaporate in an atmosphere containing air and vaporized toluene at room temperature. This process produces characteristic "coffee-ring" type patterns, which reflect the complicated interplay of many parameters during the drying process, e.g. droplet size, temperature, solvent viscosity, and surface tension.[136] For SEM imaging samples, this procedure was repeated except with a silicon substrate to mitigate charging effects. To generate an adequately dense sample for thin-film XRD analysis, a highly concentrated sample at 23 mM was prepared using the above methods.

To characterize the structure of the self-assembled BODIPYs, we turned to x-ray diffraction using the grazing incidence geometry. Due to the nature of the experiment requiring significant order to obtain an x-ray pattern, a "thick film" was prepared by drop casting a highly concentrated precursor on a glass coverslip (phase contrast image of this sample is in Figure 3.2F). The XRD pattern in Figure 3.1B reveals a single peak at 27.74° that corresponds to an interplanar spacing of 3.21 Å. Note that although patterns were collected from 5-50° 2Θ, there were no peaks observed at shallower angles, indicating we only observed 1D crystallinity. The close interplanar spacing indicates a close-packed arrangement of the monomers and that there is significant order resulting in a coherent scattering pattern that arises from the rods. Bright-field microscope images taken in the location where the XRD experiments were conducted confirm that the XRD pattern is representative of the rods measured in the spectroscopic studies described below (see supporting information, Figure A2).

Panels C and D of Figure 3.1 correspond to the absorption and emission spectrum of the solution-phase monomer and solid-state ribbon, respectively. Molecular aggregates tend to couple their electronic states and orient themselves in an H- or J-like orientation. In an H-like orientation, the transition dipole moment is aligned co-facial, and in a J-like orientation, side-by-side. This aggregation will manifest itself spectroscopically in that H-aggregates have an optically forbidden relaxation from the lowest energy state and J-aggregates have an optically allowed transition from the lowest energy state.[27-29, 32] H- and J- aggregates will also result in an absorption spectrum that is shifted relative to the monomer: red shifted for J-aggregates and blue shifted for H-aggregates. The solution-phase monomer absorption (fig. 3.1D) exhibits typical features of a 5-Styryl methylated BODIPY molecule with the S_0-S_2 at 400 nm and S_0-S_1 around 550 nm consisting of

the vibronic transitions at 584 nm for the (0-0) and 542 nm (0-1).[137, 138] Using a homebuilt absorption microscope with a spot size <5 μm, we were able to determine that the nanoribbons exhibit most features almost identical to that of the monomer, with the exception that there is a major redshift to 614 nm and broadening of the lowest energy transition (fig. 3.1C). While the 105.7 meV red shift indicates that the monomer self-assembles with the transition dipoles aligned head-to-tail relative to nearest neighbors (i.e. J-type aggregation), evidence of broadening of the higher energy peaks may indicate a more complex coupling arrangement such as HJ-type coupling,[139] I-type coupling,[57] or X-type coupling.[140] The red traces in Figure 3.1 C, D correspond to the emission spectra of the solution-phase monomer and the emission from a single wire (λ_{ex}= 580 nm), respectively. The solution-phase exhibits emission peaks that mirror the absorption spectrum with a peak at 591 nm and a shoulder at 643 nm (Stokes shift of 25 meV). The emission from the wire is significantly red shifted compared to the absorption spectrum with the major emission peak at 660 nm and a shoulder at 720 nm (Stokes shift of 121 meV). Standard methods for classifying the type of coupling in aggregates rely primarily on solution-phase spectroscopic shifts, resulting in a crystal packing structure that can only be inferred. Regardless, the red-shift in the absorption spectrum and emissive nature of the ribbons indicate that there is strong coupling of the BODIPY monomers upon solid-state deposition.

Microscopy

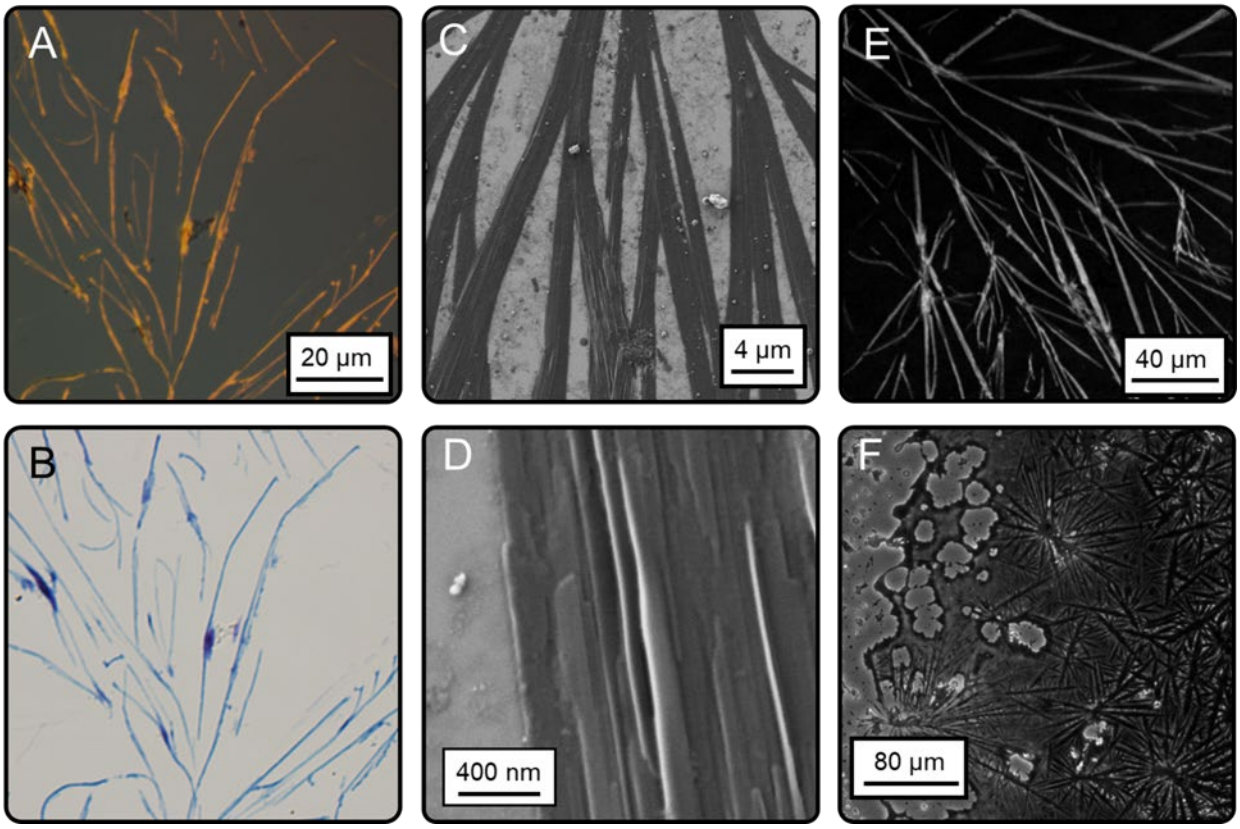

Figure 3.2: Bright-field microscope images of the self-assembled nanoribbons in A) reflective mode, highlighting a reflective gold color and B) transmissive mode. C) and D) are representative SEM images, detailing the complex nanostructure of the ribbons. E) Emission confocal microscope image of the nanoribbons excited at 580 nm. F) Phase contrast microscope image of the needle-like structure that arises from a highly concentrated precursor.

Bright-field microscopy reveals interesting characteristics about the microstructure of the drop cast BODIPY. Using the microscope's reflectance mode (fig. 3.2 A) the BODIPY monomers appear to self-organize into long wires ~100 μm in length and up to 2 μm in width. The reflected light highlights a metallic gold color with needle-like structures. In transmission mode (fig. 3.2B), wires mostly appear to be blue with areas of purple, consistent with the absorption spectrum. Turning to scanning electron microscopy (SEM) which allows us to visualize the structure of the

wires below the diffraction limit, Figure 3.2C shows that the self-assembled BODIPY materials organize themselves into thin ribbon-like structures with a complex nano-scale structure consisting of a tree bark-like pattern (fig. 3.2D).

The redshifted ground state absorption spectrum suggests the nanoribbons exhibit J-type coupling. To determine that this was the case and not a manifestation of low-energy trap sites, we turned to confocal emission microscopy (fig. 3.2C). The samples were excited from 435-680 nm and the photoluminescence was integrated at and above 696 nm. The resulting image stack shows a similar intensity dependence on the excitation wavelength that resembles an excitation spectrum (fig. A2.A). To simulate a pseudo excitation spectrum, the integrated PL intensity of each image was plotted as a function of wavelength (fig. A2.B). Interestingly, the excitation spectrum resembles the ground state extinction spectrum of a single nanoribbon. The emissive nanoribbons and redshift in the ground state absorption spectrum in conjunction with each other confirm J-type electronic coupling.

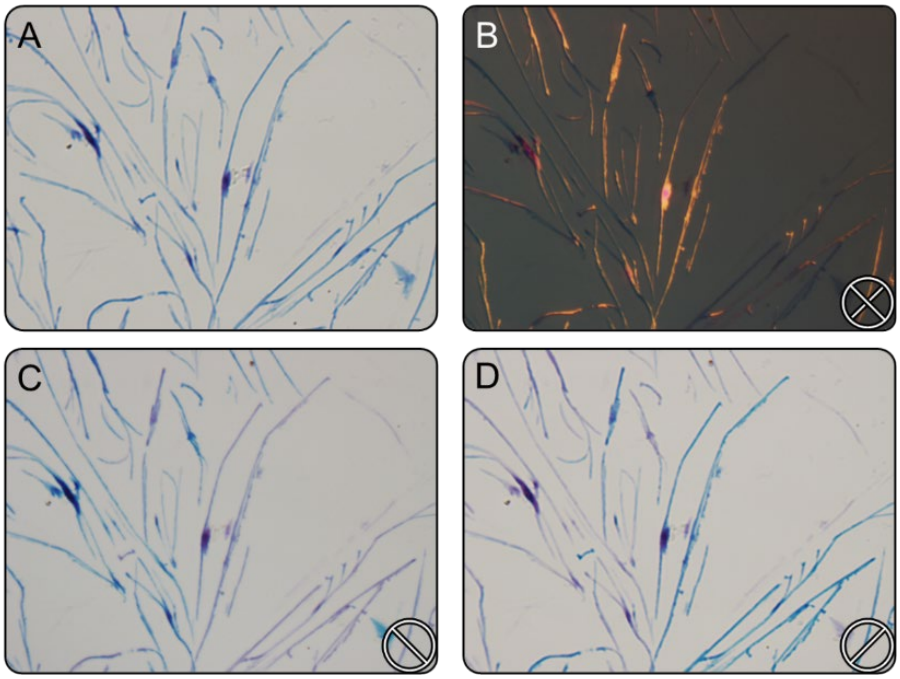

Figure 3.3: Transmissive emission microscopy with an ROI focused on the ribbons. Panel A) is unpolarized light, and B) crossed polarized light. and C) and D) correspond to linearly polarized light. The polarization direction is in the bottom corner.

Highly ordered (and crystalline materials) will often exhibit absorbance that is strongly dependent on the polarization of light. Bright-field cross-polarization images (Figure 3.3) reveal that the self-assembled ribbons exhibit a high degree of anisotropy which often is not observed in materials that rely on rapid evaporation as a solid-state deposition technique.[141] To quantitatively measure the anisotropy, we measured the degree of linear dichroism and orientation angle of the ribbons on a home-built laser microscope. Briefly, we selected the polarization of the beam at 580 nm to be parallel with the ribbon and then raster scanned the beam over the sample. Using a photodiode, the intensity of the beam was measured at each pixel. The degree of linear dichroism (or orientation parameter, S, that ranges from -0.5 to 1)[142] is defined as $S=(I_{\parallel} - I_{\perp})/I_{iso}$, where the I is the intensity measured, and the subscripts denote the polarization of the beam (relative to the

ribbon) and I_{iso} is the isotropic intensity (further details in the SI).[143] The orientation parameter also carries information about the transition dipole vector orientation (θ) with respect to the ribbon and a fixed coordinate system (model details in the supporting information).[144] The ribbon has a mean value of 0.30 ± 0.14 whereas the background exhibits a negative value of -0.11 ± 0.04, suggesting that there is little anisotropy off of the ribbon (fig. A4). The orientation of the transition dipoles shows that the ribbon exhibits a mean orientation angle of 58.9° ± 1.7° (fig. A5), which is consistent with J-aggregation. [144-146] While it is challenging to determine the crystal packing structure without single crystal X-ray crystallography, the orientation angle, along with the interplanar distance measure in the XRD experiments, give further insight into the structural arrangement of the molecules.

Ultrafast Spectroscopy and Microscopy

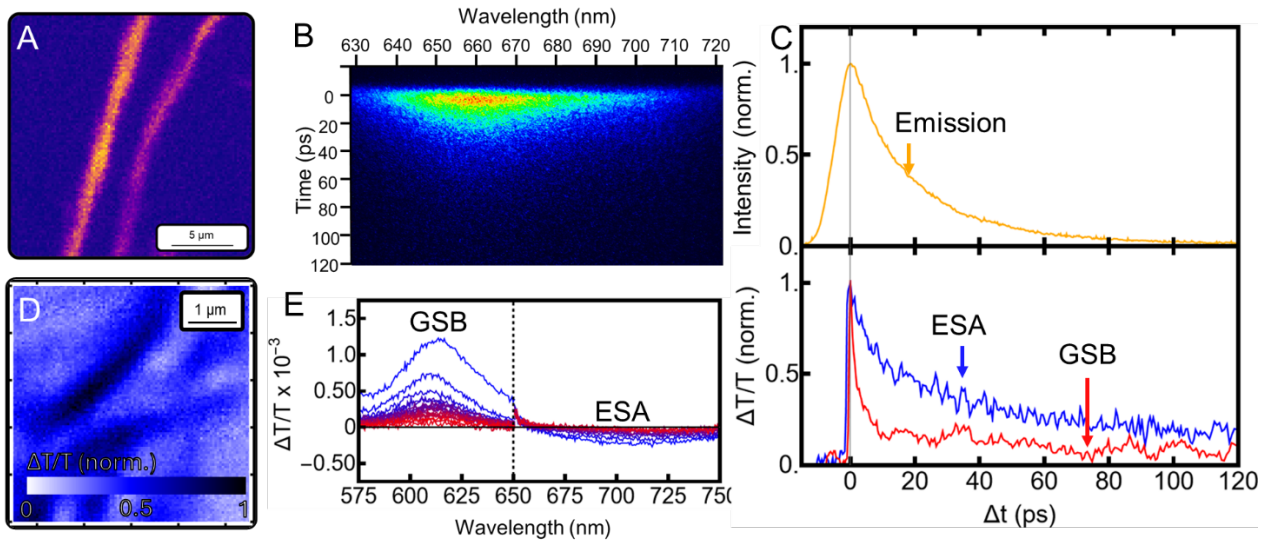

Figure 3.4: Panel A) corresponds to an integrated emission image of the nanoribbon and D) corresponds to a pump probe microscope image. Panel B highlights the transient emission spectra over time and E) is the transient absorption spectrum from early times (blue, 0 ps) to late times (red 120 ps). The ground state bleach (left) and excited state absorption (right) are also highlighted. Panel E corresponds to the integrated signal (660 ± 5 nm) as a function of time for the emission (top) and transient absorption (bottom).

To gain insight into the material's excited state dynamics, we turned to spatially resolved spectroscopies. Time-resolved photoluminescence (TRPL) experiments were conducted using a homebuilt microscope coupled to a streak camera. The instrument is capable of measuring an integrated emission signal on a pixel-by-pixel basis to produce a spatial map of emission (Figure 3.4 A, note that the image is scaled to the highest pixel value at yellow) as well as a time-integrated emission spectrum (Figure 3.1D, red) from individual ribbons. The time-resolved emission spectrum in Figure 3.4 B shows that emission from the BODIPY nanoribbon decays at the same rate regardless of the wavelength (homogeneous decay). The kinetics shown in Fig. 3.3E show the

PL decay, integrated from 555 to 665 nm. Kinetic fits show the PL decays double exponentially with lifetimes of 13.31 ps and 36.291 ps ($\langle\tau\rangle$=20.09 ps); note that the short lifetime is in the interment response (FWHM ~9 ps).

Time-resolved photoluminescent studies give insight into the emissive relaxation from the band edge. Broadband pump probe microscopy (BBPPM) can probe the material further by gaining insight into non-emissive pathways. Broadband experiments were performed on an individual ribbon using a 517 nm pump and a broadband (500 - 750 nm) probe. Figure 3.3E shows a ground state bleach from ~ 575 to 655 nm and broad excited state absorption from 655 to 750 nm. The ground state bleach exhibits a slight blue shift from 613.57 nm (2.021 eV) to 607.39 nm (2.041 eV) over the first 10 ps (Figure A7, SI). Since the aggregate exhibits lower energy than the monomer, we are tentatively assigning the 19.9 meV blueshift to the localization of the exciton over this time frame. The excited state absorption decays nearly homogeneously, indicating that the excited states such as Frenkel-CT exciton mixing,[147, 148] excimer stabilization,[149] and/or self-trapping[150] do not contribute to this decay, but rather the excited state is excitonic in nature. The decay kinetics for both the GSB and ESA (Fig. 3.3 E) were fit to a biexponential decay function with an average lifetime calculated as $\langle\tau\rangle = (a_1\tau_1 + a_2\tau_2)/(a_1 + a_2)$. The decay in ground state bleach was measured by integrating the signal at 615 ±25 nm, resulting in a rapid decay lifetime of 2.2 ps and a longer lifetime of 157.6 ps ($\langle\tau\rangle$ = 41.187 ps). The ESA spectrum was fully integrated, resulting in a short lifetime of 9.06 ps (a_1=0.541) and a long lifetime of 113.24 ps (a_2=0.468, $\langle\tau\rangle$ = 57.38 ps).

Two Color Pump Probe Microscopy

Ultrafast two color pump probe microscopy experiments provide the means to measure ultrafast dynamics with sub-micron spatial resolution and directly measure exciton transport that broadband pump probe microscopy cannot, due to inherent instrumental constraints. For these experiments the pump was selected from a generated white light continuum with a 580 nm bandpass filter, roughly where the monomer has its maximum extinction. The probe was set at 750 nm to probe the excited state absorption band as previously determined using transient absorption. To eliminate nonlinear recombination processes that would contribute to the kinetics and minimize sample damage, we limited our excitation fluence to 203.5 μJcm^{-2} By measuring the excited state dynamics in different locations, we found all locations on the ribbon to be homogenous in their decay (Fig. 3.4 A, B). Fitting to a biexponential decay function we found that the fast lifetime is 4.25 ± 0.91 ps and the longer lifetime is 69.76 ± 12.61 ps ($\langle\tau\rangle$ = 29.4 ± 4.33). The rapid relaxation is in good agreement with other J-aggregated systems.[151, 152]

Pump probe dichroism provides a means to determine if there is a change in the transition dipole moment upon photoexcitation. To conduct these measurements, we compared the transient signal (at Δt = 0ps) and mapped the spatial response as a function of the polarization of both the pump and probe beams (fig. A8 A-D). Additionally, we measured the transient response by spatially overlapping the beams and monitoring the kinetic decay (Figure 3.4C). The spatially resolved images and decay kinetics reveal identical trends: 1) signal intensity is strongest when pump and probe polarizations are in the direction of the ribbon, indicating that the material's transition dipole moment for both the S_0 to S_1 and S_1 to S_2 has a strong preference for polarizations that are parallel to the ribbon. 2) The signal is approximately half as strong (48%) when the pump is orthogonal to the ribbon when compared to the parallel-parallel configuration. 3) The signal

significantly drops (11%) when both the pump and probe are orthogonal to the ribbon. The trend described above suggests that the S_1 transition dipole moment heavily favors excitation in the direction of epitaxial growth.

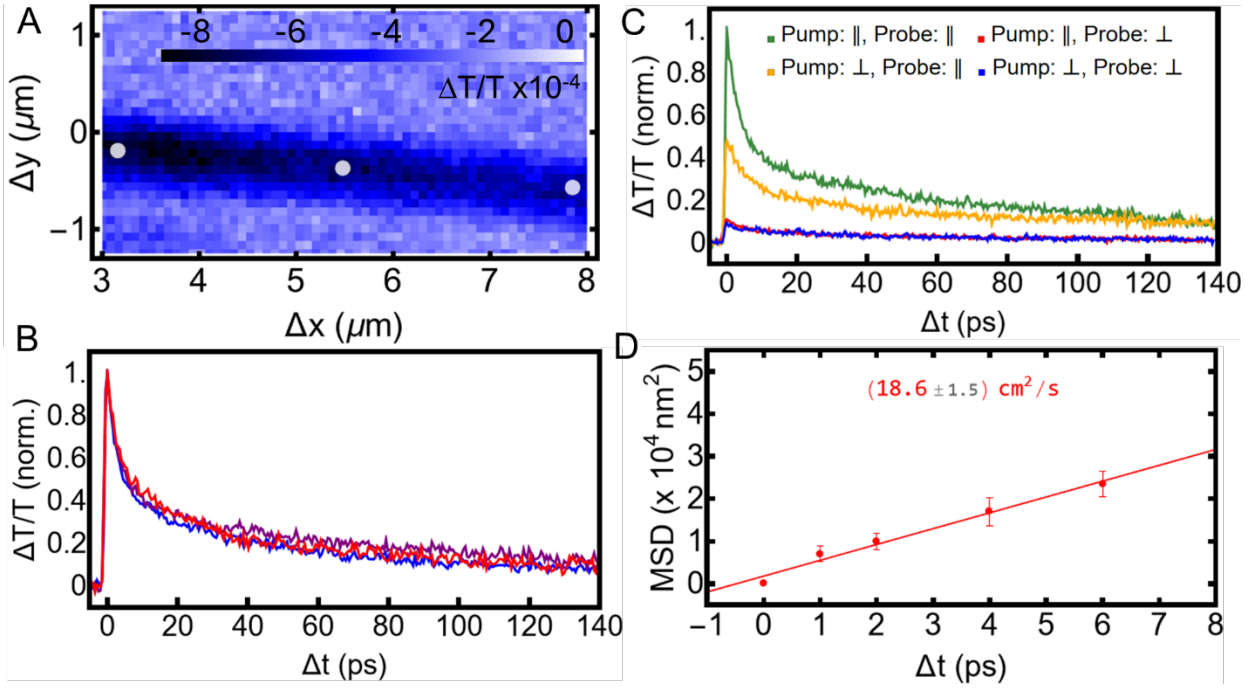

Figure 3.5: A) Pump probe microscope image of a nanoribbon with the three locations measured for kinetics depicted in (B). C) Kinetics measured as a function of pump and probe polarizations when parallel and perpendicular to the nanoribbon growth direction. The traces are normalized to the signal intensity when both beams are parallel with the ribbon. D) Ultrafast diffusion measured on the BODIPY nanoribbons.

Together with the crystalline morphology of the ribbons and the transient absorption experiments suggesting that the excitons localize in the first 10 ps after photoexcitation, we suspected that there may be fast coherent exciton transport.[153] Literature on exciton transport in J-type aggregates has shown that these types of materials are capable of this fast transport. [154-157] To measure transport in the ribbons, we next turned to spatially offset pump probe microscopy. For these measurements, the probe beam is fixed in a location on the ribbon and the pump beam is

raster scanned over the probe, allowing us to image the pump-induced response of the probe as a function of time. A series of these images were collected at increasing Δt between 0 and 100 ps and allows us to image excited state transport only limited by signal-to-noise.[158] Because the nanoribbons are ~1 μm wide and are only slightly larger than the convolution of the pump and probe beams (~700 nm), measurements were only taken in the direction of the ribbon. The average 1D spatial profile was fit by numerical convolution of the diffusion kernel with the initial Δt_0 spatial profile to determine the mean squared deviation (MSD) of the excited state profile.[159]

We observed extremely fast exciton diffusion in the first 10 ps in eight locations on different ribbons. Of the measurements with the most reliable fits (fig. A11), we measured an astonishing diffusion coefficient of 14.37 ± 2.79 cm^2s^{-1} (histogram in supporting information fig. A12). Although the standard deviation of 2.79 cm^2s^{-1} is high, site-to-site heterogeneity is a reasonable explanation for this variance. Spatially overlapped images (fig. S9A-B) and SEM images suggest that the ribbons are not perfectly smooth and single crystalline, but rather have perturbations in their crystal growth which may slow down exciton diffusion. Beyond 10 ps, the signal amplitude decays rapidly lowering the contrast-to-noise (due to exciton recombination and transport), thus making measurements beyond 10 ps unreliable when calculating diffusion coefficients.[124] The diffusion coefficients determined on the BODIPY ribbons have a similar order of magnitude as the diffusion measured in nanotubes comprised of porphyrin J-aggregates; here, Wan et al. report a diffusion coefficient of 6.4 cm^2/s.[151] While we have measured rapid diffusion in alpha styryl BODIPY ribbons, it is not uncommon for J-aggregates to exhibit similar rapid rates (even upwards of 50 cm^2s^{-1})[7] because of a mixture of coherent and hopping-type transport with large exciton delocalization (over ~10 monomers).[151, 152, 160]

Conclusion

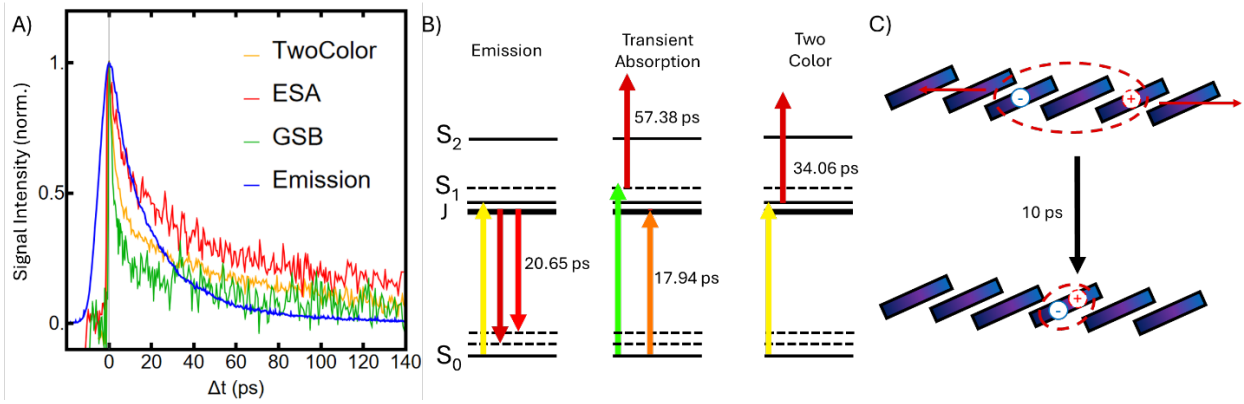

Figure 3.6: Panel A depicts the accumulation of the kinetic traces from all the ultrafast experiments. Panel B depicts the energy level diagrams of emission, broadband transient absorption, and two color transient absorption. The excitation arrow on the left corresponds to the excitation wavelength; 580 nm for yellow and 517 nm for green. Note that the spacing between the energy levels and the length of the arrow directly correspond to the energy differences measured spectroscopically.

The solid-state deposition of the 3-styryl-BODIPY monomer resulted in long ribbon-like crystals. Emission and extinction microscopies reveal the strong J-type electronic coupling via the evidence of the emission in the solid-state at 660 nm as well as a spectral redshift from 583 nm to 614 nm. The collection of ultrafast experiments shows a complex energy landscape of the BODIPY ribbons; the emission, excited state absorption (two color and broadband), and ground state bleach lead to very different relaxation lifetimes (Figure 3.5A and Table 3.1). From the ground state absorption and ultrafast spectra/relaxation lifetimes, we were able to construct a simplified energy level diagram (Figure 3.6B) that depicts the energy states (solid lines), the vibronic level (dashed) and the lower "J-Band" that is formed from aggregation (solid). When excited/pumped at 580 nm the emission and two color lifetimes result in similar relaxation rates to each other, however when pumped at 517 nm, the excited state lifetimes are very different from the lower energy excitation.

One would expect that the excited state absorption in broadband and two color experiments would result in similar lifetimes, but we observed that when pumped at 517 nm the average lifetime is double than when pumped at 580 nm. This suggests that when pumping at 580 nm, we are pumping closer to the "J-state"[161] and that this state is more coupled with the ground state versus the S_1 state, allowing for faster relaxation. The ground state bleach decays rapidly compared to the excited state absorption from both excitations. While the exact mechanism behind rapid ground state bleach decay is elusive, the combination of exciton localization and fast transport provides a reasonable explanation for this observation (fig. 3.5C).

CHAPTER FOUR

FROM MONOMERS TO AGGREGATES TO SOLID-STATE FILMS: SPECTROSCOPIC INSIGHT ON ZINC PORPHYRIN H-AGGREGATES

Contribution of Authors and Co-Authors

Manuscript in Chapter 4

Author: Alexander J. King
Contributions: Formal analysis, investigation, methodology, software, writing-original draft, writing-review & editing.

Co-Author: Emma K. Orcutt
Contributions: Formal analysis of solution-phase pump probe data.

Co-Author: Ifigeneia Tsironi
Contributions: Assisted with synthesis.

Co-Author: Joseph J. Thiebes
Contributions: Assisted XRD experimentation and software programming.

Co-Author: Jean-Hubert Olivier
Contributions: Conceptualization, formal analysis, funding acquisition.

Co-Author: Erik M. Grumstrup
Contributions: Conceptualization, formal analysis, funding acquisition, methodology, project administration, software, supervision, writing-original draft, writing-review & editing.

Manuscript Information

Alexander J. King, Emma K. Orcutt, Ifigeneia Tsironi, Joseph J. Thiebes, Jean-Hubert Olivier, Erik M. Grumstrup

Journal of Porphyrins and Phthalocyanines

Status of Manuscript:
☒ Prepared for submission to a peer-reviewed journal
☐ Officially submitted to a peer-reviewed journal
☐ Accepted by a peer-reviewed journal
☐ Published in a peer-reviewed journal

Journal of Porphyrins and Phthalocyanines

Abstract

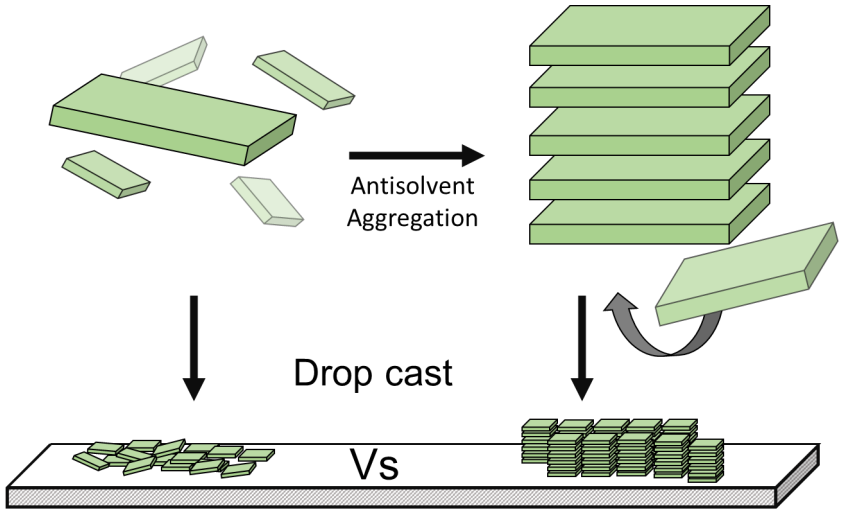

There has been great interest in using porphyrin-derived materials as organic semiconductors because of their application in photovoltaics, chemosensors, flexible electronics, and light-emitting diodes. Fabricating materials that originate from organic molecules proves to be challenging because of the weak noncovalent interactions that dictate the self-organization of the molecules. In this work, we provide a compelling strategy to mitigate electronic and structural heterogeneity upon solid-state deposition by pre-aggregating the porphyrin monomers via antisolvent aggregation. Monomer aggregation was confirmed via a hypsochromic shift in the absorption, and the photophysical properties of the monomer and aggregate were compared. To determine the effects of aggregation prior to solid-state deposition, we turned to ultrafast microscopies to measure excited state lifetime. From our results we have shown that excited state lifetime is correlated with structural homogeneity; homogeneous films exhibit a narrow distribution of short lifetimes whereas heterogeneous films exhibit a wider distribution of lifetimes.

Thus, pre-aggregation prior to solid-state deposition improves structural homogeneity in porphyrin-derived thin films.

Manuscript

Introduction

Materials derived from porphyrins via self-assembly have been shown to be excellent photocatalysts[162] and organic field-effect transistors (OFETs)[163] because of their ability to form highly crystalline structures and close π-π stacking distances. Since the structural arrangement and photophysical properties are heavily linked,[164] these molecular systems have been a challenge to implement in a functional device. One of the underlying knowledge gaps in the organic semiconductor field is the translation from the solution-phase to the solid-state.

In this manuscript, we report a spectroscopic comparison of two materials derived from the same porphyrin precursor. In one sample, the thin film is cast from a solvated monomer solution. In the other sample, the film is cast from dispersed, self-assembled aggregates. Our aim with this comparison is to determine the extent of heterogeneity that is inherent to solid-state deposition via drop casting. We found that by pre-aggregating the porphyrin monomers, the electronic and structural heterogeneity is mitigated in the solid-state. We have also shown through the use of ultrafast microscopies that the lifetime of the excited state is highly correlated with the degree of structural order. Films prepared from the aggregate precursor exhibit a shorter and more homogeneous distribution of lifetimes when compared to films prepared from the monomer. Additionally, we measured the degree of linear dichroism and found that the pre-aggregated films exhibit isotropic dichroism whereas the films prepared from the monomers are highly anisotropic.

These results suggest that solution-phase processing via aggregation prior to solid-state deposition is a compelling strategy for increasing structural homogeneity in the solid-state.

Synthesis and Characterization

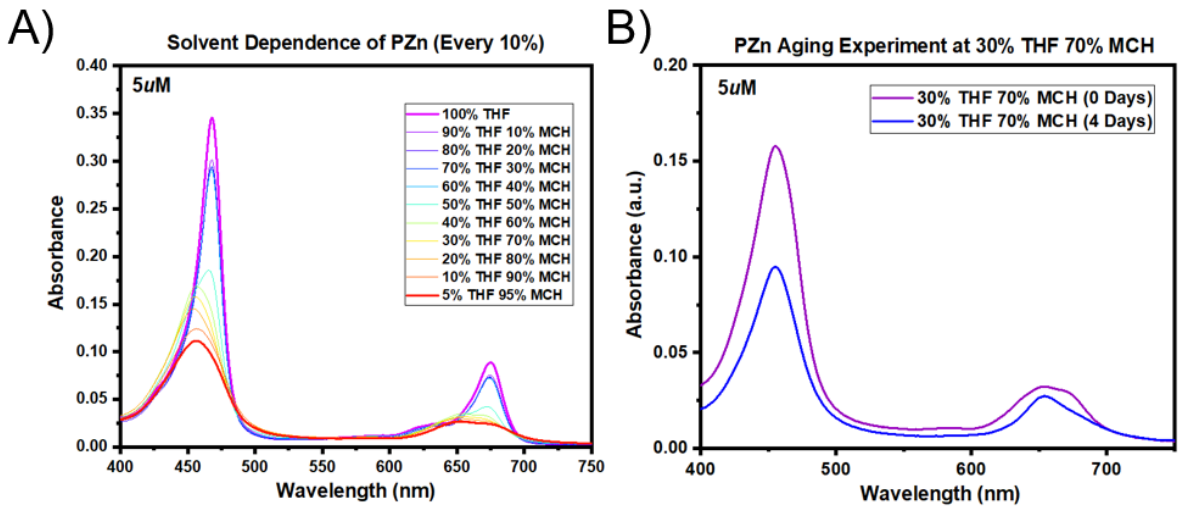

Figure 3.1: Absorption spectra of the aggregation of PZn monomers at (A) various solvent compositions and (B) over four days of aging.

To compare the effects of aggregation in solution before solid-state deposition against a material that is deposited directly from dissolved molecular building blocks, the zinc porphyrin (PZn, fig. 4.2A) samples were prepared in two ways. In the first preparation, the pure monomer was fully dissolved in THF (50 μM). In the second preparation, the monomer was dissolved in THF, and methylcyclohexane (MCH) was added until the solvent composition reached 30:70, THF:MCH (50 μM) and allowed to age for five days. To determine the degree of aggregation and optimal aggregation conditions, solution-phase absorption studies were performed using different ratios of solvent and antisolvent from 100% THF to 5% THF 95% MCH (inset of fig 4.1A). The blue shift and the broadening in the Soret band show that the monomer is sufficiently aggregated.

At solvent compositions with more than 70% antisolvent, the aggregates start to crash out of the solution. To ensure that the monomers completely aggregate, the solution was aged for a minimum of four days. Figure 4.1B shows the red edge of the q-band diminishes over the four days of aging, indicating that sufficient time is required to ensure complete aggregation.

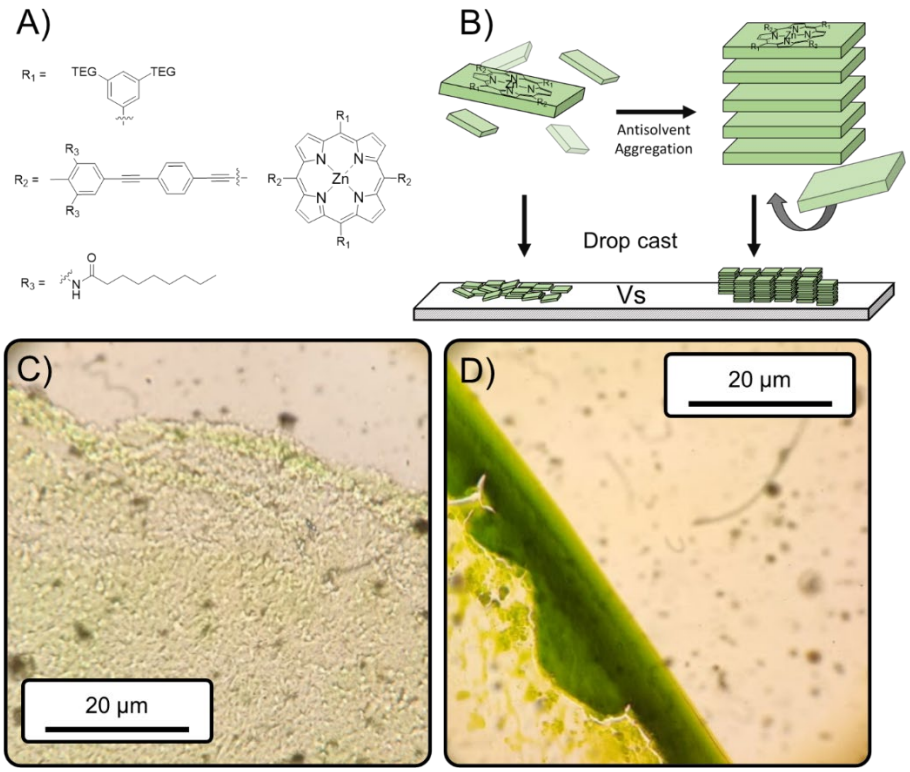

Figure 4.2: A) Chemical structure of the zinc porphyrin monomer. B) Scheme of direct deposition from monomer to solid-state and monomer to aggregate to solid-state. Panels C and D show bright-field microscope images of the monomer and pre-aggregated films, respectively.

To prepare films of the aggregate and molecular precursors, 40 uL of each solution was drop-cast onto a glass slide and allowed to evaporate under ambient conditions for 30 minutes. The evaporation process produced thin films of the material in a ‘coffee ring’ like pattern.[20, 21] Bright-field microscope images were taken of both films as seen in Figure 4.2. Panels C and D

correspond to the films derived from the monomer and pre-aggregate, respectively. These figures highlight the heterogeneous nature of drop casting the dissolved monomer, with the film consisting of regions with high and low transmission. However, turning to the film composed of the aggregate, the edge of the coffee ring exhibits a nearly homogeneous film at the edge. By microscope inspection is clear that aggregation plays a key role in homogeneous structural formation.

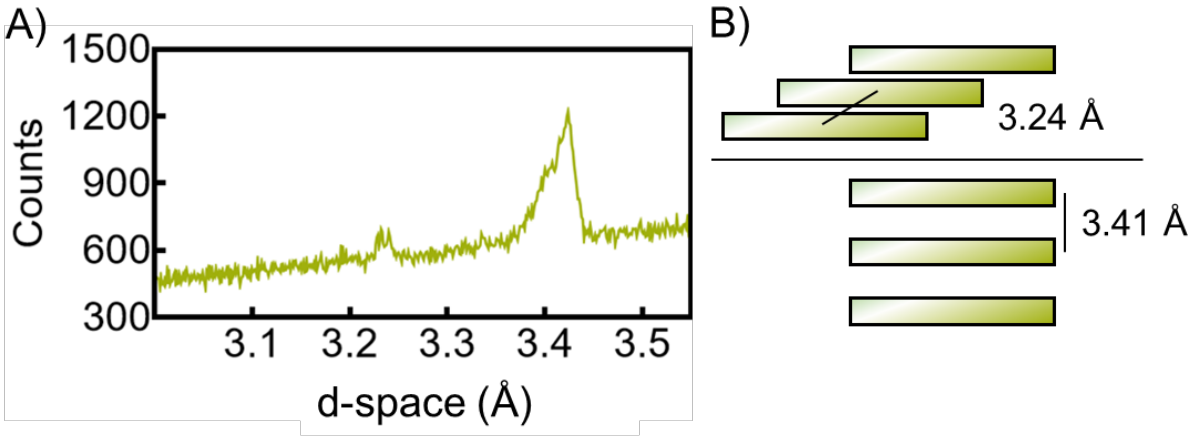

Figure 4.2: XRD pattern of a film prepared from dissolved monomer (A) and a cartoon representation of the packing arrangement (B).

To characterize the structure of the films, we next turned to X-ray diffraction using the grazing incidence diffraction geometry. The XRD pattern for the film composed of the monomer revealed two broad peaks at 3.24 Å (27.65º) and 3.41 Å (26.15º). The close packing of 3.24 Å has been assigned as a slipped stack arrangement (fig 4.2B top) and the slightly longer d-spacing of 3.4 Å is assigned a π-π stack (Fig 4.2B bottom), as previously reported in the literature on H-aggregates.[165-167] Obtaining information at the molecular level can be very challenging using small angle XRD on porphyrin-based film systems, as reported by previous author's attempts.[168-170] With

diligence, we attempted to measure patterns in pre-aggregated films, unfortunately, we were unable to extract any meaningful information.

Solution-Phase: Effects of Aggregation

Our aim in this study is to determine the extent of heterogeneity that is inherent in drop-cast organic materials. We studied the effects of drop casting from the dissolved monomer and the aggregated form of the monomer as depicted in Figure 4.2 B. Before studying the solid material, we characterized the solution-phase photophysics of the two precursors.

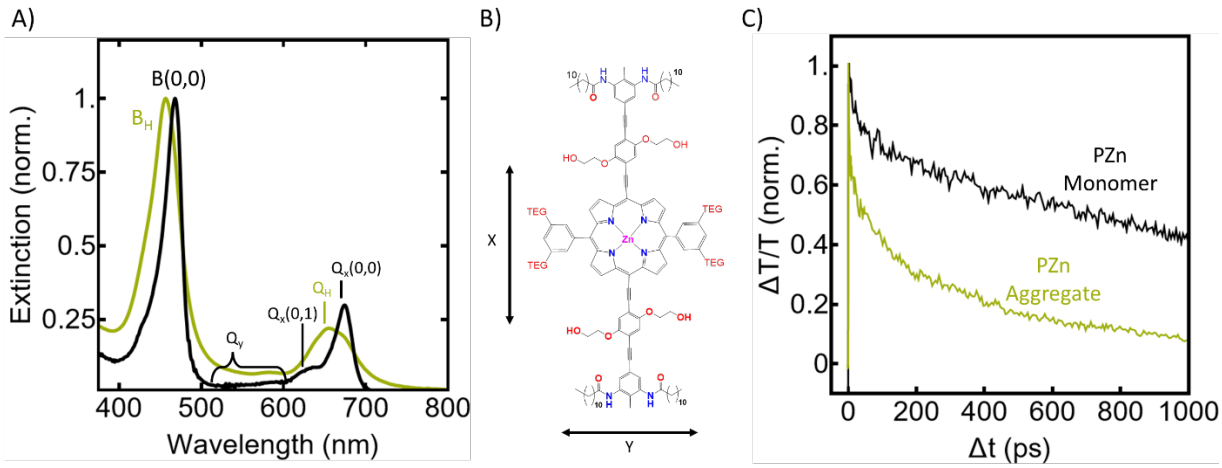

Figure 4.3: Panel A shows the solution-phase absorption spectra for the monomer (black) and aggregate (green) and their respective band assignments. Panel B is the PZn monomer and the assignment of the X and Y directions. Panel C is the excited state decay kinetics out to 1000 ps for the monomer (black) and aggregate (green).

The ground state absorption gives insight into the electronic structure of the porphyrin monomer and the aggregated porphyrin. The absorption spectra (Figure 4.3A) were measured in THF for the monomer and 3:7 THF/MCH for the aggregate. The dissolved monomer features a Soret band at 469 nm with a shoulder at 429 nm, these bands correspond to the $S_2 \leftarrow S_0$ electronic transition with B(0-0) and B(0-1) vibronic transitions, respectively.[171] The $S_1 \leftarrow S_0$ transitions at

584, 627, and 675 nm have been assigned as the Q_y, $Q_x(1,0)$, and Q_x (0,0), respectively. The Q_y band typically features the (0-1) and (0-2) vibronic transitions, however, the low oscillator strength makes it challenging to properly resolve and assign these transitions. The resolvable features are in good agreement with zinc porphyrins with a D_{2h} symmetry.[87, 90, 172] The H-aggregation of the PZn molecule was confirmed by the hypsochromic shift from 469 nm to 458 nm resulting in an overall S_2 destabilization of 64 meV, and this band is assigned at the B_H band. The Q_H-band has subtle features at 584, 635, 656, and 675 nm. While it is challenging to determine the assignment for each of the bands within the larger Q_H-band because the extent of coupling is unknown, the band broadening and hypsochromic shifts are indicative of H-aggregation of the PZn monomer.

Kinetic lifetime analysis provides a means to understand excited state dynamics and relaxation pathways. To study the decay of the excited state in the porphyrin monomer and H-aggregates, we utilized ultrafast pump probe transient absorption spectroscopy. Using a custom-built transient absorption spectrometer (experimental details in the supporting information, appendix B) we measured the excited state absorption at 800 nm when pumped at the edge of the Soret band at 517.5 nm. Measuring the decay over 1.5 nanoseconds (Figure 3.4C) and fitting to a multiexponential decay function, the observed decay for the aggregated PZn fits better to a triexponential decay function with lifetimes of 4, 100, and 682 ps while the monomer was best fit to a biexponential decay function with a short lifetime of 23 ps and a very longed lived lifetime of 1628 ps. The fast lifetime in the aggregated PZn indicates that a portion of the excited state decays rapidly in the first 4 ps, likely from the vibrational deactivation pathways that arise from the H-coupling of the monomers.[173] The monomer on the converse appears to lack vibrational-assisted relaxation pathways leading to the long lifetime of 1628 ps. While it is challenging to assign a

physical meaning to the decay pathways hidden in a triexponential function without a full spectral analysis (such as triplet state formation), its often more useful to describe the excited state lifetime as an average lifetime,[117] $\langle\tau\rangle = \frac{A_1\tau_1 + A_2\tau_2 + \cdots}{A_1 A_2 \ldots}$, where A_i is the exponential prefactor from the decay fit. The average lifetime we measured for the aggregate was 348 ps and 1256 ps for the monomer. The order of magnitude average lifetime difference between the aggregate and monomer PZn shows that aggregation greatly impacts the excited lifetime by accessing new deactivation pathways.

Solid-State: Precursor Comparison

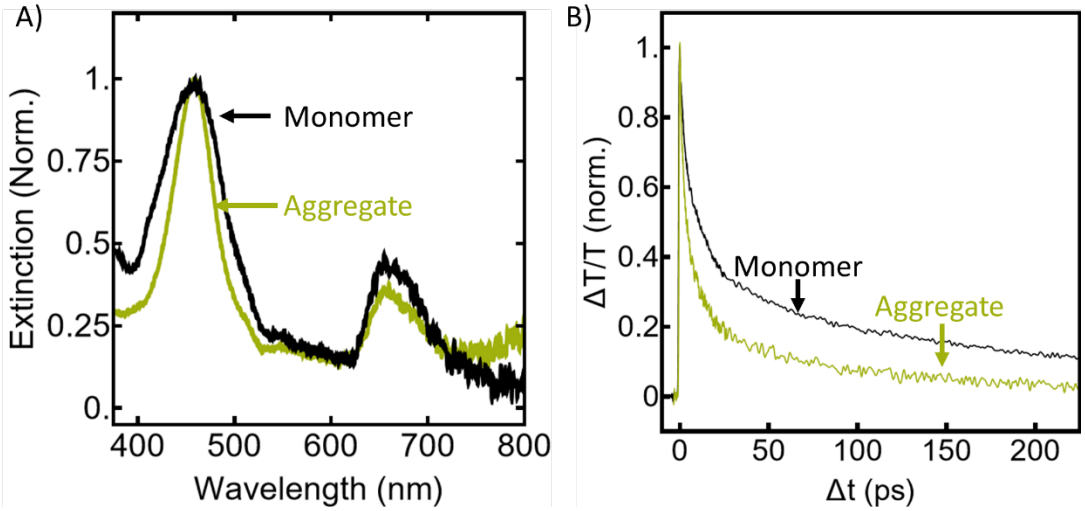

Figure 4.4: Panel A corresponds to the extinction spectra measured on the homebuilt absorption microscope and panel B corresponds to the excited state decay of the thin film prepared from the monomer (black) and aggregate (green).

The electronic band structure was determined for the solution-phase monomer and aggregate. To study the impacts of aggregation before solid-state deposition on structural heterogeneity, we first turned to ground state absorption spectroscopy using a homebuilt UV-Vis

absorption microscope with a white light spot size of ~5 μm. The solid-state extinction (fig. 4.4A) was measured on thin films prepared from the monomer (black) and a precursor prepared from the aggregated PZn (green). The peak positions are nearly identical for both films, which suggests these films strongly prefer to self-assemble in an H-like fashion regardless of whether the films were prepared from an aggregate or monomer. Interestingly, the B band at 460 nm in the aggregated film appears to be sharper than the film prepared from the monomer, which suggests that there is a greater distribution of molecular orientations in a 5 μm spot when the film is prepared from monomers, and films prepared from the aggregate are more structurally homogeneous.

From the transient absorption experiments, we were able to determine monomer and aggregate relaxation in the solution-phase. Using femtosecond pump probe microscopy (experimental details in the supporting information, appendix B), we were able to measure the relaxation in the two films. To ensure continuity between the solution-phase and solid-state experiments, the material was pumped at the edge of the Soret band at 500 nm and probed at 800 nm. The monomer film (fig. 4.4B, black) and aggregated film (fig. 4.4B, green) traces show the excited state decay out to 200 ps. Each of the traces was fit to a triexponential decay function which resulted in aggregate lifetimes of 1.6, 8.7, and 70.9 ps. The monomer had lifetimes of 2.0, 13.8, and 199.9 ps (fit data is located in Appendix B, Table B1). In the solid-state, the monomer average lifetime was measured to be 70.3 ps and 23.2 ps for the aggregated sample. The average lifetimes measured at two locations on films prepared from the monomer and aggregate show an interesting trend similar to solution-phase measurements: as the structural order of the material increases, the excited state lifetime decreases.

Ultrafast Microscopy

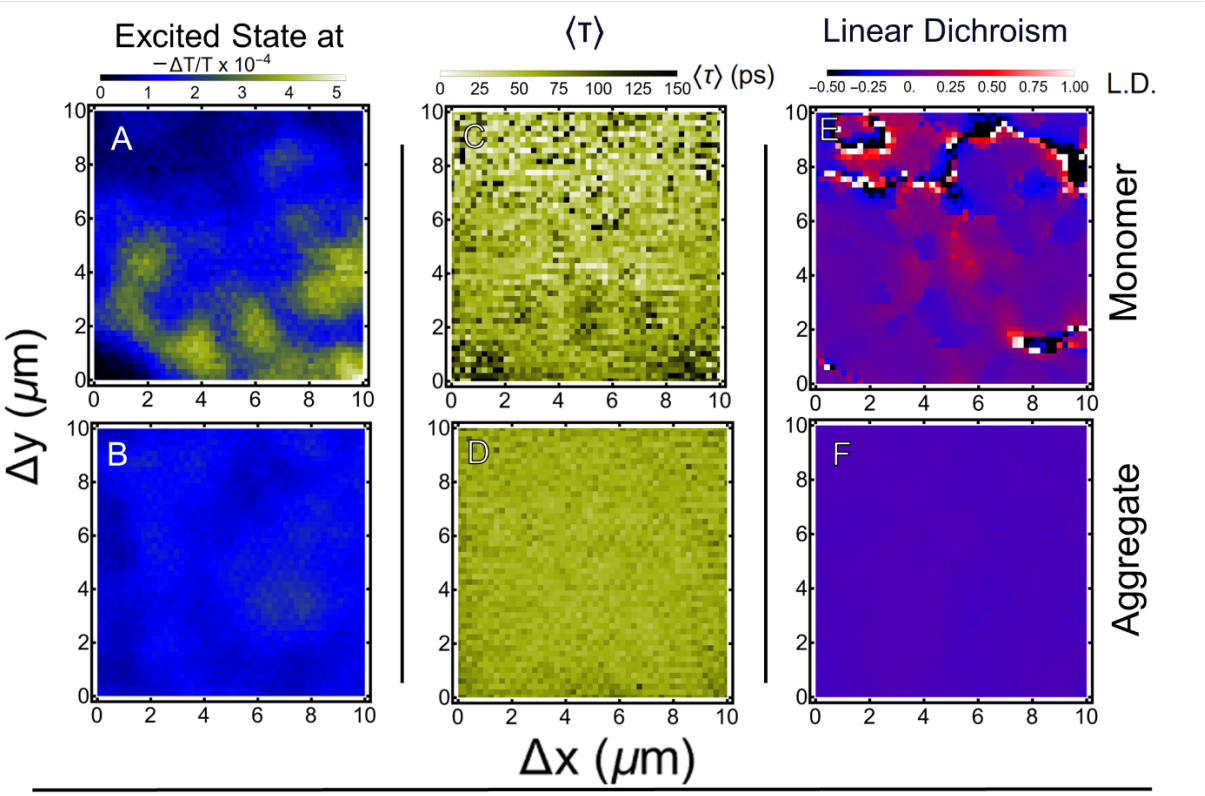

Figure 4.5: The top panel of this figure represents images of the monomer film, and the bottom panel is the aggregate. The leftmost panel corresponds to the initial t_0, the middle panel corresponds to the average lifetime, and the rightmost panel corresponds to the measure of linear dichroism. Note that all images correspond to the same ROI on the sample.

Measuring the excited state decay using the methods above affords very high temporal resolution but lacks spatial resolution. Because the pump and probe beams are confined to a single location on the material, it is challenging to determine how homogeneous/inhomogeneous the decay is over a given region. However, with the ability to raster scan the pump and probe beams we utilized Excited State Lifetime Imaging (ESLIM) to determine the homogeneity of both films. The tradeoff here is the opposite of standard kinetic measurements; this method allows us to measure the lifetime on a pixel-by-pixel basis, but it fails to result in high-temporal resolution.

Regardless, this technique is sufficient to determine the homogeneity in the material's excited state. To measure the excited state as a function of space in the monomer and pre-aggregated films, the pump and probe beams are spatially overlapped and then raster scanned over the region of interest, this is then repeated at various pump probe delay times to build up an image stack. The ΔT/T signal at each pixel is then plotted as a function of time and fit to a biexponential decay function. A biexponential fit was chosen due to the lack of time resolution to resolve the fast time component in a triexponential decay. From the fitting parameters, the average lifetime is calculated as $\langle\tau\rangle = (a_1\tau_1 + a_2\tau_2)/(a_1 + a_2)$ for each pixel.[118, 174] To represent the homogeneity in the decay, we have chosen to plot the average lifetime as a function of the spatial coordinate (fig 4.4, middle panel).[175]

Figure 4.5 A, and B show an initial t_0 signal in an ROI on each of the films that is representative of a typical location on the monomer and aggregated films, respectively. As depicted in this Figure, the film derived from the monomer shows significantly more variation in the pixel intensity than the film cast from the assemblies. The monomer contains regions of high intensity (on the order $-4\text{x}10^{-4}$) down to -10^{-5} (average pixel intensity: $1.89 \pm 0.85 \text{ x } 10^{-4}$). The pre-aggregated sample, however, is highly homogeneous in the signal intensity with an average pixel intensity of $1.46 \pm 0.21 \text{ x } 10^{-4}$ (histograms for pixel data in the supporting information, appendix B, Figure B2). Characterizing the films solely based on signal intensity can lead to misinterpretations in structural homogeneity since some regions may be thicker and will result in a higher signal and thinner regions result in a lower signal. This variability does not necessarily correlate to structural order in the film. Since measuring the lifetimes as a function of space relies on the local decay rather than signal intensity, we turned to lifetime imaging as depicted in panels C and D in Figure 4.5 to determine the relative homogeneity between the films. In these images, the pixel color

represents an average lifetime, as depicted with the scale bar. Pixels that result in a poor "goodness of fit" are set to a lifetime of 0. In the film composed of the monomer, we see that there is little correlation between the average lifetime and the signal intensity of ΔT/T. Of the 2500 pixels, 1.2% (30) of the pixels resulted in a lifetime >150 ps, and 1.0% (25) of the pixels resulted in a poor fit, with a mean average lifetime of 59.42 ± 33.38 ps (median = 57.2406 ps) for the monomer. In contrast to the film prepared from the aggregated porphyrin, the ROI exhibits a rather homogeneous lifetime with a mean average lifetime of 61.5125 ± 8.0460 ps (median=60.4112) and of these pixels, all pixels resulted in a good fit. From these results in lifetime imaging, it is evident that solution aggregation greatly improves electronic homogeneity.

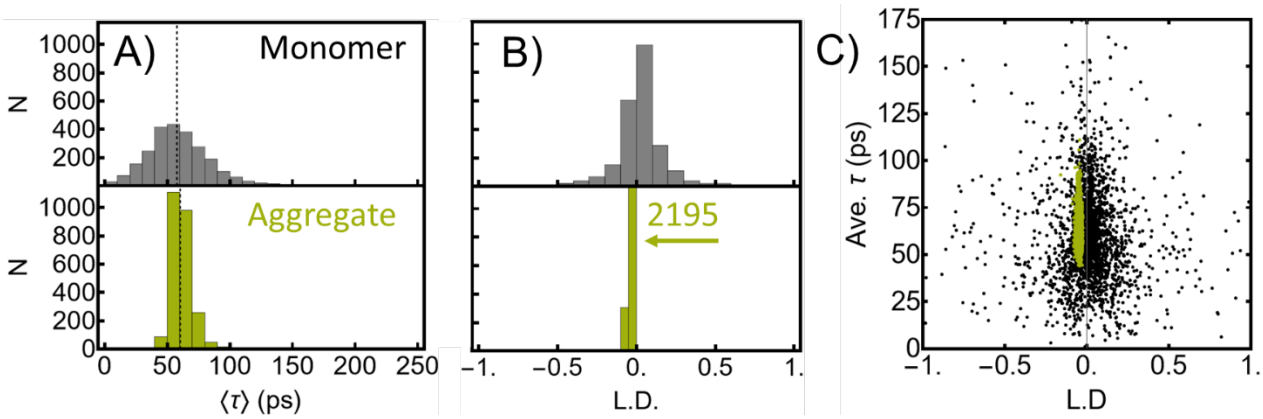

Figure 4.6: Histograms for the monomer (gray) and aggregated films (green) for the average lifetime (A) and LD (B) extracted from the pixel data in fig. 4.5. The average lifetime plotted against the linear dichroism at each pixel. Green shows the pre-aggregated film while black shows the film prepared from the monomer.

Another method for probing the structure of the thin films is spatially resolved linear dichroism. Briefly, we selected the polarization of the beam at 500 nm, and raster scanned the beam across the film and measured the intensity. At each pixel, the transmittance is plotted as a function of the polarization and fitted to a cosine function. Because the material is a film the

relative beam orientation to the crystal growth becomes arbitrary. We took the amplitude (maximum intensity – minimum intensity) of the cosine function and divided by the isotropic intensity to measure the degree of linear dichroism (LD =(I_{Max} – I_{Min})/Iiso.[142] Of the 2500 pixels we found that for the film prepared from the monomers, the mean LD was 0.0773 ± 0.1863 (median 0.0191). For the film prepared from the aggregates, we measured a mean of -0.0386 ± 0.0093 (median 0.0386). From Fig 4.5 E, F it is clear that films composed of the aggregate show very little dichroism whereas the control is largely heterogeneous. Compared to the excited state imaging (fig. 4.5 C, D), the image of the dichroism shows structure not revealed in the image of the excited state, this suggests that the orientation of the monomers varies across the film and has no correlation to how the excited state relaxes. Interestingly, the film composed of the aggregate is not centered around zero but has a slight offset (fig 4.5). Our current hypothesis is that the stacks are aligned parallel with the substrate and because of the high symmetry of the monomer (C_{2v}), the linear dichroism is not well resolved. If this is the case, then experimentally we are rotating the beam around the highest symmetry point of the molecule, so it is not unfeasible that the measured dichroism is low. However, when the monomers are not perpendicular to the beam, there is a large variation in the linear dichroism. These results ultimately suggest that by allowing the monomers to aggregate before solvent evaporation, the resulting films are highly homogeneous in pump probe intensity, excited state decay, and linear dichroism. Films prepared from simple dropping casting of monomers result in highly heterogeneous films.

Conclusion

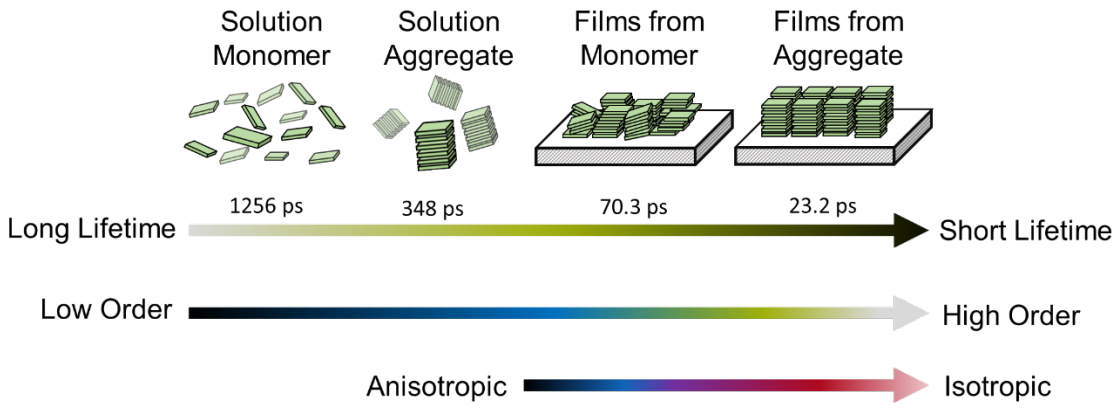

Figure 4.7: Graphical summary of chapter 4.

Fabricating materials that originate from organic molecules proves to be challenging because of the inherent structural heterogeneity that arises from self-organization. In this work, we have mitigated electronic and structural heterogeneity in the solid-state by pre-aggregating the porphyrin monomers via antisolvent aggregation. Aggregation of the PZn monomer was confirmed by the spectral shifts in the solution-phase and a notable hypsochromic shift from 469 nm to 458 nm. The solid-state extinction showed that there is significant broadening of the 469 nm peak, but no further peak shift. Turning to ultrafast studies, we have also shown that the lifetime of the excited state is highly correlated with the degree of structural order. The monomer exhibits the longest lifetime with an average lifetime of 1.26 ns, the aggregate lifetime is much shorter with an average lifetime of 349 ps, and the films show substantially faster relaxation with the film fabricated from the monomer having a 72.56 ps average lifetime and the film composed of the aggregate having a 26 ps lifetime. These results show that the lifetime decreases as the order and electronic coupling of the system increases, resulting in lifetime differences spanning two orders

of magnitude. The pre-aggregated films exhibit isotropic dichroism whereas the films prepared from just the monomers are highly anisotropic. Solution-phase processing via aggregation prior to solid-state deposition provides a compelling strategy for increasing structural homogeneity in the solid-state.

CHAPTER FIVE

COVALENTLY TETHERED ASSEMBLIES IMPROVE ENERGETIC HOMOGENEITY AND EXCITON TRANSPORT IN ORGANIC MATERIALS

Contribution of Authors and Co-Authors

Manuscript in Chapter 5

Author: Alexander J. King
Contributions: Formal analysis, investigation, methodology, software, writing-original draft, writing-review & editing.

Co-Author: Victor A. Paulino
Contributions: Synthesis of PBI locked Assemblies

Co-Author: Skyler R. Hollenbeck
Contributions: Collected broadband transient spectra for PBI samples

Co-Author: Ifigeneia Tsironi
Contributions: Assisted with synthesis

Co-Author: Jarek Maleszka
Contributions: Assisted with synthesis

Co-Author: Jean-Hubert Olivier
Contributions: Conceptualization, formal analysis, funding acquisition, project administration, writing-review & editing.

Co-Author: Erik M. Grumstrup
Contributions: Conceptualization, formal analysis, funding acquisition, methodology, project administration, software, supervision, writing-original draft, writing-review & editing.

Manuscript Information

Alexander J. King, Victor A. Paulino, Skyler R. Hollenbeck, Ifigeneia Tsironi, Jarek Maleszka, Jean-Hubert Olivier, Erik M. Grumstrup

Status of Manuscript:
☐ Prepared for submission to a peer-reviewed journal
☐ Officially submitted to a peer-reviewed journal
☐ Accepted by a peer-reviewed journal
☒ Published in a peer-reviewed journal
.

ACS Materials Letters:
DOI: 10.1021/acsmaterialslett.4c00279

Abstract

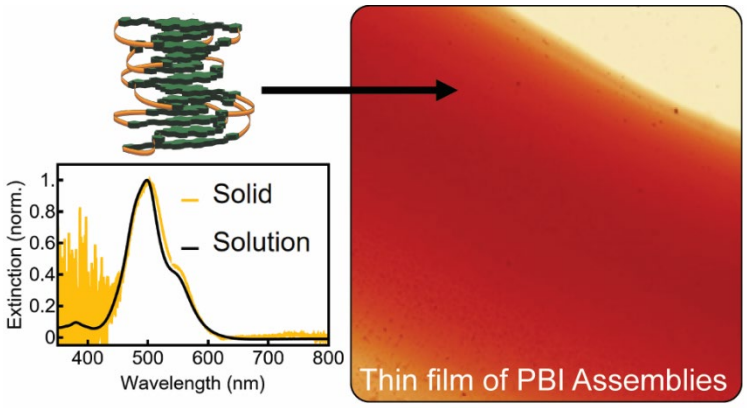

Structural and functional heterogeneity is a consequence of the weak noncovalent interactions that direct formation of organic materials from solution precursors. While covalent tethering of solution-phase assemblies provides a compelling strategy to enhance intermolecular order, the solid-state photophysical impacts of this tethering strategy remain unestablished. This work uses pump probe microscopy to compare excited state dynamics in thin films fabricated from tethered perylene bisimide assemblies to those from noncovalent assemblies. On average, tethered films exhibit faster and more homogeneous excited state lifetimes, consistent with stronger and more uniform intermolecular coupling. Optical measurements of excited state diffusion show that the tethered film has ~75% faster transport than the control film. Kinetic Monte Carlo modeling suggests that reduction of site energetic disorder is sufficient to quantitatively explain the difference in diffusion coefficients. These results provide strong support that covalent tethering is a promising strategy to enhance the structural and energetic ordering in molecular materials.

Manuscript

Introduction

The diverse application portfolio of organic semiconductors in photovoltaics,[176] chemosensors,[108] flexible electronics,[177] and light-emitting diodes[178] is in part enabled by their sensitive structure-function relationship, which provides a means to tune functionality via synthetic modification. However, this same structure-function sensitivity can be problematic in molecular materials, as minor variation in short- and long-range structural order can cause significant differences in functional properties at nano to mesoscale dimensions.[3] Because solid-state organic materials typically rely on noncovalent interactions to enforce intermolecular ordering, minor perturbations to, for example, solvent dielectric[179], temperature[180], and molecular concentration[181] will inherently change the structure and defect density of the bulk material. These minor changes to the crystal structure can cause significant differences in electrical and optical properties,[6, 182-186] thus making semiconducting materials derived from organic building blocks prone to unpredictable functionality.

Materials derived from the family of perylene-3,4,9,10-tetracarboxylic bisimide (perylene bisimide, PBI) are promising organic semiconductors as they exhibit strong chemical, thermal, and photo stability,[182, 187] as well as high electron mobility and fluorescence quantum yields.[188, 189] Self-assembly of the perylene core can produce structurally well-defined nanoscale objects.[190-193] If robustly translated to the solid-state, such bottom up design strategies could be lever-aged to, for example, engineer materials with non-equilibrium structures aimed at specific functionalities.[193, 194] Despite the promise, a robust and predictable approach for translating the well-defined structure of solvated self-assembled pre-cursors into a solid-state material remains challenging.[195]

One strategy to overcome this challenge is to reinforce the weak noncovalent interactions of solution-phase assemblies so that their structure is resistant to perturbation. Recently, Olivier and coworkers have developed a covalent tethering/stapling approach, whereby self-assembled supramolecular assemblies of perylene bisimide chromophores are covalently tethered to rigidify the π-stacked structures.[196, 197] Compared to conventional molecular assemblies that are bound only by van der Waals interactions, the structures of the covalently-tethered assemblies are significantly more resistant to changes in temperature and dielectric environment in the solution-phase. As a result, the electronic coupling between adjacent units is less sensitive to the local environment.[196]

While this previous work demonstrates the validity of the covalent tethering strategy to enhance interchromophoric coupling in solvated assemblies, there is to date, no work that addresses how the functionality of tethered assemblies, engineered in solution, translates from the solution-phase to a solid-state material. Based on the structural robustness exhibited by the solution-phase tethered assemblies, we hypothesized that the electronic structure determined by the solution-phase self-assembly process would be maintained upon condensation into the solid-state. We further anticipated that materials formed from a suspension of the tethered assemblies would be characterized by greater long-range electronic ordering relative to materials formed from noncovalent assemblies, and, therefore, exhibit 1) more homogeneous excited state behavior, and 2) faster exciton diffusion.

To test these hypotheses, we used ultrafast pump probe microscopy (PPM) to compare excited state dynamics in a film cast from PBI noncovalent assemblies to a film comprised of covalently-tethered PBI assemblies PBI-Stap-2 Because PPM provides the ability to measure ultrafast spatiotemporal dynamics with spatial resolution better than 1 μm, it is possible to compare

excited state decay kinetics from different locations on the same film. We find that excited state decay lifetimes are faster and significantly more uniform in the thin films formed from tethered assemblies, relative to decay kinetics collected on the untethered film. We also use PPM to directly measure exciton diffusion in the two films and find that excited state transport in the tethered-assembly film is significantly faster than in the untethered film. Kinetic Monte Carlo (kMC) modeling of exciton transport suggests that reduction of energetic disorder is sufficient to explain the approximate two-fold increase in exciton diffusion observed. Together, these results provide strong support that covalent tethering enforces the structure and electronic coupling of solution-phase supramolecular assemblies, and therefore provides a promising approach for achieving optimized solid-state organic materials for future electronic and optoelectronic needs.

Synthesis and Characterization

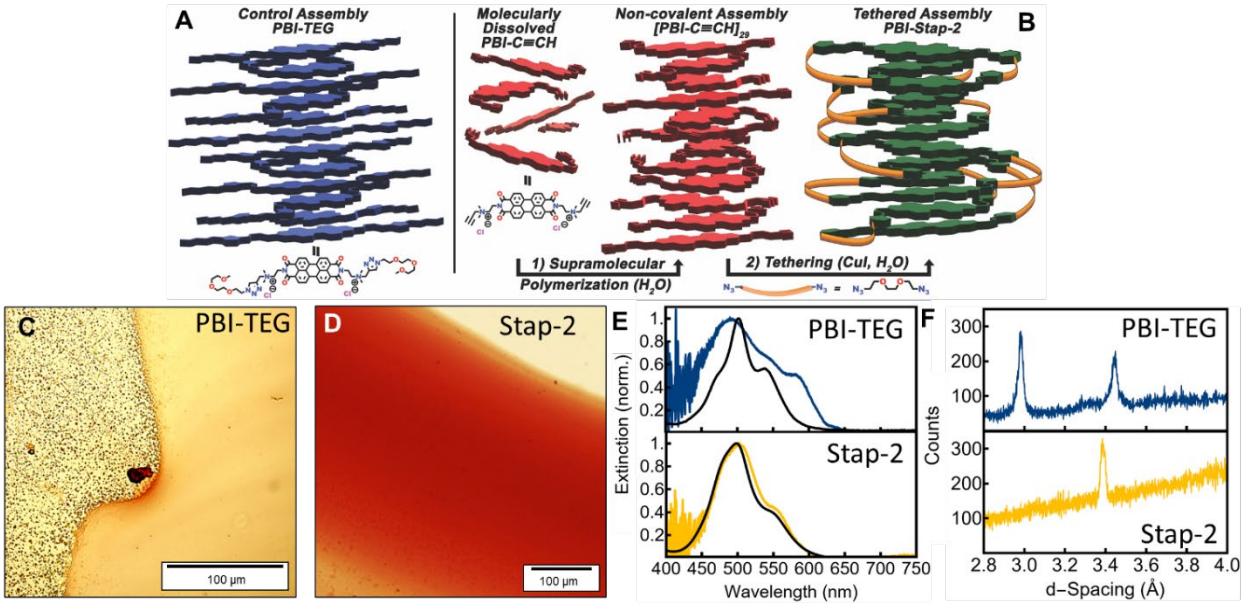

Figure 5.1: Summary of precursors and thin films. A) Schematic of the control precursor PBI-TEG B) Synthetic scheme to generate tethered superstructures (PBI-Stap-2) by aggregation followed by covalent tethering. C) and D) bright-field microscope images of the PBI-TEG and PBI-Stap-2 films, respectively. E) Comparison of absorption spectra for the precursor solutions (black) and the deposited thin films (yellow/blue) for the two systems. F) Comparison of the XRD patterns from films prepared from the PBI-TEG and PBI-Stap-2 precursors.

Figure 5.1 summarizes the composition of the two PBI systems compared in this letter. Panels A and B show schematic representations of the solution-phase control (PBI-TEG, PBI-triethylene glycol) and tethered assemblies (PBI-Stap-2) used as precursors for the two films. PBI-Stap-2 features ethylene oxide linkers that tether the PBI core with triazole functionality. The short molecular tether has been shown to create tethered structures whose excitonic coupling remain virtually unperturbed in solution as a function of solvent temperature and dielectric constant.[196] The control PBI-TEG is functionalized with analogous ethylene oxide terminal groups. The synthesis and characterization of both precursors have been reported previously.[196, 197] Briefly,

tethered assemblies are synthesized from the reaction of the parent supramolecular polymer with the linker precursor N3(CH2CH2O)2N3 in water. Due to the polymeric character of these assemblies, gel permeation chromatography is used to remove unreacted species and narrow the size distribution of the PBI-Stap-2 assemblies.

To prepare films of the PBI-TEG (Fig. 5.1C) and PBI-Stap-2 (Fig. 5.1D), aqueous solutions were prepared and drop-cased onto borosilicate slides. It is important to highlight that careful control of environmental parameters and advanced fabrication techniques like printing or meniscus-guided coating can provide a significant handle for controlling the structure of solution-processed organic thin films.[198, 199] Here, we aim to demonstrate that despite using a fabrication approach that provides minimal control over the environmental variables, films with highly uniform electronic structure can be formed if morphology is enforced at an appropriate length scale.

Visible absorption spectra of the control and tethered assembly films were collected with a homebuilt microscopic spectrometer. The spectrum of the PBI-TEG film (Fig. 5.1E-Blue) is characterized by three overlapping transitions at 495, 545, and 585 nm. Based on comparison to the absorption spectrum of the assembly precursor solution (solid black), the transitions at 502 and 538 nm are assigned to the 0-1 and 0-0 vibronic transitions.[196] The distinct shoulder at 585 nm is unique to solid-state films of PBI-TEG, and likely derives from low-energy states formed as a result of structural disorder introduced during film condensation. While a bathochromic shift could indicate formation of local J-type or HJ-type aggregation[111, 112, 139], fluorescence spectroscopy and microscopy performed on the PBI-TEG film showed no detectable emission, which would be expected in the case of J-type coupling. In contrast to the control film, the tethered PBI-Stap-2 film

exhibits a ground state absorption spectrum (Fig. 5.1E-gold) nearly identical to that of the solution-phase assemblies (black), indicating that the electronic structure is preserved upon formation of the solid-state film.

To characterize the structure of the films, we next turned to grazing incidence x-ray diffraction (Fig. 5.1F). The XRD pattern from the PBI-TEG film reveals two distinct peaks at $2\theta = 25.85°$ (3.45 Å) and $2\theta = 29.90°$ (2.98 Å). We assign the 3.45 Å peak to the π-π stacking distance, but the assignment of the peak at 2.98 Å is less certain. It is unlikely to arise from a polymorph with a closer packing as it falls outside the range of 3.4 Å to 3.6 Å observed for the π-π stacking distance in PBI materials.[200-203] Instead we assign it to a diffraction plane that is non-coplanar with the PBI core, reflecting long-range symmetry in crystal directions orthogonal to the π-π stacking direction.[204] For the PBI-Stap-2 film, we observe only a single diffraction peak at $2\theta = 26.30°$ (3.39 Å), which is expected for a film comprised of columnar π-stacked assemblies. The smaller spacing associated with this peak indicates that covalent tethering enforces a more tightly packed π–π stack than the PBI-TEG film. The peak from the PBI-Stap-2 film is also narrower than the corresponding peak in the PBI-TEG film, particularly near the base, indicating that PBI-Stap-2 film is structurally more homogeneous along the π-stacking direction. Note that in the PBI-TEG film there is a weak feature near 3.3 Å that may indicate a small population of the closer packing arrangement seen in the Stap-2 film, however, this feature is broad and poorly resolved.

Ultrafast

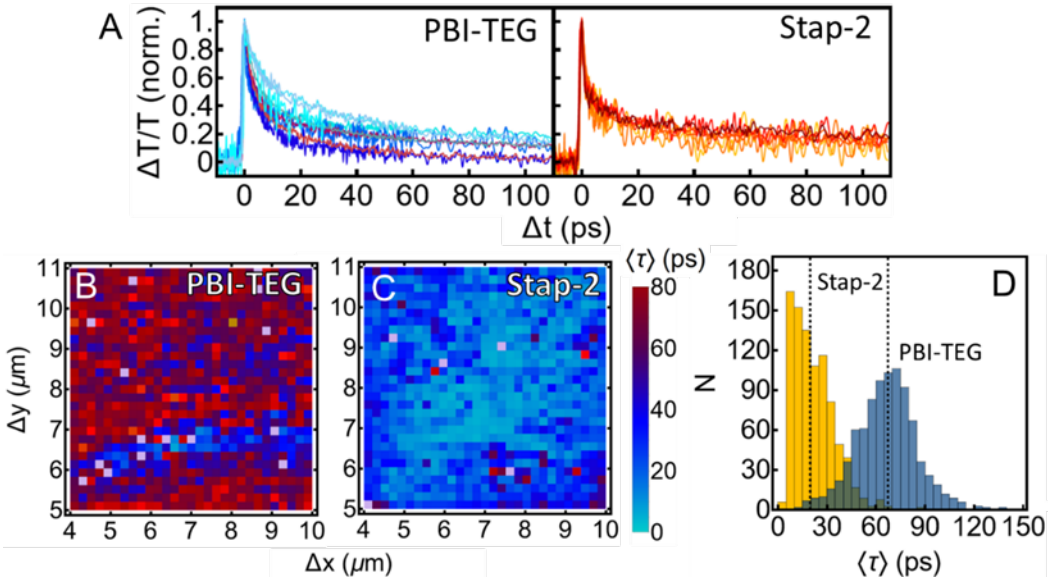

Figure 5.2: Excited state lifetimes of the two thin films. (A) Kinetics of the PBI-TEG and PBI-Stap-2 films measured at different locations on each film. Excited state average lifetime images of the control PBI-TEG film (B) and the PBI-Stap-2 film (C). (D) Distribution of average lifetimes from each of the lifetime images in panels B and C. The dashed lines show the mean lifetimes of 68.4 and 23.8 ps for the control PBI-TEG and PBI-Stap-2 films, respectively.

The closer interchromophore distance observed in XRD suggests that the electronic coupling should be altered in the PBI-Stap-2 film. To compare the ultrafast dynamics of the two films and evaluate the impact of covalent tethering, we utilized ultrafast pump probe microscopy (PPM), which provides the ability to measure ultrafast dynamics with sub-micron spatial resolution and directly image exciton transport.[139, 205-207] Both films were excited at 500 nm, near the peak of the 0-1 vibronic transition (Fig. 5.1E) with an excitation fluence limited to 130 μJ/cm^2 to eliminate nonlinear recombination processes contributing to the kinetics.[208] The probe wavelength of 800 nm monitors a broad photoinduced absorption, which has previously been assigned to a mixed Frenkel exciton, charge-transfer state in the solution-phase assemblies.[196] Broadband transient

absorption spectra of the thin films (Supporting Information, SI) are consistent with this spectral assignment and show that the PBI-Stap-2 excited state exhibits greater charge transfer character than the PBI-TEG film.

Because pump probe microscopy has sub-micron spatial resolution, it provides the opportunity to characterize the excited state lifetime in a manner inaccessible to conventional time-resolved spectroscopies. By measuring decay kinetics at several locations on each film, we find that excited state dynamics in different locations of PBI-TEG are significantly more heterogeneous than those of the PBI-Stap-2 (Fig. 5.2A). We observed similar behavior across two additional films of both PBI-TEG and PBI-Stap-2 prepared on different days, indicating that the differences in excited state lifetime behavior are systematic to the precursor materials and fabrication approach employed. To visualize this difference in behavior, we collected pump probe images over a 6×6 μm region of each film for a series of increasing time delays. We fit the resultant kinetics from each spatial pixel of the image stack to a biexponential model to extract an average lifetime for that location on the films. Figures 5.2B and 5.2C show average excited state lifetime ($\langle\tau\rangle = (a_1\tau_1 + a_2\tau_2)/(a_1 + a_2)$) images for PBI-TEG and PBI-Stap-2 films, respectively. When the images are compared (scaling is identical), the PBI-TEG film shows significantly longer-lived and more widely distributed excited state lifetimes relative to the film of the locked PBI-Stap-2 assemblies.

Histograms of the 900 locations probed in the lifetime images are shown in Fig. 5.2D. From these distributions, two material differences are apparent. First, the average lifetime of the control PBI-TEG film is 69 ps, whereas the PBI-Stap-2 film has a significantly shorter average lifetime of 23 ps. Second, the distribution of lifetimes shows more variation in the control film than the PBI-

Stap-2 film. ($\sigma_{TEG} = 29\ ps$; $\sigma_{Stap-2} = 16\ ps$). While it is difficult to assign a specific mechanism with single wavelength measurements, the rapid excited state relaxation observed in the PBI-Stap-2 film is characteristic of strong intermolecular coupling,[209-212] which activates fast excited state relaxation pathways through charge transfer state mixing,[213-215] strong dipole-dipole coupling,[216] and/or internal conversion.[56] The narrower lifetime distribution observed for the PBI-Stap-2 tethered film further suggests that intermolecular coupling is more homogeneous than in the control PBI-TEG film. Although there are sites on the control film that exhibit a similar lifetime as the PBI-Stap-2 film, there are many more sites with longer lifetimes, which likely derive from a combination (depending on the local morphology) of states with weaker intermolecular coupling and from energetically low-lying trap states.

Without high resolution broadband[194, 208] or multi-dimensional time-resolved microscopies[184], it is difficult to assign which specific mechanisms, for example Frenkel-CT exciton mixing[147, 148], excimer stabilization[149], and/or geometric rearrangement/self-trapping[150], are responsible for the longer lifetimes observed in the control film. However, since the films are chemically homogeneous, the variability in lifetime observed from site to site in the PBI-TEG film must reflect morphological defects and differences in intermolecular coupling. Regardless of their nature, the heterogeneity observed clearly highlights one of the primary challenges of characterizing and ultimately utilizing organic materials – the functional properties are highly sensitive to microscopic morphology changes that are an intrinsic characteristic of film fabrication. Our results indicate that covalent tethering is a promising strategy for mitigating such heterogeneity and achieving films with significantly improved electronic homogeneity, even under minimally controlled fabrication conditions.

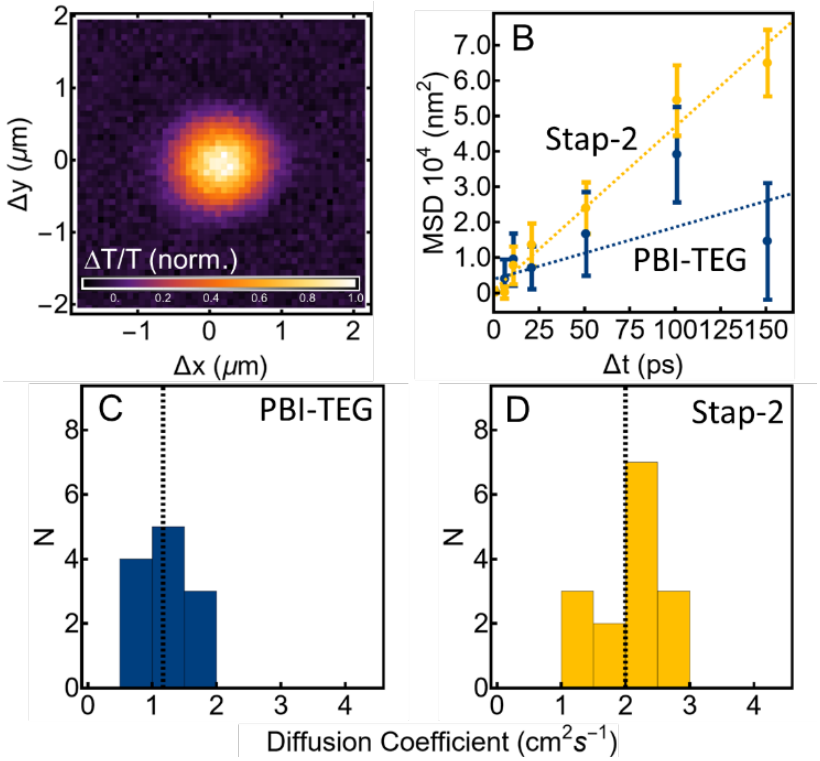

Figure 5.3: Comparison of excited state transport. A) Diffusion spot measured on the PBI-Stap-2 film at Δt = 0 ps. C) Representative mean squared deviation data collected for PBI-TEG (Blue, 0.83 ± 0.29 cm^2s^{-1}) and PBI-Stap-2 (Yellow, 2.06 ± 0.17 cm^2s^{-1}). Distributions of measured diffusion coefficients for PBI-Control (C) and PBI-Stap-2 (D) with average values (indicated by dashed lines) of 1.12 ± 0.38 cm^2s^{-1} and 1.94 ± 0.48 cm^2s^{-1}, respectively.

To determine the effects of covalent tethering on excited state transport, we next turned to spatially offset pump probe microscopy. For these measurements, the probe beam is positioned at a fixed location and the pump beam is scanned over the probe to generate an image of the excited state spatial distribution (Fig. 5.3A) as a function of the delay time, Δt. By collecting a series of images at increasing Δt between 0 and 150 ps, excited state transport can be measured with precision that is limited only by signal-to-noise levels.[158] The averaged 1D images are fit by numerical convolution of the diffusion kernel with the initial (Δt = 0 ps) spatial profile to determine

the mean squared deviation (MSD) of the excited state profile.[159] Linear fits to the MSD provide a measure of the diffusion coefficient (Fig. 5.3B).

Figure 5.3C, D shows diffusion coefficients measured in twelve locations on the control PBI-TEG film and 15 locations on the PBI-Stap-2 tethered film. On average, the diffusion coefficient of the control film is measured to be 1.12 ± 0.38 cm^2s^{-1}. The PBI-Stap-2 film exhibits nearly 75% faster transport, with an average diffusion coefficient of 1.94 ± 0.48 cm $2s^{-1}$. These average values are similar to diffusion coefficients measured in comparable, well-ordered organic materials[217] but slower than observed in vapor-deposited PBI films on the 0 – 3 ps timescale, which have been reported to exceed 40 cm^2s^{-1}. [218] For both films, we observe significant variability in observed transport rates. Although measurement noise is likely responsible for some of the observed variation, microscale morphology differences are also likely contributors to the width of the distribution for both films. For the control film, the presence of well-resolved peaks in the X-ray diffraction pattern indicates that well-ordered domains are present but overall that the film is less ordered than PBI-Stap-2. The lifetime imaging data presented in Fig. 5.2 is another indicator of microscale morphological heterogeneity. For the PBI-Stap-2 film, lifetime imaging suggests that, at least from the perspective of excited state relaxation, the film is more homogeneous than the control film. These results are consistent with a narrowed density of states, suggesting that relative to the control film, the PBI-Stap-2 film is likely to have a reduced density of localized trap sites that inhibit transport. Instead, we attribute the site-to-site variation in measured diffusion coefficient to variability in inter-assembly coupling due to differences in the geometrical alignment of adjacent assemblies.

Kinetic Monte Carlo

Despite the site-to-site variability observed for both films, the difference in transport rates is significant at the 0.01 confidence level ($P < 0.005$ using the Mann-Whitney test), suggesting that covalent tethering improves exciton transport, likely by narrowing the density of states and reducing trapping. To provide further insight into this hypothesis, we use a kinetic Monte Carlo (kMC) approach to model transport in the films, where the probability of inter-site hopping is parameterized using a Miller-Abrahams model (further detail available in supporting information).[219] We generate a 3D cubic grid, with each site assigned an energy based on a Gaussian distribution of variable energetic width. Exciton trajectories are propagated and mean square displacements are used to calculate average diffusion constants (SI).

We first parameterize the model to reproduce the experimentally observed diffusion coefficient for PBI-TEG of ~1.1 cm^2s^{-1}. Then, to model the Stap-2 film, all parameters are kept identical, except for the width of the energetic distribution. We find that by reducing the width from ~75 meV for PBI-TEG to ~50 meV for PBI-Stap-2, the model quantitatively reproduces the experimentally observed diffusion coefficient of ~1.9 cm^2s^{-1} in PBI-Stap-2 (SI). Given the likely importance of both coherent and incoherent transport mechanisms,[218, 220] as well as the potential role played by polarons[221] and charge transfer states[222], the simple kMC model described above is unlikely to capture the full mechanistic complexity of transport in these materials. Nevertheless, because the two films are nearly chemically identical, using the model as a comparative tool provides insight into the role played by energetic disorder on transport.

Conclusion

In summary, a direct spectroscopic comparison between thin film formed from noncovalent assemblies and from covalently tethered molecular assemblies indicates that interchromophore coupling is enhanced in the covalently tethered film. By using pump probe microscopy, we provide direct evidence of functional properties that are strongly impacted by this additional ordering: a 73% increase in excited state transport compared to the control film, as well as a shorter and more homogenous excited state lifetime. KMC modeling suggests that narrowing the distribution of site energies, presumably by enhancing structural homogeneity, is an important factor responsible for the observed increase in the transport rate. These results suggest that covalently locking noncovalent assemblies is a promising strategy for reducing structural and energetic heterogeneity in organic functional materials. Combining covalent tethering with well-established solution-based fabrication approaches may be a compelling strategy for designing hierarchical structures into solid-state organic materials.

CHAPTER SIX

CONCLUSION

Chapters three through five show the impact of generating more ordered systems using solution-phase processing techniques from levels one to three. Chapter three covers materials that rely on self-assembly (level 1) and chapter four introduces a more ordered system via solution-phase aggregation (level 2). Finally, chapter five covers molecular stapling of aggregates (level 3). In these latter two chapters, materials prepared with processing levels 2 and 3 are compared back to processing level 1 (materials derived without solution-phase processing).

In chapter three, we performed solid-state deposition of the 3-styryl-BODIPY monomer which resulted in long ribbon-like crystals. Emission and extinction microscopies reveal the strong J-type electronic coupling via evidence of the emission in the solid-state at 660 nm as well as a spectral redshift from 583 nm to 614 nm. The collection of ultrafast experiments shows a complex energy landscape of the BODIPY ribbons; the emission, excited state absorption (two color and broadband), and ground state bleach lead to very different relaxations. From the ground state absorption and ultrafast spectra/relaxation lifetimes, we were able to construct a simplified energy level diagram that depicts the main transitions. When excited/pumped at 580 nm the emission and two color lifetimes result in similar relaxation rates to each other, however when pumped at 517 nm, the excited state lifetimes are very different from the lower energy excitation. One would expect that the excited state absorption in broadband and two color experiments would result in similar lifetimes, but we observed that when pumped at 517 nm, the average lifetime is double that when pumped at 580 nm. This suggests that when pumping at 580 nm, we are pumping closer to the "J-state"[161] and that this state is more coupled with the ground state versus the S_1 state, allowing

for faster relaxation. The ground state bleach decays rapidly compared to the excited state absorption from both excitations. While the exact mechanism behind rapid ground state bleach decay is elusive, the combination of localization and fast transport provides a reasonable explanation for this observation (fig. 3.5C).

In chapter four, we have mitigated electronic and structural heterogeneity in the solid-state by pre-aggregating the porphyrin monomers via antisolvent aggregation. Aggregation of the PZn monomer was confirmed by the spectral shifts in the solution-phase and a notable hypsochromic shift from 469 nm to 458 nm. The solid-state extinction showed that there is significant broadening of the 469 nm peak, but no further peak shift. Turning to ultrafast studies, we have also shown that the lifetime of the excited is highly correlated with the degree of structural order. The monomer exhibits the longest lifetime with an average lifetime of 1.26 ns, the aggregate is much shorter with a lifetime of 349 ps, and the films show substantially faster relaxation with the film fabricated from the monomer having a 72.56 ps average lifetime and the film composed of the aggregate having a 26 ps average lifetime. These results show that the lifetime decreases as the order and electronic coupling of the system increases, resulting in lifetime differences spanning two orders of magnitude. The pre-aggregated films exhibit isotropic dichroism whereas the films prepared from just the monomers are highly anisotropic. Solution-phase processing via aggregation prior to solid-state deposition provides a compelling strategy for increasing structural homogeneity in the solid-state.

In chapter five we studied the third level of order with the covalently bound aggregates of PBI. We used a direct spectroscopic comparison between thin films formed from noncovalent assemblies and from covalently tethered molecular assemblies and showed that interchromophore

coupling is enhanced in the covalently tethered film. By using pump probe microscopy, we provide direct evidence of functional properties that are strongly impacted by this additional ordering: a 73% increase in excited state transport compared to the control film, as well as a shorter and more homogenous excited state lifetime. KMC modeling suggests that narrowing the distribution of site energies, presumably by enhancing structural homogeneity, is an important factor responsible for the observed increase in the transport rate. These results suggest that covalently locking noncovalent assemblies is a promising strategy for reducing structural and energetic heterogeneity in organic functional materials. Combining covalent tethering with well-established solution-based fabrication approaches may be a compelling approach for designing hierarchical structures into solid-state organic materials.

Of the three levels of solution-phase processing before solid-state deposition, covalently tethering provides the most successful strategy to generate a functioning organic semiconductor. These molecules are far superior because they are highly thermally stable, electronically stable, and photostable.[196] Properties of the chromophore are retained after several years of storage whereas the molecules in chapters three and four decompose in a short amount of time and require significant sample preparation to be able to study these systems using ultrafast lasers. The covalent linkers might also function as an environmental insulator, thus making the chromophores photochemically inert, which is an ideal property for exciton transport. The biggest drawback when considering strongly coupled organic semiconductors is the short lifetime that persists in both H- and J-type aggregates. Should one consider using these as transport devices, great attention must be given to the lifetime of the excited state.

APPENDICES

APPENDIX A

SUPPORTING INFORMATION FOR "ULTRAFAST EXCITONIC TRANSPORT AND STRONG ELECTRONIC COUPLING IN SELF-ASSEMBLED ALPHA-STYRYL-BODIPY NANORIBBONS"

Experimental Details

Below are the experimental details used in chapter 3.

Synthesis

Synthesis of the BODIPY molecule is unavailable at this time due to the sensitive nature of the novel synthetic route for this molecule.

Confocal Emission

Confocal emission microscopy was conducted on a Leica STELLARIS 8 inverted confocal microscope platform. The instrument's white light laser was filtered to excite the BODIPY sample at wavelengths of 405, 450, 500, 550, 579, 600, 625, 650, 675, and 700 nm. Using a combination of filter cubes, emission was detected at +10 nm from the excitation source and integrated for long wavelengths with a HyD detector. Pixel format was set to 1024x1024. For Figure A3 photographs of emission signal from each excitation wavelength were taken in Leica's LASX software and exported in TIF format for (A) and in ASCII format (B).

Pump Probe Microscope – Two color

Pump probe microscopy experiments were performed using a Spectra Physics MaiTai (~80 fs pulse width, 80 MHz repetition rate, 800 nm fundamental). The fundamental beam is split into the pump and probe lines using a plate beamsplitter. The pump line is passed through an acoustic optic modulator (AOM) to reduce the repetition rate of the pulse train to 2 MHz and modulate with a 50% duty cycle at 120 kHz. The modulated pump is focused through a photonic crystal fiber (PCF) to generate a white light supercontinuum which is passed through a 580 (+/- 5 nm) nm band pass filter to select the pump wavelength. The spectrally filtered pump is coupled to an optical

delay stage to achieve a temporal delay from that of the probe line. The pump line is coupled, via a pair of galvanometer (GV) mirrors, through a 4-f telescope and combined with the probe with a dichroic beamsplitter. The probe line is first modulated to 2 MHz via an AOM to match the repetition rate of the pump. The combined beams are sent onto a set of GV mirrors, through a 4-f telescope, and coupled into the back aperture of a 100x plan apo objective to focus onto the sample. The two beams are collected with a condenser and the pump beam filtered out using a long pass filter. The probe is focused onto an amplified silicon photodiode. The APD signal is split (Mini Circuits ZFRSC-2050+) and one output it sent to a Stanford Research lock-in amplifier to demodulate the signal at 120 kHz (ΔT). The other is coupled to a National Instruments DAQ card for the reference (T).

Figure A7 Plot legend correspond to the power of the pump beam. At 2 MHz on a 50% duty cycle and a spot size of 612 nm at 1/e2 the powers of 0.1, 0.2, 0.3, 0.4, 0.5, 0.6, 0.7 μW corresponds to 67.82, 135.6, 203.5, 271.3, 339.1, 406.9, 474.7 μJ cm^{-2}, respectively. Even at the upper limit of a high fluence 474.7 μJcm-2, there is no indication of any non-linear recombination processes (fig. A7). However, due to the time scale of the experiments, prolonged exposure on the films at fluences greater than 203.5 μJcm-2 results in visual decomposition of the wires. Excited state transport was determined to be isotropic and so spatially offset scans were performed along a single axis to allow for more averaging. Each time delayed frame is the average of twenty spatially separated scans along a single axis, for pump probe delays between $\Delta t = 0$ and 140 ps to calculate the diffusion (fig. A10). As noted in the main text, diffusion calculations were only fit within the first 10 ps.

Pump Probe Microscope – Broadband

The Broadband pump probe microscope is powered by a Coherent Monaco industrial femtosecond laser (40 W, 1035 nm, 1 MHz, 300fs pulse width). The beam is split by a 30:70 (R:T) beamsplitter; the reflected pump beam sent through an acoustic optic modulator (AOM) running at 15.6kHz with a 50:50 duty cycle. The pump beam is focused into a type 1 BBO to generate the second harmonic (517.5 nm). The pump is then sent onto a translation stage with a range corresponding to ~2 ns of pump probe delay. The pump line is coupled, via a pair of galvanometer (GV) mirrors, through a 4-f telescope and combined with the probe with a 70:30 beam splitter and sent into the back aperture of a 100X Olympus MPlanFL-N and focused on sample. The light transmitted by the initial 30:70 beamsplitter is used to produce the probe, The probe (~1μJ) is focused with a 75mm focal length into a Yittrium Aluminum Garnet (YAG) crystal to generate the white light continuum, and then collimated with an achromatic lens before being combine with the pump. After the sample a second objective (100x Nikon TU Plan Apo) collimates the beams, the pump beam is filtered out with a long pass filter. The probe is sent into a custom-built spectrometer that consists of two 50 mm (1.8F) camera lenses and a 600 gratings/mm holographic grating. The dispersed probe is focused onto a line CMOS camera (Teledyne DALSA OctoPlus E2V line CMOS camera, 2048 pixels). Spatial resolution of the sample is obtained with 0.2 nm positional precision using a piezoelectric stage (Mad City Labs, Nano-H100). The camera interfaces with a computer and dumps frames of collected line data where data acquisition and control are provided by a homebuilt LabVIEW guided user interface (GUI). Collecting two lines with the pump on and two with the pump off averages the noise of the two ADCs and allows for the calculation of $\Delta T/T$. The LabVIEW GUI allows for the consolidated control of transient transmission experiments.

XRD

X-ray diffraction was measured using a Bruker D8 Advance Power X-ray Diffractometer with a Cu X-ray source in Grazing Incidence Diffraction geometry. The source was held constant at 1.600 degrees while the detector angle was varied.

Supporting Data

Below are the supporting data used in chapter 3.

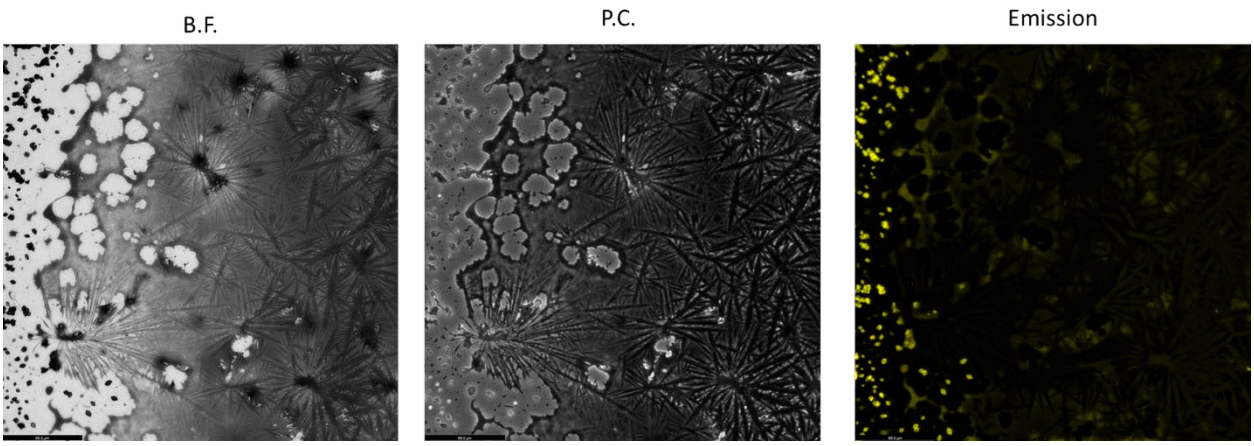

Figure A1: Microscope images taken of the BODIPY thick film used in the XRD experiments. The three insets correspond to the bright-field image (left), phase contrast (middle) and the right inset corresponds to a false colored emission image.

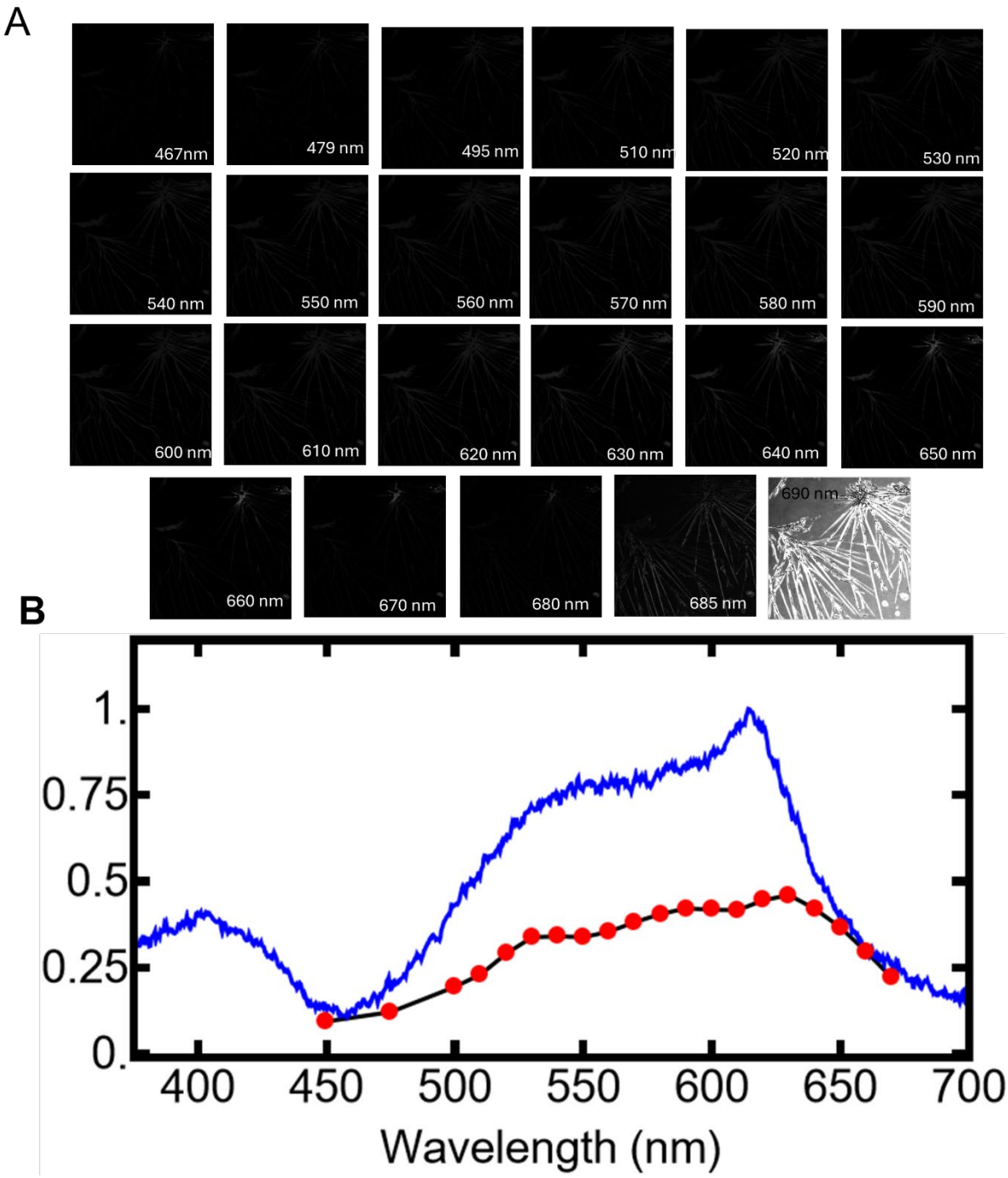

Figure A2: A) Confocal Emission Images displayed as a function of excitation (inset). B) Integrated emission intensity of images in (A) normalized to the highest signal at 690 nm, note 680+ nm are not shown in the B due to the transmission of light with the optical filter. Extinction spectrum of a single ribbon (blue) plotted with the integrated emission (red).

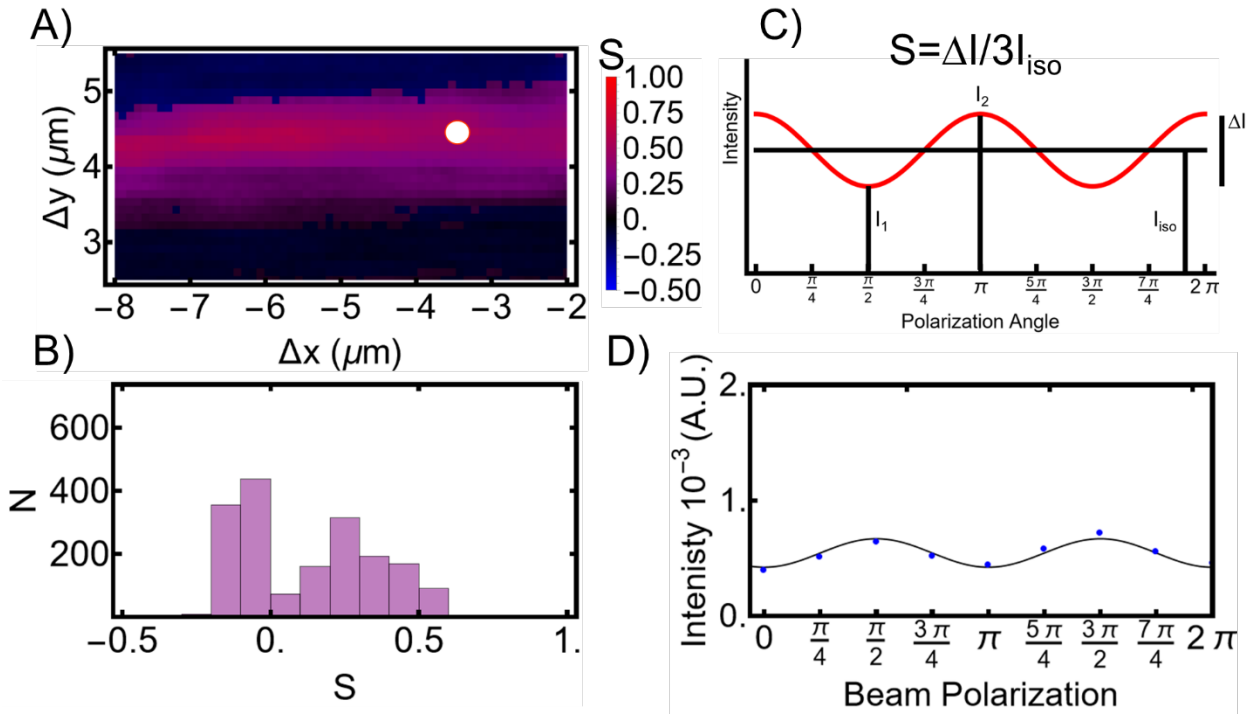

Figure A3: A) Image of the spatially resolved linear dichroism calculated per pixel. B) Histogram of (A). C) Definition of the orientation parameter replicated from Gábor et. al. [142] D) Single location of the intensity plotted against the polarization of the beam, showing the maximum absorption is in the direction of the wire.

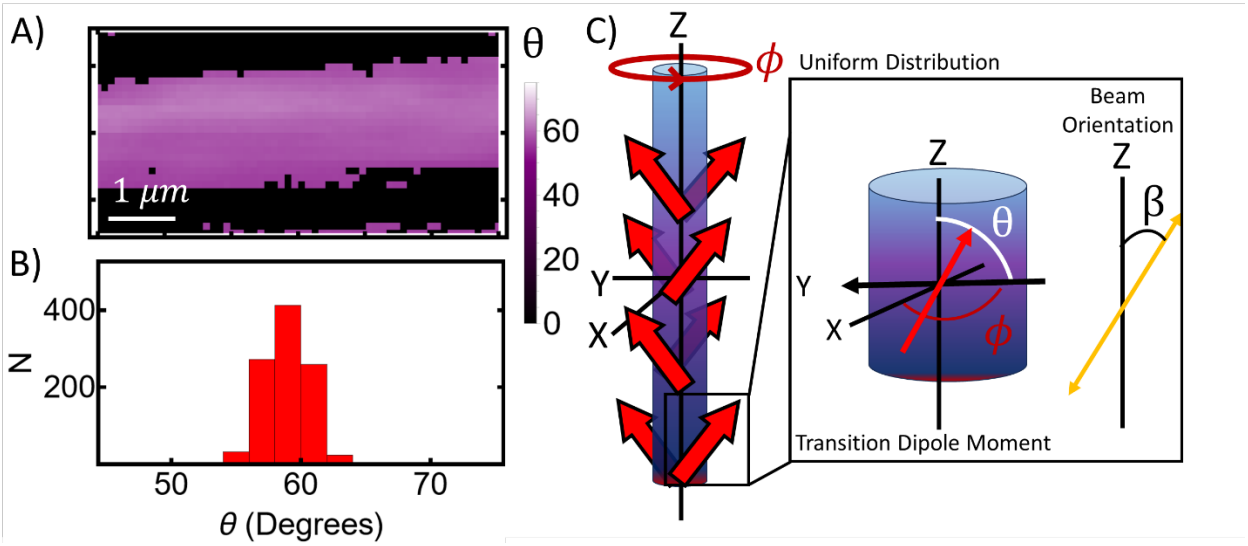

Figure A4: Transition dipole orientation angles calculated from A4 and the corresponding histogram (B). Panel C) is a replication of the dipole projection model replicated from Harada et. al.[144]

The model used to calculate the transition dipole orientation was replicated from Harada et al. [144] This model assumes that the transition dipole moment (μ) and orientation of the transition dipole (θ) is not correlated to the z axis and that all transition dipole moments are uniformly distributed along z-axis with an angle ϕ. The growth of the ribbon corresponds to the z-axis and the beam polarization relative to the ribbon is angle β. Note that the data is normalized to the angle in which the material is most transmissive, β'. Thus, the transmission intensity can be fit the following equation:

$$I(\beta) = \frac{\int_0^{2\pi}(sin\beta sin\theta cos\phi + cos\beta cos\theta)^2 d\phi}{\int_0^{2\pi}(sin\beta' sin\theta cos\phi + cos\beta' cos\theta)^2 d\phi} = \frac{3 + cos2\theta + cos2\beta(1 + 3cos2\theta)}{3 + cos2\theta + cos2\beta'(1 + 3cos2\theta)}$$

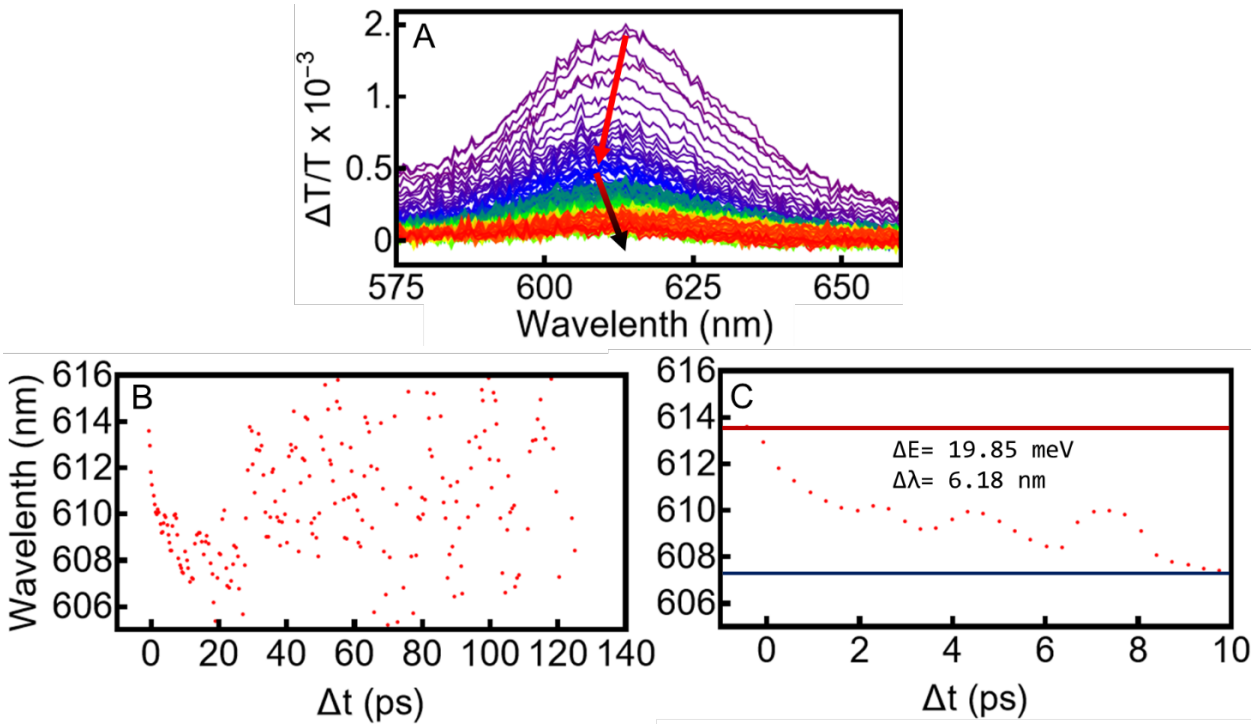

Figure A5: Transient absorption spectra collected on a single nanoribbon. Panel A highlights a slight blue shift in the ground state bleach. Panels B and C show the center of the peak (determined with a Gaussian fit) as a function of time.

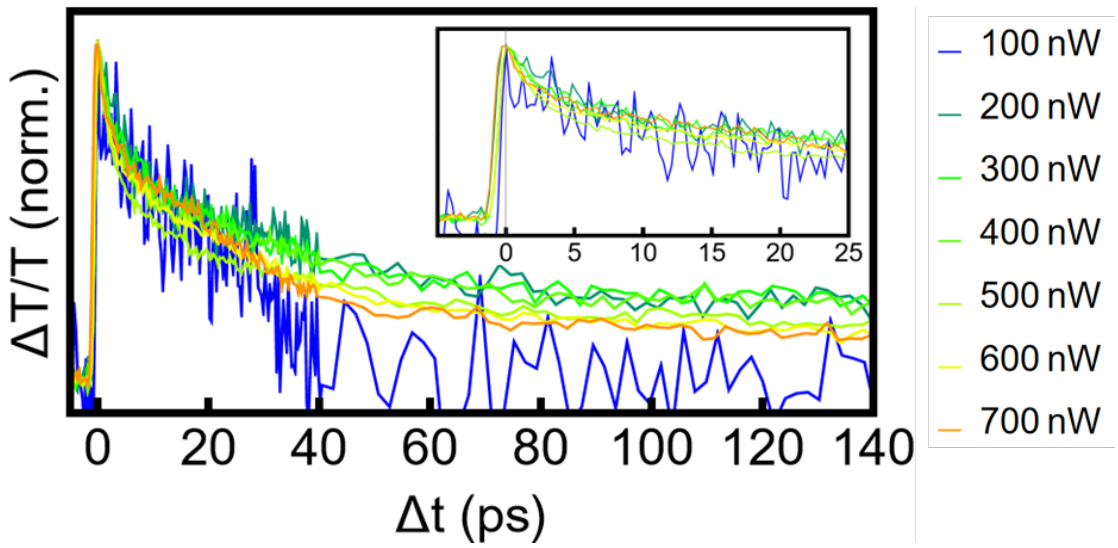

Figure A6: Pump probe power dependent kinetics taken at the powers displayed on the right. Inset shows kinetics at early times.

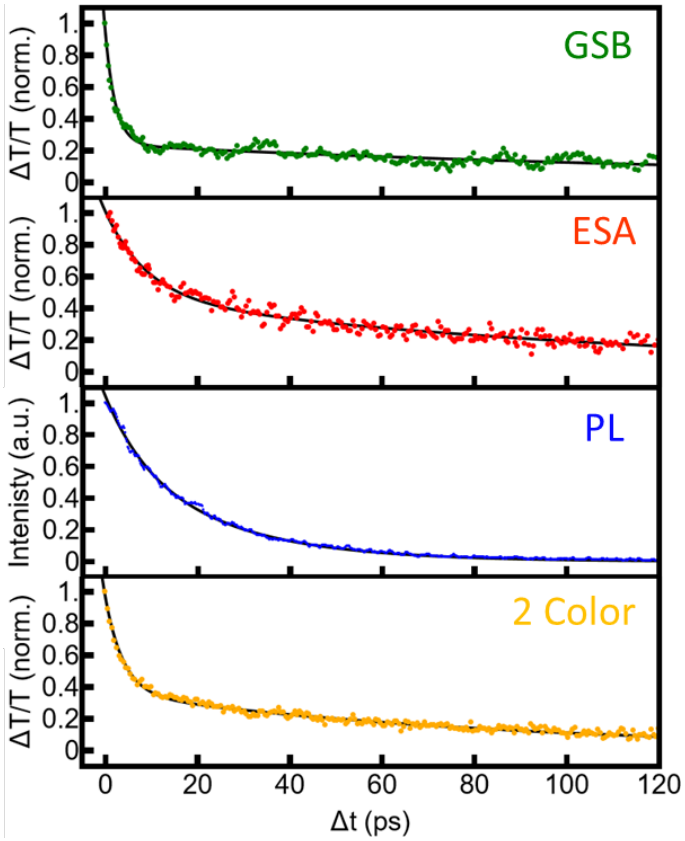

Figure A7: Compiled kinetic decay traces from broadband pump probe, two color pump probe, and streak camera emission.

Table A1: Lifetime fitting parameters for the time resolved emission and transient absorption experiments.

	GSB	**ESA**	**emission**	**Two color**
a_1	0.955	0.541	0.710	0.603
a_2	0.212	0.468	0.334	0.363
$\tau_{1\ (ps)}$	2.110	9.055	13.305	3.83
$\tau_{2\ (ps)}$	89.147	113.242	36.291	84.26
$\langle\tau\rangle_{\ (ps)}$	17.94	57.38	20.65	34.06

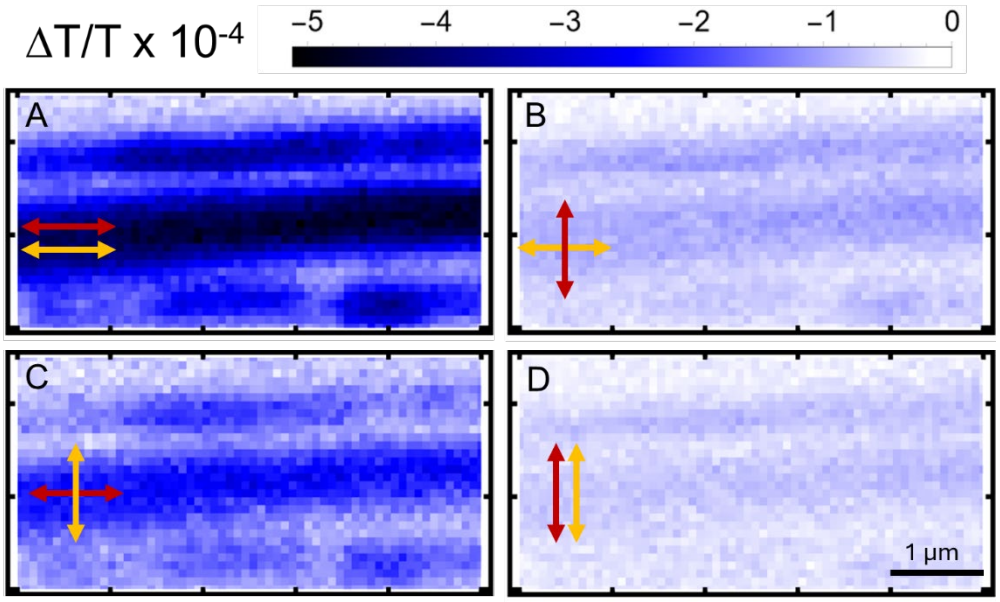

Figure A8: Polarization dependent spatially overlapped pump probe images. The pump polarization is depicted with the yellow arrow and the probe in red.

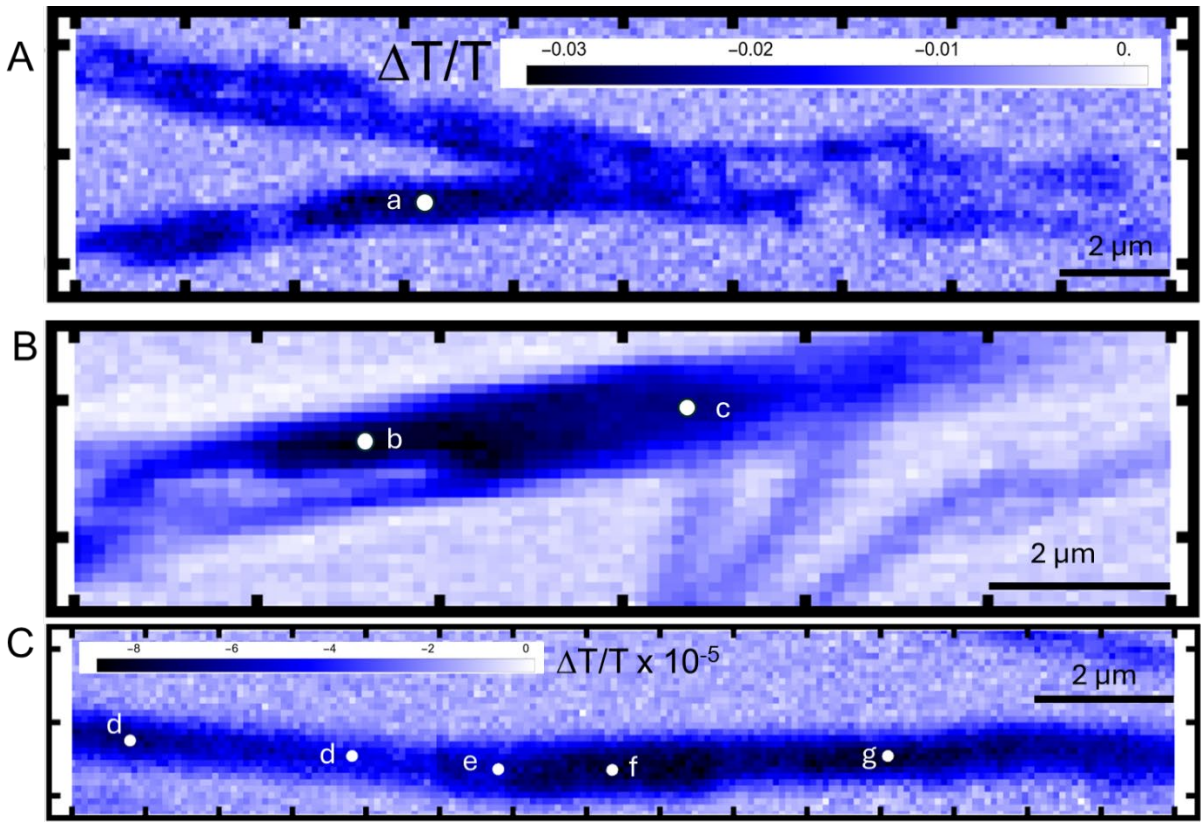

Figure A9: Spatially overlapped images of wires used in diffusion measurements. Locations where diffusion measurements are denoted with spots and letters (a-g). Diffusion fits are displayed in Figure A11. Note: Panels A and B share the same scale bar.

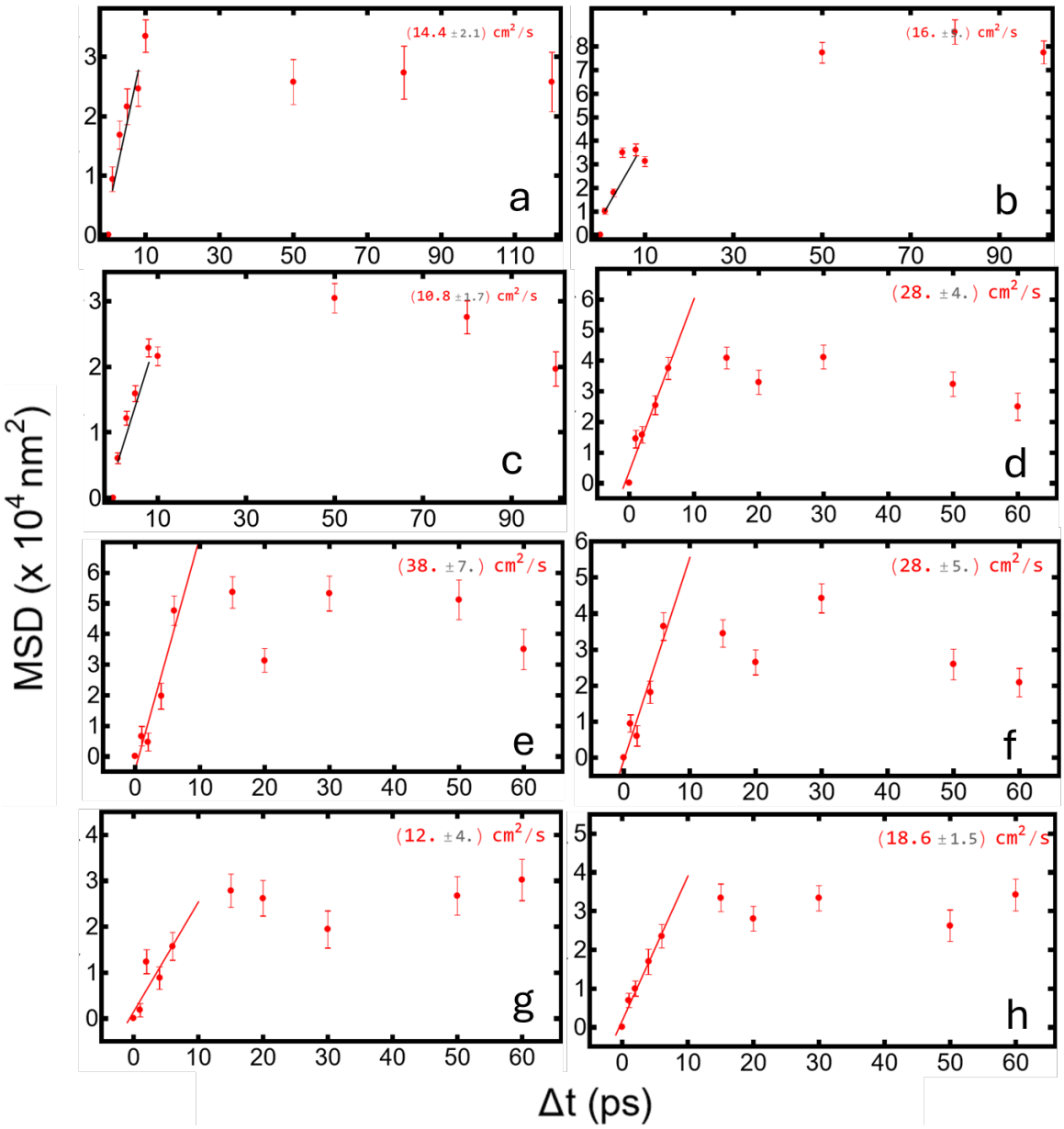

Figure A10: Diffusion fits that correspond to the locations taken in Figure A10.

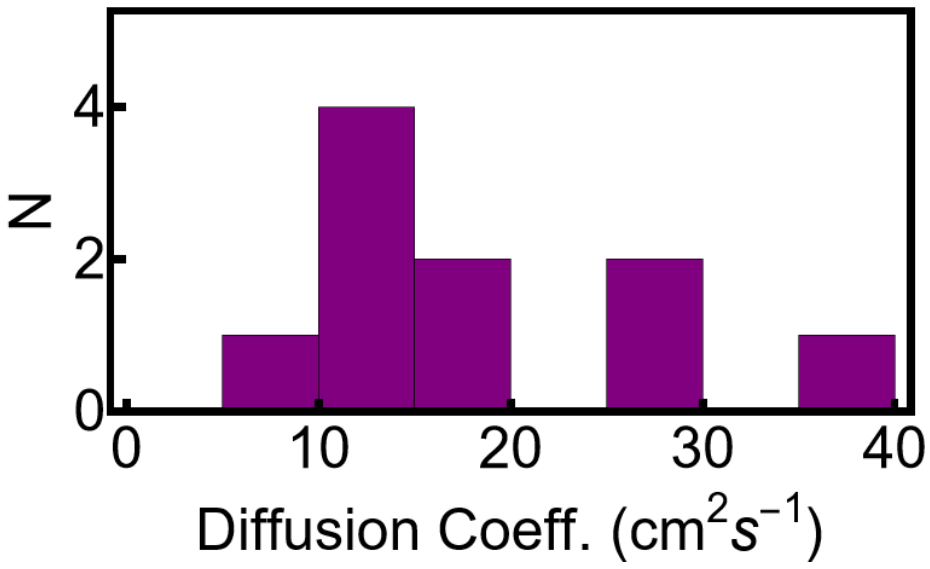

Figure A11: Histogram of the diffusion coefficient measured on the BODIPY ribbons, extracted from Figure A11.

APPENDIX B

SUPPORTING INFORMATION FOR "*FROM MONOMERS TO AGGREGATES TO SOLID-STATE FILMS: UNIQUE INSIGHT INTO ZINC PORPHYIN H-AGGREGATES"*

Experimental Details

Below are the experimental details used in chapter 4.

Synthesis

Synthesis of the porphyrin molecule is unavailable at this time due to the sensitive nature of the novel synthetic route for this molecule.

Pump Probe Microscope – Two color

Pump probe microscopy experiments were performed using a Spectra Physics MaiTai (~80 fs pulse width, 80 MHz repetition rate, 800 nm fundamental). The fundamental beam is split into the pump and probe lines using a plate beamsplitter. The pump line is passed through an acoustic optic modulator (AOM) to reduce the repetition rate of the pulse train to 2 MHz and modulate with a 50% duty cycle at 60 kHz. The modulated pump is focused through a photonic crystal fiber (PCF) to generate a white light supercontinuum which is passed through a 500 (+/- 5 nm) nm band pass filter to select the pump wavelength. The spectrally filtered pump is coupled to an optical delay stage to achieve a temporal delay from that of the probe line. The pump line is coupled, via a pair of galvanometer (GV) mirrors, through a 4-f telescope and combined with the probe with a dichroic beamsplitter. The probe line is first modulated to 2 MHz via an AOM to match the repetition rate of the pump. The combined beams are sent onto a set of GV mirrors, through a 4-f telescope, and coupled into the back aperture of a 100x plan apo objective to focus onto the sample. The two beams are collected with a condenser and the pump beam filtered out using a long pass filter. The probe is focused onto an amplified silicon photodiode. The APD signal is split (Mini Circuits ZFRSC-2050+) and one output it sent to a Stanford Research lock-in amplifier to demodulate the

signal at 120 kHz (ΔT). The other is coupled to a National Instruments DAQ card for the reference (T).

Figure B1 Plot legends correspond to the power of the pump beam. At 2 MHz on a 50% duty cycle and a spot size of 612 nm at 1/e2 the powers of 0.2, 0.3, 0.4, 0.5, 0.6, 0.75,1.0 μW corresponds to 33.91, 50.87, 57.82, 84.78, 127.20, 169.60 μJ cm^{-2}, respectively. Even at the upper limit of a high fluence 169.6 μJcm^{-2}, there is no indication of any non-linear recombination processes (fig. B1). However, due to the time scale of the experiments, prolonged exposure on the films at fluences greater than 84 μJcm-2 results in visual decomposition of the film.

Femtosecond Transient Absorption (TA)

Transient spectra were collected on a home built transient absorption instrument. Pump and probe pulses were derived from a commercial ultrafast fiber laser (Coherent Monaco 1035, 40 Watt, 1 MHz, 272 fs pulse duration, 1035±5 nm). The pump beam was modulated with an acousto-optic modulator at 16.125 kHz, coupled onto a 600 mm delay stage, and frequency doubled in a type-I BBO crystals. The resultant 517.5 nm light was attenuated using neutral density filters and focused onto the sample using a spherical 500 mm focal length aluminum mirror. The probe was generated by focusing a portion of the 1035 nm fundamental into an yttrium aluminum garnet (YAG) crystal and collimated using reflective optics. Magic angle polarization was set with a broadband waveplate, and the probe was focused and overlapped with the pump using a 250 mm FL spherical mirror. Transmitted probe light was coupled into a homebuilt spectrograph and imaged onto a high-speed line camera synched to collect lines at 62.5 kHz, four times the frequency of the pump modulation, to collect both “pump on” and “pump off” lines (on, on, off, off). The

unconventional modulation scheme was used to eliminate systematic noise introduced by the line camera's dual ADCs when subsequent lines are subtracted.

Supporting Data

Below are the supporting data used in chapter 4.

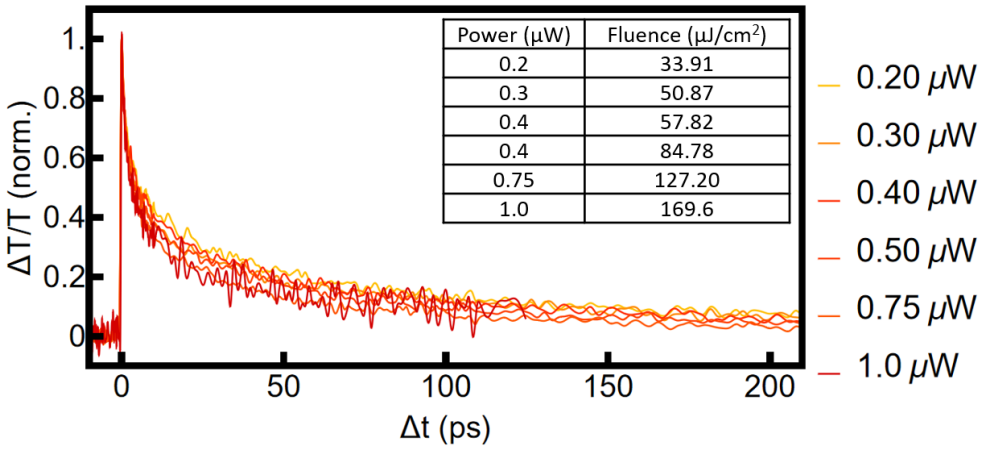

Figure B1: Power dependent kinetics of the PZn monomer. Sample degradation becomes evident after fluences above 169 μJ/cm^2. Inset has the corresponding fluence to power at 4MHz rep rate.

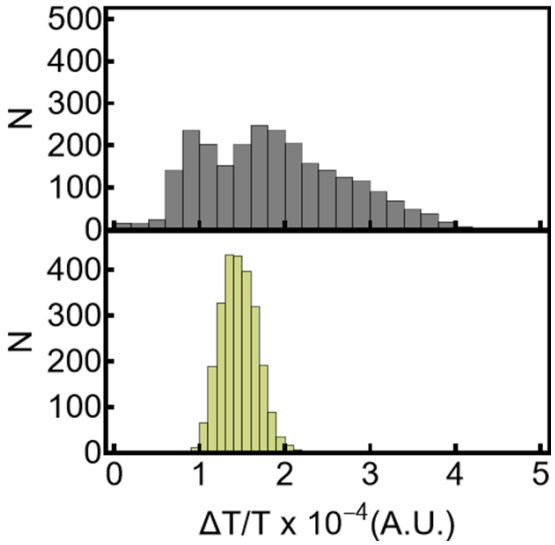

Figure B2: Histogram for the pixel data extracted from Figure 4.3 A and B. The top panel corresponds to the monomer and the bottom corresponds to aggregate.

Table B1: Fitting parameters for the excited state absorption decay

	Solution-phase				Solid-state			
	Agg	Std. Error	Monomer	Std. Error	Agg	Std. Error	Monomer	Std. Error
A_1	0.164	0.007	0.231	0.008	0.163	0.014	0.275	0.002
A_2	0.259	0.008	0.766	0.003	0.327	0.010	0.410	0.005
A_3	0.363	0.007	--	--	0.205	0.008	0.326	0.005
τ_1 (ps)	4	0.4	23.238	2	1.6	0.09	2.0	0.07
τ_2 (ps)	100	6	1628.84	13	8.7	0.55	13.8	0.28
τ_3 (ps)	682	12	--	--	70.9	0.25	199.9	2.42

APPENDIX C

SUPPORTING INFORMATION FOR "*COVALENTLY TETHERED ASSEMBLIES IMPROVE ENERGETIC HOMOGENEITY AND EXCITON TRANSPORT IN ORGANIC MATERIALS"*

Experimental Details

Below are the experimental details used in chapter 5.

Film Fabrication

Thin films were drop-casted from aqueous solutions onto borosilicate microscope slides under ambient conditions. This process produces characteristic "coffee-ring" type patterns, which reflect the complicated interplay of many parameters during the drying process, e.g. droplet size, temperature, solvent viscosity, and surface tension.[136] Spectroscopic measurements were performed near the edge of the films, where PBI deposition was most dense.

X-ray diffraction

X-ray diffraction was measured using a Bruker D8 Advance Power X-ray Diffractometer with a Cu X-ray source in Grazing Incidence Diffraction geometry. The source was held constant at 0.100^{o} while the detector angle was varied. Films of the PBI-TEG and Stap-2 were prepared as above on a glass substrate.

Pump Probe Microscopy

Pump probe microscopy experiments were performed using a Spectra Physics MaiTai (~80 fs pulse width, 80 MHz repetition rate, 800 nm fundamental). The fundamental beam is split into the pump and probe lines using a plate beamsplitter. The pump line is passed through an acoustic optic modulator (AOM) to reduce the repetition rate of the pulse train to 8 MHz and modulate with a 50% duty cycle at 60 kHz. The modulated pump is focused through a photonic crystal fiber (PCF) to generate a white light supercontinuum which is passed through a 500 (+/- 5 nm) nm band pass filter to select the pump wavelength. The spectrally filtered pump is coupled to an optical delay

stage to achieve a temporal delay from that of the probe line. The pump line is coupled, via a pair of galvanometer (GV) mirrors, through a 4-f telescope and combined with the probe with a dichroic beamsplitter. The probe line is first modulated to 8 MHz via an AOM to match the repetition rate of the pump. The combined beams are sent onto a set of GV mirrors, through a 4-f telescope, and coupled into the back aperture of a 100x plan apo objective to focus onto the sample. The two beams are collected with a condenser and the pump beam filtered out using a long pass filter. The probe is focused onto an amplified silicon photodiode. The APD signal is split (Mini Circuits ZFRSC-2050+) and one output it sent to a Stanford Research lock-in amplifier to demodulate the signal at 60 kHz (ΔT). The other is coupled to a National Instruments DAQ card for the reference (T).

To ensure linear excitation and decay dynamics, the pump fluence was kept low at ~85 μJ cm^{-1}, to remain in the power independent regime (Figure S2). Plot legends correspond to the power of the pump beam. At 8 MHz on a 50% duty cycle and a spot size of 612 nm at $1/e^2$ the powers of 0.250, 0.5, 0.75, 1, 1.5, 2, 3, 4, 5, 6, 8, 10 μW corresponds to 21.2, 42.4, 63.6, 84.8, 127, 170, 254, 339, 424, 509, 678, 848 μJ cm^{-2}, respectively. Even at the upper limit of a high fluence 848 μJ cm^{-2}, there is no indication of any non-linear recombination processes. However, due to the time scale of the experiments, prolonged exposure on the films at fluences greater than 250 μJ cm^{-2} results in discoloration of the pink films. Excited state transport was determined to be isotropic (Fig. 5.3A in main text), and so spatially offset scans were performed along a single axis to allow for more averaging. Each time delayed frame is the average of twenty spatially separated scans along a single axis, for pump probe delays between $\Delta t = 0$ and 150 ps to calculate the diffusion, Fig. 5.3B in the main text.

Supporting Data

Below are the supporting data used in chapter 5.

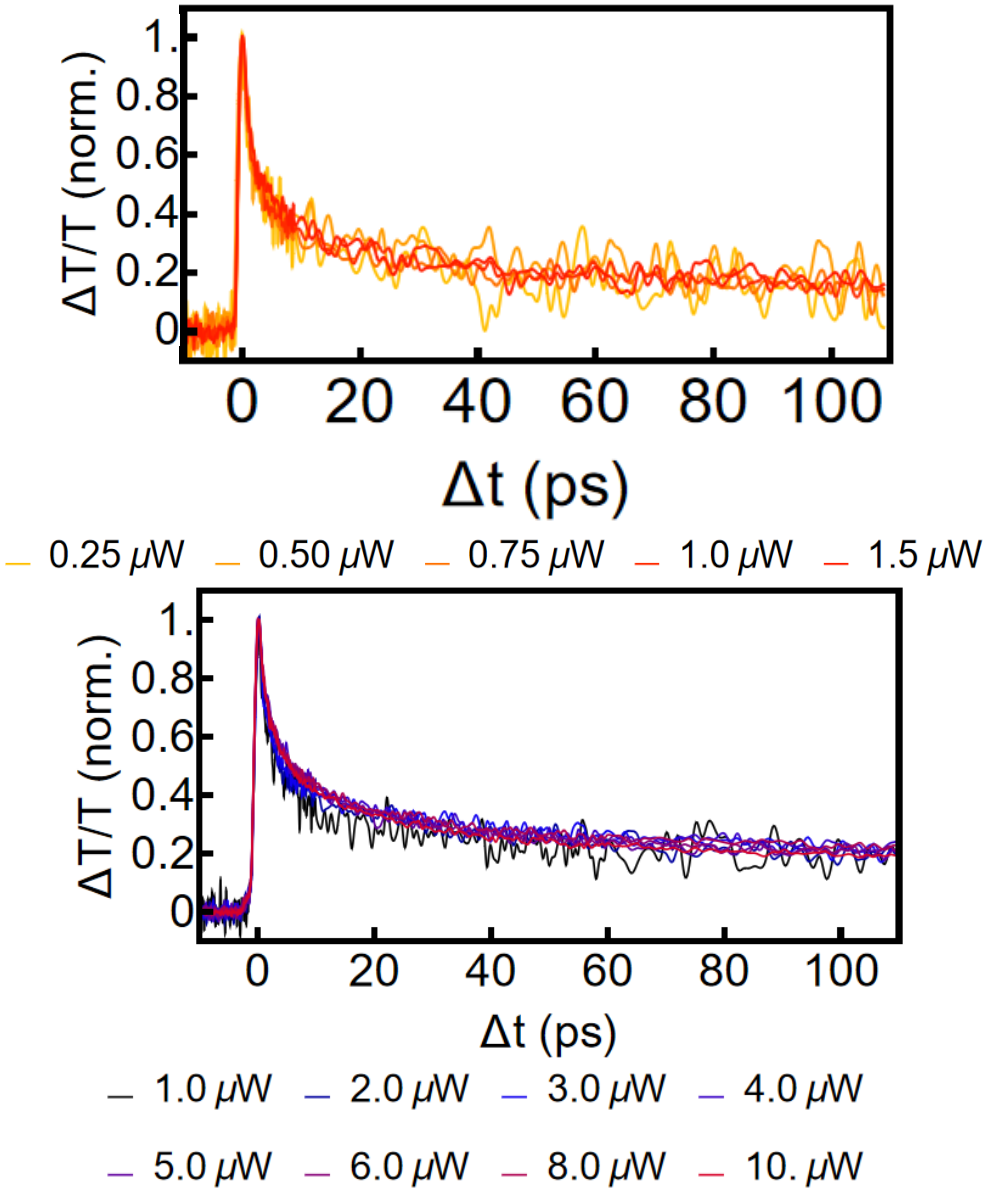

Figure C1: Power dependent studies on A) Control PBI-TEG B) PBI-STAP 2.

Table C1: Measured diffusion constants on the Locked PBI-Stap-2 and control PBI-TEG films.

PBI-STAP-2		**Control PBI-TEG**	
D (cm^2/s)	Std. Error	D (cm^2/s)	Std. Error
1.0	0.6	1.1	0.3
2.0	0.5	1.14	0.32
2.0	0.7	1.7	1.2
1.8	0.5	0.7	0.5
2.5	0.5	1.5	1
1.3	0.4	0.55	0.26
2.6	0.4	1.6	0.7
1.5	0.5	1.3	0.6
2.5	0.6	1.2	0.3
2.1	0.27	0.83	0.24
2.0	2.6	1.2	0.8
1.3	0.27	0.6	0.4
2.4	0.16		
2.1	0.17		
2.1	0.22		

Kinetic Monte Carlo Modeling

This section describes the kinetic Monte Carlo (KMC) model223 for the two samples: PBI-TEG and PBI-Stap-2.

Each film is parameterized by a site-to-site distance and site energies that sample a Gaussian distribution of states. Because pump probe measurements are performed in the power independent regime, excitons are assumed to propagate independently. A Miller-Abrahams[219] expression is adopted for the hoping rate:

$$k_{ij} = \nu \, Exp\left[-2\alpha r_{ij}\right] \begin{cases} Exp\left[\frac{-\Delta E_{ij}}{kT}\right] & \Delta E_{ij} > 0 \\ 1 & \Delta E_{ij} \leq 0 \end{cases} \qquad \text{(C.1)}$$

Where k_{ij} is the hopping rate from site $i \rightarrow j$, ν is the attempt to hop frequency, α is the inverse delocalization length, r_{ij} is the distance of the hop from $i \rightarrow j$, ΔE_{ij} is the change in energy

from i → j, and kT is the Boltzmann energy at room temperature. A 3D grid is generated with each site parameterized by an energy randomly selected from the energetic distribution. Transition rates, k_{ij}, to each of the six nearest neighboring sites are tabulated according to Eq. SI 1. Each exciton is placed randomly on the grid using a pseudo random number generator. For each time step, τ, the exciton hop i → j is determined by a weighted random selection. The probability of hop i → j is given by $p_{ij} = k_{ij}/\sum_l k_{il}$, where the denominator sums over the six nearest neighbors to site i. The hop time τ is determined by $\tau = -Ln[r]/\sum_l k_{il}$, where r is a random number selected on the interval (0,1). At each step, the exciton recombines with a cumulative probability determined by the two decay rates experimentally observed. After termination, the mean squared displacement (MSD) of each exciton is calculated, with the diffusion constant, D, is given by:

$$D = \frac{1}{6}\frac{(x_f - x_0)^2}{t} \qquad \text{(C.2)}$$

Where x_f is the final position and x_0 is the starting position, and t is exciton lifetime.

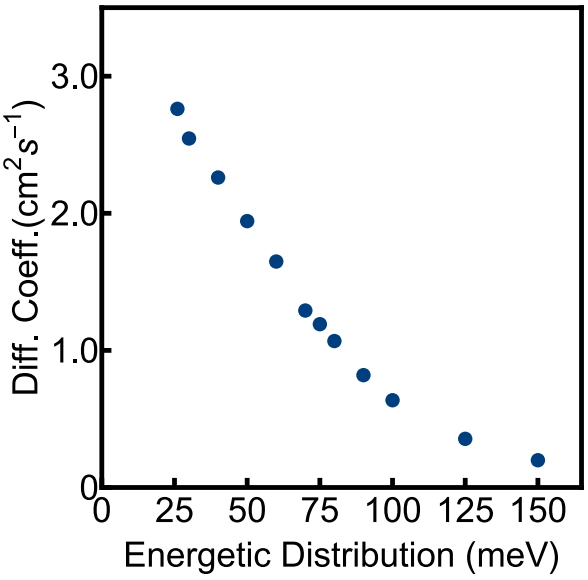

Figure C2: Dependence of the population averaged diffusion constant on the width of the Gaussian distribution of site energies.

Models of the films use a 3D cubic grid with a side length of 50 nm. Site energies were randomly selected from a Gaussian distribution with width spanning 26 – 100 meV. To reproduce the average D value experimentally observed, an inverse localization length of 2 nm and the attempt to hop frequency of 1 fs^{-1} was chosen.[224] Note that this simple model assumes that transport occurs only through incoherent hopping[225], and so physically unrealistic hopping rates are necessary to reproduce the ~ 1 cm^2s^{-1} rate observed experimentally. Diffusion constants shown in Fig. C2 are obtained by averaging D determined for 500 trajectories, with an average diffusion coefficient of 1.19 cm/2 s^{-1} at a distribution of 75 meV.

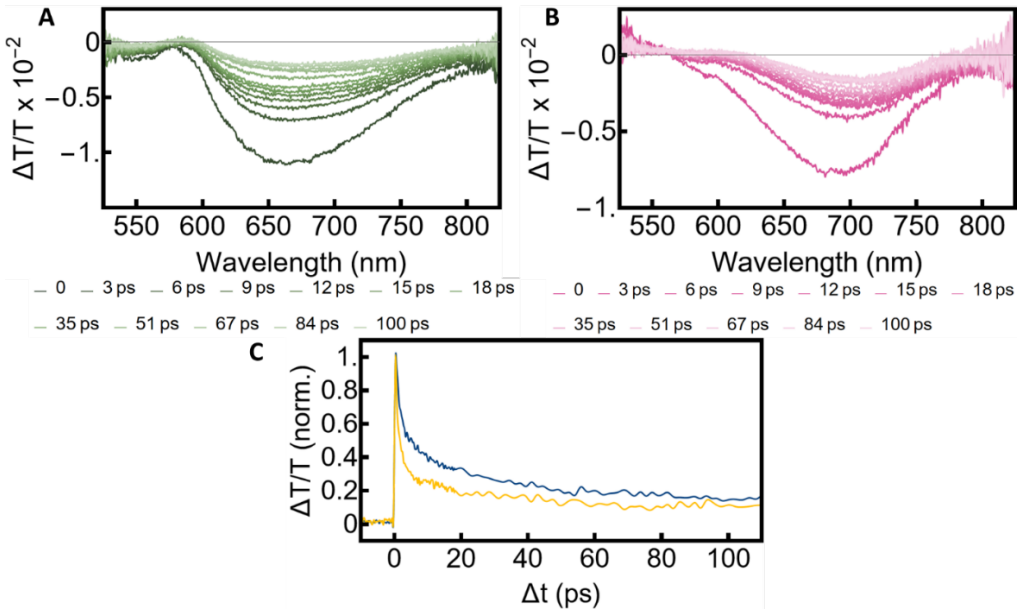

Figure C3: Transient transmission spectra of the PBI-TEG (A) and PBI-Stap-2 (B) films for delay times up to 100 ps. C) Integrated (between 665 and 670 nm) kinetics for PBI-TEG (Blue) and PBI-Stap-2 (Gold).

Transient transmission spectra collected on thin films of PBI-Stap-2 and PBI-TEG (Fig. S3) are consistent with previously reported broadband spectra for the solvated assemblies (note that in ref. 6, PBI-TEG is called PBI-Non-Cov).[196] For both films, the broad excited state absorption spanning ~ 600 nm – 850 nm is consistent with an excited state of mixed Frenkel/charge-transfer exciton character, with the singlet exciton dominating the blue edge of the PIA and anionic character dominating the red edge. The more strongly redshifted spectrum of the PBI-Stap-2 film indicates stronger charge transfer character, again, consistent with the solution-phase transient absorption spectra reported in ref 6. Both films show a dynamic redshift of the transient spectra attributed to structural relaxation. Note that the attenuating signal intensity red of 750 nm is in part caused by chromatic aberrations which reduces the pump probe spatial overlap.[208]

One significant difference between the solution-phase and solid-state spectroscopic data is the significantly shorter excited state lifetime in the solid-state. Whereas the excited state lifetimes for solution-phase PBI-TEG and PBI-Stap-2 were reported to be τ = 373 ps and τ = 235 ps, respectively[196], the lifetimes obtained in the solid-state are significantly shorter. Fitting the spectrally integrated kinetics shown in Fig C.5C with a biexponential decay function yields a short lifetime of 3.7 +/- 0.2 ps (A_1=0.64) and a long lifetime of 133.9 +/- 5.5 ps (A_2=0.36) for the PBI-TEG film. Fits to the PBI-Stap-2 kinetic decay yields a short lifetime of 1.7 +/- 0.1 ps (A_1=0.79) and a long lifetime of 172.7 +/- 11.2 ps (A_2=0.21). These lifetimes are consistent with the lifetimes measured with the two color pump probe microscope at a probe wavelength of 800 nm (Fig. 5.2A in the main manuscript). We attribute the discrepancy between solution-phase and solid-state lifetime to the significant difference in dielectric environment. The solution-phase spectroscopy in Paulino et. al.[196] was performed in water, which will act to significantly screen the coulomb coupling of, e.g. charge transfer excitons, resulting in slower recombination. In contrast, the dielectric constant of the thin films is likely to be 40-60 times lower than water, which is likely to result in faster recombination.

CUMULATIVE REFERENCES CITED

(1) Najafpour, M. M.; Shen, J.-R.; Allakhverdiev, S. I. Natural and artificial photosynthesis: fundamentals, progress, and challenges. *Photosynthesis Research* **2022**, *154* (3), 229-231.

(2) Mikhnenko, O. V.; Blom, P. W. M.; Nguyen, T.-Q. Exciton diffusion in organic semiconductors. *Energy & Environmental Science* **2015**, *8* (7), 1867-1888, 10.1039/C5EE00925A.

(3) Brixner, T.; Hildner, R.; Köhler, J.; Lambert, C.; Würthner, F. Exciton Transport in Molecular Aggregates - From Natural Antennas to Synthetic Chromophore Systems. *Advanced Energy Materials* **2017**, *7* (16), 1700236.

(4) Akselrod, G. M.; Deotare, P. B.; Thompson, N. J.; Lee, J.; Tisdale, W. A.; Baldo, M. A.; Menon, V. M.; Bulović, V. Visualization of exciton transport in ordered and disordered molecular solids. *Nature Communications* **2014**, *5* (1), 3646.

(5) Mas-Torrent, M.; Rovira, C. Role of Molecular Order and Solid-State Structure in Organic Field-Effect Transistors. *Chemical Reviews* **2011**, *111* (8), 4833-4856.

(6) Coropceanu, V.; Cornil, J.; Da Silva Filho, D. A.; Olivier, Y.; Silbey, R.; Brédas, J.-L. Charge Transport in Organic Semiconductors. *Chemical Reviews* **2007**, *107* (4), 926-952.

(7) Caram, J. R.; Doria, S.; Eisele, D. M.; Freyria, F. S.; Sinclair, T. S.; Rebentrost, P.; Lloyd, S.; Bawendi, M. G. Room-Temperature Micron-Scale Exciton Migration in a Stabilized Emissive Molecular Aggregate. *Nano Letters* **2016**, *16* (11), 6808-6815.

(8) Mascaro, D. J.; Thompson, M. E.; Smith, H. I.; Bulović, V. Forming oriented organic crystals from amorphous thin films on patterned substrates via solvent-vapor annealing. *Organic Electronics* **2005**, *6* (5), 211-220.

(9) Guo, X.; Li, H.; Han, Y.; Yang, Y.; Luo, Q.; Ma, C.-Q.; Yang, J. Fully doctor-bladed efficient organic solar cells processed under ambient condition. *Organic Electronics* **2020**, *82*, 105725.

(10) Fleischmann, E.-K.; Zentel, R. Liquid-Crystalline Ordering as a Concept in Materials Science: From Semiconductors to Stimuli-Responsive Devices. *Angewandte Chemie International Edition* **2013**, *52* (34), 8810-8827.

(11) McDermott, G.; Prince, S. M.; Freer, A. A.; Hawthornthwaite-Lawless, A. M.; Papiz, M. Z.; Cogdell, R. J.; Isaacs, N. W. Crystal structure of an integral membrane light-harvesting complex from photosynthetic bacteria. *Nature* **1995**, *374* (6522), 517-521.

(12) Bässler, H. Charge Transport in Disordered Organic Photoconductors a Monte Carlo Simulation Study. *physica status solidi (b)* **1993**, *175* (1), 15-56.

(13) Hervet, H.; Dianoux, A. J.; Lechner, R. E.; Volino, F. Neutron scattering study of methyl group rotation in solid para-azoxyanisole (PAA). *J. Phys. France* **1976**, *37* (5), 587-594, 10.1051/jphys:01976003705058700.

(14) Llamas-Saiz, A. L.; Foces-Foces, C.; Fontenas, C.; Jagerovic, N.; Elguero, J. The search for proton mobility in solid pyrazoles: molecular and crystal structure of 3(5)-phenyl-4-bromo-5(3)-methylpyrazole. *Journal of Molecular Structure* **1999**, *484* (1), 197-205.

(15) White, M. A.; Wasylishen, R. E.; Eaton, P. E.; Xiong, Y.; Pramod, K.; Nodari, N. Orientational disorder in solid cubane: a thermodynamic and carbon-13 NMR study. *The Journal of Physical Chemistry* **1992**, *96* (1), 421-425.

(16) Reiser, P.; Konrad, M.; Fediai, A.; Léon, S.; Wenzel, W.; Friederich, P. Analyzing Dynamical Disorder for Charge Transport in Organic Semiconductors via Machine Learning. *Journal of Chemical Theory and Computation* **2021**, *17* (6), 3750-3759.

(17) Ishii, H.; Kobayashi, N.; Hirose, K. Carrier transport calculations of organic semiconductors with static and dynamic disorder. *Japanese Journal of Applied Physics* **2019**, *58* (11), 110501.

(18) Köhler, A.; dos Santos, D. A.; Beljonne, D.; Shuai, Z.; Brédas, J. L.; Holmes, A. B.; Kraus, A.; Müllen, K.; Friend, R. H. Charge separation in localized and delocalized electronic states in polymeric semiconductors. *Nature* **1998**, *392* (6679), 903-906.

(19) Fishchuk, I. I.; Kadashchuk, A.; Hoffmann, S. T.; Athanasopoulos, S.; Genoe, J.; Bässler, H.; Köhler, A. Unified description for hopping transport in organic semiconductors including both energetic disorder and polaronic contributions. *Physical Review B* **2013**, *88* (12), 125202.

(20) Kaliyaraj Selva Kumar, A.; Zhang, Y.; Li, D.; Compton, R. G. A mini-review: How reliable is the drop casting technique? *Electrochemistry Communications* **2020**, *121*, 106867.

(21) Deegan, R. D.; Bakajin, O.; Dupont, T. F.; Huber, G.; Nagel, S. R.; Witten, T. A. Capillary flow as the cause of ring stains from dried liquid drops. *Nature* **1997**, *389* (6653), 827-829.

(22) Schön, J. H.; Batlogg, B. Modeling of the temperature dependence of the field-effect mobility in thin film devices of conjugated oligomers. *Applied Physics Letters* **1999**, *74* (2), 260-262.

(23) Jagoo, Z.; Lamport, Z. A.; Jurchescu, O. D.; McNeil, L. E. Efficiency enhancement of organic thin-film phototransistors due to photoassisted charge injection. *Applied Physics Letters* **2021**, *119* (7), 073302.

(24) Wen, Y.; Liu, Y.; Guo, Y.; Yu, G.; Hu, W. Experimental Techniques for the Fabrication and Characterization of Organic Thin Films for Field-Effect Transistors. *Chemical Reviews* **2011**, *111* (5), 3358-3406.

(25) Brédas, J.-L.; Norton, J. E.; Cornil, J.; Coropceanu, V. Molecular Understanding of Organic Solar Cells: The Challenges. *Accounts of Chemical Research* **2009**, *42* (11), 1691-1699.

(26) Kasha, M. Energy Transfer Mechanisms and the Molecular Exciton Model for Molecular Aggregates. *Radiation Research* **1963**, *20* (1), 55-70.

(27) Kistler, K. A.; Pochas, C. M.; Yamagata, H.; Matsika, S.; Spano, F. C. Absorption, Circular Dichroism, and Photoluminescence in Perylene Diimide Bichromophores: Polarization-Dependent H- and J-Aggregate Behavior. *The Journal of Physical Chemistry B* **2012**, *116* (1), 77-86.

(28) Jelley, E. E. Spectral Absorption and Fluorescence of Dyes in the Molecular State. *Nature* **1936**, *138* (3502), 1009-1010.

(29) Scheibe, G. Reversible Polymerisation als Ursache neuartiger Absorptionsbanden von Farbstoffen. *Kolloid-Zeitschrift* **1938**, *82* (1), 1-14.

(30) Kopainsky, B.; Hallermeier, J. K.; Kaiser, W. K. The first step of aggregation of pic: the dimerization. *Chemical Physics Letters* **1981**, *83*, 498-502.

(31) Cooper, W. Multiplet structure of aggregated states in 1,1′-diethyl-2,2′-cyanine dye. *Chemical Physics Letters* **1970**, *7* (1), 73-77.

(32) Spano, F. C. EXCITONS IN CONJUGATED OLIGOMER AGGREGATES, FILMS, AND CRYSTALS. *Annual Review of Physical Chemistry* **2006**, *57* (1), 217-243.

(33) Hestand, N. J.; Spano, F. C. Molecular Aggregate Photophysics beyond the Kasha Model: Novel Design Principles for Organic Materials. *Accounts of Chemical Research* **2017**, *50* (2), 341-350.

(34) Eisfeld, A.; Briggs, J. S. The J- and H-bands of organic dye aggregates. *Chemical Physics* **2006**, *324* (2-3), 376-384.

(35) Spano, F. C.; Silva, C. H- and J-Aggregate Behavior in Polymeric Semiconductors. *Annual Review of Physical Chemistry* **2014**, *65* (1), 477-500.

(36) Avellanal-Zaballa, E.; Gartzia-Rivero, L.; Arbeloa, T.; Bañuelos, J. Fundamental photophysical concepts and key structural factors for the design of BODIPY-based tunable lasers. *International Reviews in Physical Chemistry* **2022**, *41* (2), 177-203.

(37) Menke, S. M.; Holmes, R. J. Exciton diffusion in organic photovoltaic cells. *Energy & Environmental Science* **2014**, *7* (2), 499-512, 10.1039/C3EE42444H.

(38) Pope, M.; Swenberg, C. E.; Pope, M. *Electronic processes in organic crystals and polymers / Martin Pope, Charles E. Swenberg*; Oxford University Press, 1999.

(39) Gao, M.; Paul, S.; Schwieters, C. D.; You, Z.-Q.; Shao, H.; Herbert, J. M.; Parquette, J. R.; Jaroniec, C. P. A Structural Model for a Self-Assembled Nanotube Provides Insight into Its Exciton Dynamics. *The Journal of Physical Chemistry C* **2015**, *119* (24), 13948-13956.

(40) Scheblykin, I. G.; Yartsev, A.; Pullerits, T.; Gulbinas, V.; Sundström, V. Excited State and Charge Photogeneration Dynamics in Conjugated Polymers. *The Journal of Physical Chemistry B* **2007**, *111* (23), 6303-6321.

(41) Brédas, J.-L.; Beljonne, D.; Coropceanu, V.; Cornil, J. Charge-Transfer and Energy-Transfer Processes in π-Conjugated Oligomers and Polymers: A Molecular Picture. *Chemical Reviews* **2004**, *104* (11), 4971-5004.

(42) Ruini, A.; Caldas, M. J.; Bussi, G.; Molinari, E. Solid State Effects on Exciton States and Optical Properties of PPV. *Physical Review Letters* **2002**, *88* (20), 206403.

(43) Dexter, D. L. A Theory of Sensitized Luminescence in Solids. *The Journal of Chemical Physics* **1953**, *21* (5), 836-850.

(44) Dexter, D. L.; Knox, R. S.; Förster, T. The Radiationless Transfer of Energy of Electronic Excitation between Impurity Molecules in Crystals. *physica status solidi (b)* **1969**, *34* (2), K159-K162.

(45) Sekar, R. B.; Periasamy, A. Fluorescence resonance energy transfer (FRET) microscopy imaging of live cell protein localizations. *J Cell Biol* **2003**, *160* (5), 629-633.

(46) Scholes, G. D. Long-Range Resonance Energy Transfer in Molecular Systems. *Annual Review of Physical Chemistry* **2003**, *54* (Volume 54, 2003), 57-87.

(47) Cleave, V.; Yahioglu, G.; Barny, P. L.; Friend, R. H.; Tessler, N. Harvesting Singlet and Triplet Energy in Polymer LEDs. *Advanced Materials* **1999**, *11* (4), 285-288.

(48) Yavuz, I. Dichotomy between the band and hopping transport in organic crystals: insights from experiments. *Physical Chemistry Chemical Physics* **2017**, *19* (38), 25819-25828.

(49) Bai, S.; Zhang, P.; Antoniou, P.; Skourtis, S. S.; Beratan, David N. Quantum interferences among Dexter energy transfer pathways. *Faraday Discussions* **2019**, *216* (0), 301-318, 10.1039/C9FD00007K.

(50) Coehoorn, R.; Van Eersel, H.; Bobbert, P.; Janssen, R. Kinetic Monte Carlo Study of the Sensitivity of OLED Efficiency and Lifetime to Materials Parameters. *Advanced Functional Materials* **2015**, *25* (13), 2024-2037.

(51) Köhler, A.; Bässler, H. Triplet states in organic semiconductors. *Materials Science and Engineering: R: Reports* **2009**, *66* (4), 71-109.

(52) Bardeen, C. J. The Structure and Dynamics of Molecular Excitons. *Annual Review of Physical Chemistry* **2014**, *65* (Volume 65, 2014), 127-148.

(53) Bjorgaard, J. A.; Köse, M. E. Simulations of singlet exciton diffusion in organic semiconductors: a review. *RSC Advances* **2015**, *5* (11), 8432-8445, 10.1039/C4RA12409J.

(54) Huff, J. S.; Turner, D. B.; Mass, O. A.; Patten, L. K.; Wilson, C. K.; Roy, S. K.; Barclay, M. S.; Yurke, B.; Knowlton, W. B.; Davis, P. H.; et al. Excited-State Lifetimes of DNA-Templated Cyanine Dimer, Trimer, and Tetramer Aggregates: The Role of Exciton Delocalization, Dye

Separation, and DNA Heterogeneity. *The Journal of Physical Chemistry B* **2021**, *125* (36), 10240-10259.

(55) Cunningham, P. D.; Kim, Y. C.; Díaz, S. A.; Buckhout-White, S.; Mathur, D.; Medintz, I. L.; Melinger, J. S. Optical Properties of Vibronically Coupled Cy3 Dimers on DNA Scaffolds. *The Journal of Physical Chemistry B* **2018**, *122* (19), 5020-5029.

(56) Huff, J. S.; Davis, P. H.; Christy, A.; Kellis, D. L.; Kandadai, N.; Toa, Z. S. D.; Scholes, G. D.; Yurke, B.; Knowlton, W. B.; Pensack, R. D. DNA-Templated Aggregates of Strongly Coupled Cyanine Dyes: Nonradiative Decay Governs Exciton Lifetimes. *The Journal of Physical Chemistry Letters* **2019**, *10* (10), 2386-2392.

(57) Deshmukh, A. P.; Geue, N.; Bradbury, N. C.; Atallah, T. L.; Chuang, C.; Pengshung, M.; Cao, J.; Sletten, E. M.; Neuhauser, D.; Caram, J. R. Bridging the gap between H- and J-aggregates: Classification and supramolecular tunability for excitonic band structures in two-dimensional molecular aggregates. *Chemical Physics Reviews* **2022**, *3* (2), 021401.

(58) Zhao, Y.; Wang, V.; Javey, A. Molecular Materials with Short Radiative Lifetime for High-Speed Light-Emitting Devices. *Matter* **2020**, *3* (6), 1832-1844.

(59) Treibs, A.; Kreuzer, F.-H. Difluorboryl-Komplexe von Di- und Tripyrrylmethenen. *Justus Liebigs Annalen der Chemie* **1968**, *718* (1), 208-223.

(60) Boens, N.; Leen, V.; Dehaen, W. Fluorescent indicators based on BODIPY. *Chemical Society Reviews* **2012**, *41* (3), 1130-1172, 10.1039/C1CS15132K.

(61) Kaur, P.; Singh, K. Recent advances in the application of BODIPY in bioimaging and chemosensing. *Journal of Materials Chemistry C* **2019**, *7* (37), 11361-11405, 10.1039/C9TC03719E.

(62) Wang, J.; Gong, Q.; Wang, L.; Hao, E.; Jiao, L. The main strategies for tuning BODIPY fluorophores into photosensitizers. *Journal of Porphyrins and Phthalocyanines* **2020**, *24* (05n07), 603-635.

(63) Waghorn, P. A.; Jones, M. W.; McIntyre, A.; Innocenti, A.; Vullo, D.; Harris, A. L.; Supuran, C. T.; Dilworth, J. R. Targeting Carbonic Anhydrases with Fluorescent BODIPY-Labelled Sulfonamides. *European Journal of Inorganic Chemistry* **2012**, *2012* (17), 2898-2907.

(64) Liu, J.-Y.; Yeung, H.-S.; Xu, W.; Li, X.; Ng, D. K. P. Highly Efficient Energy Transfer in Subphthalocyanine−BODIPY Conjugates. *Organic Letters* **2008**, *10* (23), 5421-5424.

(65) Banfi, S.; Nasini, G.; Zaza, S.; Caruso, E. Synthesis and photo-physical properties of a series of BODIPY dyes. *Tetrahedron* **2013**, *69* (24), 4845-4856.

(66) Bonardi, L.; Ulrich, G.; Ziessel, R. Tailoring the Properties of Boron−Dipyrromethene Dyes with Acetylenic Functions at the 2,6,8 and 4-B Substitution Positions. *Organic Letters* **2008**, *10* (11), 2183-2186.

(67) Zatsikha, Y. V.; Nemez, D. B.; Davis, R. L.; Singh, S.; Herbert, D. E.; King, A. J.; Ziegler, C. J.; Nemykin, V. N. Testing the Limits of the BOPHY Platform: Preparation, Characterization, and Theoretical Modeling of BOPHYs and Organometallic BOPHYs with Electron-Withdrawing Groups at β-Pyrrolic and Bridging Positions. *Chemistry – A European Journal* **2017**, *23* (59), 14786-14796.

(68) Didukh, N. O.; Zatsikha, Y. V.; Rohde, G. T.; Blesener, T. S.; Yakubovskyi, V. P.; Kovtun, Y. P.; Nemykin, V. N. NIR absorbing diferrocene-containing meso-cyano-BODIPY with a UV-Vis-NIR spectrum remarkably close to that of magnesium tetracyanotetraferrocenyltetraazaporphyrin. *Chemical Communications* **2016**, *52* (77), 11563-11566, 10.1039/C6CC06344F.

(69) Benitz, A.; Thomas, M. B.; de Silva, I.; Nesterov, V. N.; Verbeck Iv, G. F.; D'Souza, F. Photoinduced Electron Transfer in Axially Coordinated Supramolecular Zinc Tetrapyrrole Bis(styryl)BODIPY Donor-Acceptor Conjugates. *ChemPhotoChem* **2021**, *5* (3), 260-269.

(70) Ziegler, C. J.; Chanawanno, K.; Hasheminsasab, A.; Zatsikha, Y. V.; Maligaspe, E.; Nemykin, V. N. Synthesis, redox properties, and electronic coupling in the diferrocene aza-dipyrromethene and azaBODIPY donor-acceptor dyad with direct ferrocene-α-pyrrole bond. *Inorg Chem* **2014**, *53* (9), 4751-4755.

(71) Xia, Q.; Yang, J.; Zhang, S.; Zhang, J.; Li, Z.; Wang, J.; Chen, X. Bodipy-Based Metal–Organic Frameworks Transformed in Solid States from 1D Chains to 2D Layer Structures as Efficient Visible Light Heterogeneous Photocatalysts for Forging C–B and C–C Bonds. *Journal of the American Chemical Society* **2023**, *145* (11), 6123-6134.

(72) Kreno, L. E.; Leong, K.; Farha, O. K.; Allendorf, M.; Van Duyne, R. P.; Hupp, J. T. Metal–Organic Framework Materials as Chemical Sensors. *Chemical Reviews* **2012**, *112* (2), 1105-1125.

(73) El-Ali, H. A. A.; Jing, J.; Zhang, X. Solid-state emissive O-BODIPY dyes with bimodal emissions across red and near infrared region. *RSC Adv* **2019**, *9* (28), 16246-16251.

(74) Gartzia-Rivero, L.; Ray Leiva, C.; Sánchez-Carnerero, E. M.; Bañuelos, J.; Moreno, F.; Maroto, B. L.; García-Moreno, I.; Infantes, L.; Mendez, B.; López-Arbeloa, I.; et al. Chiral Microneedles from an Achiral Bis(boron dipyrromethene): Spontaneous Mirror Symmetry Breaking Leading to a Promising Photoluminescent Organic Material. *Langmuir* **2019**, *35* (14), 5021-5028.

(75) Yin, J.-F.; Hu, Y.; Wang, H.; Jin, Z.; Zhang, Y.; Kuang, G.-C. Near-Infrared-Emissive Amphiphilic BODIPY Assemblies Manipulated by Charge-Transfer Interaction: From Nanofibers to Nanorods and Nanodisks. *Chemistry – An Asian Journal* **2017**, *12* (23), 3088-3095.

(76) Fu, G.-L.; Pan, H.; Zhao, Y.-H.; Zhao, C.-H. Solid-state emissive triarylborane-based BODIPY dyes: Photophysical properties and fluorescent sensing for fluoride and cyanide ions. *Organic & Biomolecular Chemistry* **2011**, *9* (23), 8141-8146, 10.1039/C1OB05959A.

(77) Chen, Z.; Liu, Y.; Wagner, W.; Stepanenko, V.; Ren, X.; Ogi, S.; Würthner, F. Near-IR Absorbing J-Aggregate of an Amphiphilic BF2-Azadipyrromethene Dye by Kinetic Cooperative Self-Assembly. *Angewandte Chemie International Edition* **2017**, *56* (21), 5729-5733.

(78) Kim, S.; Bouffard, J.; Kim, Y. Tailoring the Solid-State Fluorescence Emission of BODIPY Dyes by meso Substitution. *Chemistry – A European Journal* **2015**, *21* (48), 17459-17465.

(79) Antina, L. A.; Ksenofontov, A. A.; Kazak, A. V.; Usol'tseva, N. V.; Antina, E. V.; Berezin, M. B. Effect of ms-substitution on aggregation behavior and spectroscopic properties of BODIPY dyes in aqueous solution, Langmuir-Schaefer and poly(methyl methacrylate) thin films. *Colloids and Surfaces A: Physicochemical and Engineering Aspects* **2021**, *618*, 126449.

(80) Marfin, Y. S.; Usoltsev, S. D.; Kazak, A. V.; Vodyanova, O. S.; Novikova, N. E.; Verin, I. A.; Rumyantsev, E. V.; Kholodkov, I. V.; Merkushev, D. A. Supramolecular organization and optical properties of BODIPY derivatives in Langmuir–Schaefer films. *New Journal of Chemistry* **2020**, *44* (44), 19046-19053, 10.1039/D0NJ02855J.

(81) Poulos, T. L. Heme Enzyme Structure and Function. *Chemical Reviews* **2014**, *114* (7), 3919-3962.

(82) Scheer, H. An Overview of Chlorophylls and Bacteriochlorophylls: Biochemistry, Biophysics, Functions and Applications. In *Chlorophylls and Bacteriochlorophylls: Biochemistry, Biophysics, Functions and Applications*, Grimm, B., Porra, R. J., Rüdiger, W., Scheer, H. Eds.; Springer Netherlands, 2006; pp 1-26.

(83) Norvaiša, K.; Kielmann, M.; Senge, M. O. Porphyrins as Colorimetric and Photometric Biosensors in Modern Bioanalytical Systems. *ChemBioChem* **2020**, *21* (13), 1793-1807.

(84) Costa e Silva, R.; Oliveira da Silva, L.; de Andrade Bartolomeu, A.; Brocksom, T. J.; de Oliveira, K. T. Recent applications of porphyrins as photocatalysts in organic synthesis: batch and continuous flow approaches. *Beilstein Journal of Organic Chemistry* **2020**, *16*, 917-955.

(85) Ryan, A. A.; Senge, M. O. How green is green chemistry? Chlorophylls as a bioresource from biorefineries and their commercial potential in medicine and photovoltaics. *Photochemical & Photobiological Sciences* **2015**, *14* (4), 638-660, 10.1039/C4PP00435C.

(86) Hiroto, S.; Miyake, Y.; Shinokubo, H. Synthesis and Functionalization of Porphyrins through Organometallic Methodologies. *Chemical Reviews* **2017**, *117* (4), 2910-3043.

(87) Magdaong, N. C. M.; Taniguchi, M.; Diers, J. R.; Niedzwiedzki, D. M.; Kirmaier, C.; Lindsey, J. S.; Bocian, D. F.; Holten, D. Photophysical Properties and Electronic Structure of Zinc(II)

Porphyrins Bearing 0–4 meso-Phenyl Substituents: Zinc Porphine to Zinc Tetraphenylporphyrin (ZnTPP). *The Journal of Physical Chemistry A* **2020**, *124* (38), 7776-7794.

(88) Mandal, A. K.; Taniguchi, M.; Diers, J. R.; Niedzwiedzki, D. M.; Kirmaier, C.; Lindsey, J. S.; Bocian, D. F.; Holten, D. Photophysical Properties and Electronic Structure of Porphyrins Bearing Zero to Four meso-Phenyl Substituents: New Insights into Seemingly Well Understood Tetrapyrroles. *The Journal of Physical Chemistry A* **2016**, *120* (49), 9719-9731.

(89) Baskin, J. S.; Yu, H.-Z.; Zewail, A. H. Ultrafast Dynamics of Porphyrins in the Condensed Phase: I. Free Base Tetraphenylporphyrin. *The Journal of Physical Chemistry A* **2002**, *106* (42), 9837-9844.

(90) Yu, H.-Z.; Baskin, J. S.; Zewail, A. H. Ultrafast Dynamics of Porphyrins in the Condensed Phase: II. Zinc Tetraphenylporphyrin. *The Journal of Physical Chemistry A* **2002**, *106* (42), 9845-9854.

(91) Gurinovich, G. P.; Sevchenko, A. N.; Konstantin, N. S. e. THE SPECTROSCOPY OF THE PORPHYRINS. *Soviet Physics Uspekhi* **1963**, *6* (1), 67.

(92) Rita, G. The Use of Spectrophotometry UV-Vis for the Study of Porphyrins. In *Macro To Nano Spectroscopy*, Jamal, U. Ed.; IntechOpen, 2012; p Ch. 6.

(93) Wamser, C. C.; Ghosh, A. The Hyperporphyrin Concept: A Contemporary Perspective. *JACS Au* **2022**, *2* (7), 1543-1560.

(94) SHELNUTT, J. A. Normal-coordinate structural decomposition and the vibronic spectra of porphyrins. *Journal of Porphyrins and Phthalocyanines* **2001**, *05* (03), 300-311.

(95) Conradie, J.; Wamser, C. C.; Ghosh, A. Understanding Hyperporphyrin Spectra: TDDFT Calculations on Diprotonated Tetrakis(p-aminophenyl)porphyrin. *The Journal of Physical Chemistry A* **2021**, *125* (46), 9953-9961.

(96) Gouterman, M.; Wagnière, G. H.; Snyder, L. C. Spectra of porphyrins: Part II. Four orbital model. *Journal of Molecular Spectroscopy* **1963**, *11* (1), 108-127.

(97) Zang, L.; Che, Y.; Moore, J. S. One-Dimensional Self-Assembly of Planar π-Conjugated Molecules: Adaptable Building Blocks for Organic Nanodevices. *Accounts of Chemical Research* **2008**, *41* (12), 1596-1608.

(98) Li, Y.; Zhang, X.; Liu, D. Recent developments of perylene diimide (PDI) supramolecular photocatalysts: A review. *Journal of Photochemistry and Photobiology C: Photochemistry Reviews* **2021**, *48*, 100436.

(99) Langhals, H. Control of the Interactions in Multichromophores: Novel Concepts. Perylene Bis-imides as Components for Larger Functional Units. *Helvetica Chimica Acta* **2005**, *88* (6), 1309-1343.

(100) Spenst, P.; Würthner, F. A Perylene Bisimide Cyclophane as a “Turn-On” and “Turn-Off” Fluorescence Probe. *Angewandte Chemie International Edition* **2015**, *54* (35), 10165-10168.

(101) Li, C.; Wonneberger, H. Perylene Imides for Organic Photovoltaics: Yesterday, Today, and Tomorrow. *Advanced Materials* **2012**, *24* (5), 613-636.

(102) Weingarten, A. S.; Kazantsev, R. V.; Palmer, L. C.; McClendon, M.; Koltonow, A. R.; Samuel, A. P. S.; Kiebala, D. J.; Wasielewski, M. R.; Stupp, S. I. Self-assembling hydrogel scaffolds for photocatalytic hydrogen production. *Nature Chemistry* **2014**, *6* (11), 964-970.

(103) Minder, N. A.; Ono, S.; Chen, Z.; Facchetti, A.; Morpurgo, A. F. Band-Like Electron Transport in Organic Transistors and Implication of the Molecular Structure for Performance Optimization. *Advanced Materials* **2012**, *24* (4), 503-508.

(104) Alibert-Fouet, S.; Dardel, S.; Bock, H.; Oukachmih, M.; Archambeau, S.; Seguy, I.; Jolinat, P.; Destruel, P. Electroluminescent Diodes from Complementary Discotic Benzoperylenes. *ChemPhysChem* **2003**, *4* (9), 983-985.

(105) Kalinin, S.; Speckbacher, M.; Langhals, H.; Johansson, L. B. Å. A new and versatile fluorescence standard for quantum yield determination. *Physical Chemistry Chemical Physics* **2001**, *3* (2), 172-174, 10.1039/B007671F.

(106) Langhals, H.; Karolin, J.; B-Å. Johansson, L. Spectroscopic properties of new and convenient standards for measuring fluorescence quantum yields. *Journal of the Chemical Society, Faraday Transactions* **1998**, *94* (19), 2919-2922, 10.1039/A804973D.

(107) Würthner, F.; Osswald, P.; Schmidt, R.; Kaiser, T. E.; Mansikkamäki, H.; Könemann, M. Synthesis and Optical and Electrochemical Properties of Core-Fluorinated Perylene Bisimides. *Organic Letters* **2006**, *8* (17), 3765-3768.

(108) Zhou, W.; Liu, G.; Yang, B.; Ji, Q.; Xiang, W.; He, H.; Xu, Z.; Qi, C.; Li, S.; Yang, S.; et al. Review on application of perylene diimide (PDI)-based materials in environment: Pollutant detection and degradation. *Science of The Total Environment* **2021**, *780*, 146483.

(109) Langhals, H. Chromophores for picoscale optical computers. *Fundamentals of picoscience* **2013**, *1*.

(110) Würthner, F. Perylene bisimide dyes as versatile building blocks for functional supramolecular architectures. *Chemical Communications* **2004**, (14), 1564-1579, 10.1039/B401630K.

(111) Yan, Q.; Cai, K.; Zhao, D. Supramolecular aggregates with distinct optical properties from PDI oligomers of similar structures. *Physical Chemistry Chemical Physics* **2016**, *18* (3), 1905-1910.

(112) Li, H.; Zhang, Y.; Chen, B.; Wang, Y.; Teh, C.; Ng, G. H. B.; Meng, J.; Huang, Z.; Dong, W.; Tan, M. Y.; et al. J-Aggregation of Perylene Diimides in Silica Nanocapsules for Stable Near-Infrared Photothermal Conversion. *ACS Applied Bio Materials* **2019**, *2* (4), 1569-1577.

(113) Berera, R.; van Grondelle, R.; Kennis, J. T. Ultrafast transient absorption spectroscopy: principles and application to photosynthetic systems. *Photosynth Res* **2009**, *101* (2-3), 105-118.

(114) Dan, F.; Tong, Y.; Thomas, E. M.; Gunay, Y.; Warren, S. W., Sr. Two-color, two-photon, and excited-state absorption microscopy. *Journal of Biomedical Optics* **2007**, *12* (5), 054004.

(115) Fischer, M. C.; Wilson, J. W.; Robles, F. E.; Warren, W. S. Invited Review Article: Pump-probe microscopy. *Review of Scientific Instruments* **2016**, *87* (3), 031101.

(116) Grumstrup, E. M.; Gabriel, M. M.; Cating, E. E. M.; Van Goethem, E. M.; Papanikolas, J. M. Pump–probe microscopy: Visualization and spectroscopy of ultrafast dynamics at the nanoscale. *Chemical Physics* **2015**, *458*, 30-40.

(117) Berezin, M. Y.; Achilefu, S. Fluorescence lifetime measurements and biological imaging. *Chem Rev* **2010**, *110* (5), 2641-2684.

(118) Datta, R.; Heaster, T. M.; Sharick, J. T.; Gillette, A. A.; Skala, M. C. Fluorescence lifetime imaging microscopy: fundamentals and advances in instrumentation, analysis, and applications. *J Biomed Opt* **2020**, *25* (7), 1-43.

(119) Lakowicz, J. R. *Principles of fluorescence spectroscopy*; Springer, 2006.

(120) Ginsberg, N. S.; Tisdale, W. A. Spatially resolved photogenerated exciton and charge transport in emerging semiconductors. *Annual review of physical chemistry* **2020**, *71*, 1-30.

(121) Deng, S.; Blach, D. D.; Jin, L.; Huang, L. Imaging carrier dynamics and transport in hybrid perovskites with transient absorption microscopy. *Advanced Energy Materials* **2020**, *10* (26), 1903781.

(122) Stavrakas, C.; Delport, G.; Zhumekenov, A. A.; Anaya, M.; Chahbazian, R.; Bakr, O. M.; Barnard, E. S.; Stranks, S. D. Visualizing buried local carrier diffusion in halide perovskite crystals via two-photon microscopy. *ACS energy letters* **2019**, *5* (1), 117-123.

(123) deQuilettes, D. W.; Brenes, R.; Laitz, M.; Motes, B. T.; Glazov, M. M.; Bulović, V. Impact of photon recycling, grain boundaries, and nonlinear recombination on energy transport in semiconductors. *Acs Photonics* **2021**, *9* (1), 110-122.

(124) Thiebes, J. J.; Grumstrup, E. M. Quantifying noise effects in optical measures of excited state transport. *The Journal of Chemical Physics* **2024**, *160* (12), 124201.

(125) Bañuelos-Prieto, J.; Llano, R. S. *BODIPY Dyes: A Privilege Molecular Scaffold with Tunable Properties*; BoD–Books on Demand, 2019.

(126) Dos Santos, J. M.; Jagadamma, L. K.; Cariello, M.; Samuel, I. D. W.; Cooke, G. A BODIPY small molecule as hole transporting material for efficient perovskite solar cells. *Sustainable Energy & Fuels* **2022**, *6* (18), 4322-4330.

(127) Poddar, M.; Misra, R. Recent advances of BODIPY based derivatives for optoelectronic applications. *Coordination Chemistry Reviews* **2020**, *421*, 213462.

(128) Zhang, D.; Liu, L.; Zhang, X.; Lu, J.; Jiang, X.-D. Rational design of photofunctional dyes BODIPYs/aza-BODIPYs and applications for photocatalysis, photoelectric conversion and thermochromic materials. *Resources Chemicals and Materials* **2024**.

(129) Musser, A. J.; Rajendran, S. K.; Georgiou, K.; Gai, L.; Grant, R. T.; Shen, Z.; Cavazzini, M.; Ruseckas, A.; Turnbull, G. A.; Samuel, I. D. W.; et al. Intermolecular states in organic dye dispersions: excimers vs. aggregates. *Journal of Materials Chemistry C* **2017**, *5* (33), 8380-8389, 10.1039/C7TC02655B.

(130) Vu, T. T.; Dvorko, M.; Schmidt, E. Y.; Audibert, J.-F.; Retailleau, P.; Trofimov, B. A.; Pansu, R. B.; Clavier, G.; Méallet-Renault, R. Understanding the Spectroscopic Properties and Aggregation Process of a New Emitting Boron Dipyrromethene (BODIPY). *The Journal of Physical Chemistry C* **2013**, *117* (10), 5373-5385.

(131) Ahrens, J.; Scheja, A.; Wicht, R.; Bröring, M. Excitonic Coupling in Acyclic and Cyclic Dithioaryl-Linked BODIPY DYEmers. *European Journal of Organic Chemistry* **2016**, *2016* (16), 2864-2870.

(132) Okada, D.; Nakamura, T.; Braam, D.; Dao, T. D.; Ishii, S.; Nagao, T.; Lorke, A.; Nabeshima, T.; Yamamoto, Y. Color-Tunable Resonant Photoluminescence and Cavity-Mediated Multistep Energy Transfer Cascade. *ACS Nano* **2016**, *10* (7), 7058-7063.

(133) Mikhalyov, I.; Gretskaya, N.; Bergström, F.; Johansson, L. B. Å. Electronic ground and excited state properties of dipyrrometheneboron difluoride (BODIPY): Dimers with application to biosciences. *Physical Chemistry Chemical Physics* **2002**, *4* (22), 5663-5670, 10.1039/B206357N.

(134) Choi, S.; Bouffard, J.; Kim, Y. Aggregation-induced emission enhancement of a meso-trifluoromethyl BODIPY via J-aggregation. *Chemical Science* **2014**, *5* (2), 751-755, 10.1039/C3SC52495G.

(135) Tleugabulova, D.; Zhang, Z.; Brennan, J. D. Characterization of Bodipy Dimers Formed in a Molecularly Confined Environment. *The Journal of Physical Chemistry B* **2002**, *106* (51), 13133-13138.

(136) Sefiane, K. Patterns from drying drops. *Adv Colloid Interface Sci* **2014**, *206*, 372-381.

(137) Orte, A.; Debroye, E.; Ruedas-Rama, M. J.; Garcia-Fernandez, E.; Robinson, D.; Crovetto, L.; Talavera, E. M.; Alvarez-Pez, J. M.; Leen, V.; Verbelen, B.; et al. Effect of the substitution

position (2, 3 or 8) on the spectroscopic and photophysical properties of BODIPY dyes with a phenyl, styryl or phenylethynyl group. *RSC Advances* **2016**, *6* (105), 102899-102913.

(138) Loudet, A.; Burgess, K. BODIPY Dyes and Their Derivatives: Syntheses and Spectroscopic Properties. *Chemical Reviews* **2007**, *107* (11), 4891-4932.

(139) Oleson, A.; Zhu, T.; Dunn, I. S.; Bialas, D.; Bai, Y.; Zhang, W.; Dai, M.; Reichman, D. R.; Tempelaar, R.; Huang, L.; et al. Perylene Diimide-Based Hj- and hJ-Aggregates: The Prospect of Exciton Band Shape Engineering in Organic Materials. *The Journal of Physical Chemistry C* **2019**, *123* (33), 20567-20578.

(140) Ma, S.; Liu, Y.; Zhang, J.; Xu, B.; Tian, W. Polymorphism-Dependent Enhanced Emission in Molecular Aggregates: J-Aggregate versus X-Aggregate. *The Journal of Physical Chemistry Letters* **2020**, *11* (24), 10504-10510.

(141) Brinker, C. J.; Lu, Y.; Sellinger, A.; Fan, H. Evaporation-Induced Self-Assembly: Nanostructures Made Easy. *Advanced Materials* **1999**, *11* (7), 579-585.

(142) Garab, G.; van Amerongen, H. Linear dichroism and circular dichroism in photosynthesis research. *Photosynthesis Research* **2009**, *101* (2), 135-146.

(143) Garab, G.; Amesz, J.; Hoff, A. Biophysical techniques in photosynthesis. *Advances in Photosynthesis, eds Amesz J, Hoff AJ (Kluwer, Dordrecht, The Netherlands)* **1996**, *3*, 11-40.

(144) Harada, M.; Yatsuhashi, T.; Sakota, K. Alignment of fibrous J-aggregates and the resulting macroscopic optical anisotropy observed in static solution. *The Journal of Chemical Physics* **2024**, *160* (13), 134901.

(145) Higgins, D. A.; Reid, P. J.; Barbara, P. F. Structure and Exciton Dynamics in J-Aggregates Studied by Polarization-Dependent Near-Field Scanning Optical Microscopy. *The Journal of Physical Chemistry* **1996**, *100* (4), 1174-1180.

(146) Zhang, Y.; Yuan, S.; Liu, P.; Jing, L.; Pan, H.; Ren, X.-K.; Chen, Z. J-aggregation induced emission enhancement of BODIPY dyes via H-bonding directed supramolecular polymerization: the importance of substituents at boron. *Organic Chemistry Frontiers* **2021**, *8* (15), 4078-4085.

(147) Brown, K. E.; Salamant, W. A.; Shoer, L. E.; Young, R. M.; Wasielewski, M. R. Direct Observation of Ultrafast Excimer Formation in Covalent Perylenediimide Dimers Using Near-Infrared Transient Absorption Spectroscopy. *The Journal of Physical Chemistry Letters* **2014**, *5* (15), 2588-2593.

(148) Heckelmann, I.; Lu, Z.; Prentice, J. C. A.; Auras, F.; Ronson, T. K.; Friend, R. H.; Nitschke, J. R.; Feldmann, S. Supramolecular Self-Assembly as a Tool To Preserve the Electronic Purity of Perylene Diimide Chromophores**. *Angewandte Chemie International Edition* **2023**, *62* (12).

(149) Giaimo, J. M.; Lockard, J. V.; Sinks, L. E.; Scott, A. M.; Wilson, T. M.; Wasielewski, M. R. Excited Singlet States of Covalently Bound, Cofacial Dimers and Trimers of Perylene-3,4:9,10-bis(dicarboximide)s. *The Journal of Physical Chemistry A* **2008**, *112* (11), 2322-2330.

(150) Schubert, A.; Settels, V.; Liu, W.; Würthner, F.; Meier, C.; Fink, R. F.; Schindlbeck, S.; Lochbrunner, S.; Engels, B.; Engel, V. Ultrafast Exciton Self-Trapping upon Geometry Deformation in Perylene-Based Molecular Aggregates. *The Journal of Physical Chemistry Letters* **2013**, *4* (5), 792-796.

(151) Wan, Y.; Stradomska, A.; Knoester, J.; Huang, L. Direct Imaging of Exciton Transport in Tubular Porphyrin Aggregates by Ultrafast Microscopy. *Journal of the American Chemical Society* **2017**, *139* (21), 7287-7293.

(152) Belko, N. V.; Samtsov, M. P.; Tikhomirov, S. A.; Buganov, O. V. Ultrafast Excited-State Dynamics in Molecular Aggregates of an Indotricarbocyanine Dye. *Journal of Applied Spectroscopy* **2020**, *87* (5), 830-839.

(153) Lebedenko, A. N.; Grynyov, R. S.; Guralchuk, G. Y.; Sorokin, A. V.; Yefimova, S. L.; Malyukin, Y. V. Coherent Mechanism of Exciton Transport in Disordered J-Aggregates. *The Journal of Physical Chemistry C* **2009**, *113* (29), 12883-12887.

(154) Brixner, T.; Hildner, R.; Köhler, J.; Lambert, C.; Würthner, F. Exciton Transport in Molecular Aggregates – From Natural Antennas to Synthetic Chromophore Systems. *Advanced Energy Materials* **2017**, *7* (16), 1700236.

(155) Valleau, S.; Saikin, S. K.; Yung, M.-H.; Guzik, A. A. Exciton transport in thin-film cyanine dye J-aggregates. *The Journal of Chemical Physics* **2012**, *137* (3), 034109.

(156) Anantharaman, S. B.; Stöferle, T.; Nüesch, F. A.; Mahrt, R. F.; Heier, J. Exciton Dynamics and Effects of Structural Order in Morphology-Controlled J-Aggregate Assemblies. *Advanced Functional Materials* **2019**, *29* (21), 1806997.

(157) Hecht, M.; Würthner, F. Supramolecularly Engineered J-Aggregates Based on Perylene Bisimide Dyes. *Accounts of Chemical Research* **2021**, *54* (3), 642-653.

(158) Ginsberg, N. S.; Tisdale, W. A. Spatially Resolved Photogenerated Exciton and Charge Transport in Emerging Semiconductors. *Annual Review of Physical Chemistry* **2020**, *71* (1), 1-30.

(159) Hickey, C. L.; Grumstrup, E. M. Reduced Artifact Approach for Determining Diffusion Coefficients in Time-Resolved Microscopy. *The Journal of Physical Chemistry C* **2020**, *124* (25), 14016-14021.

(160) Aleksandr, A. I. Structure and spectral-luminescent properties of polymethine dyes. *Russian Chemical Reviews* **1991**, *60* (8), 865.

(161) Waly, S. M.; Karlsson, J. K. G.; Waddell, P. G.; Benniston, A. C.; Harriman, A. Light-Harvesting Crystals Formed from BODIPY-Proline Biohybrid Conjugates: Antenna Effects and Excitonic Coupling. *J Phys Chem A* **2022**, *126* (9), 1530-1541.

(162) La, D. D.; Jadha, R. W.; Gosavi, N. M.; Rene, E. R.; Nguyen, T. A.; Xuan-Thanh, B.; Nguyen, D. D.; Chung, W. J.; Chang, S. W.; Nguyen, X. H.; et al. Nature-inspired organic semiconductor via solvophobic self-assembly of porphyrin derivative as an effective photocatalyst for degradation of rhodamine B dye. *Journal of Water Process Engineering* **2021**, *40*, 101876.

(163) Chae, S. H.; Kim, H.; Kim, J. Y.; Kim, S.-J.; Kim, Y.; Lee, S. J. Preparation of new semiconducting tetraphenylethynyl porphyrin derivatives and their high-performing organic field-effect transistors. *Synthetic Metals* **2016**, *220*, 20-24.

(164) Payne, M. M.; Parkin, S. R.; Anthony, J. E.; Kuo, C. C.; Jackson, T. N. Organic field-effect transistors from solution-deposited functionalized acenes with mobilities as high as 1 cm2/V x s. *J Am Chem Soc* **2005**, *127* (14), 4986-4987.

(165) Ryuzaki, S.; Hasegawa, T.; Onoe, J. X-ray diffraction and infrared multiple-angle incidence resolution spectroscopic studies on the crystal structure and molecular orientation of zinc-porphyrin thin films on a SiO2/Si substrate. *Journal of Applied Physics* **2009**, *105* (11), 113529.

(166) Zeyada, H. M.; Makhlouf, M. M.; Ali, M. A. Structural, optical and dispersion properties of 5,10,15,20-tetraphenyl-21H,23H-porphyrin zinc thin films. *Japanese Journal of Applied Physics* **2016**, *55* (2), 022601.

(167) Wang, Y.-Y.; Chen, S.-M.; Haldar, R.; Wöll, C.; Gu, Z.-G.; Zhang, J. van der Waals Epitaxial Growth of 2D Metal–Porphyrin Framework Derived Thin Films for Dye-Sensitized Solar Cells. *Advanced Materials Interfaces* **2018**, *5* (21), 1800985.

(168) Friesen, B. A.; Nishida, K. R. A.; McHale, J. L.; Mazur, U. New Nanoscale Insights into the Internal Structure of Tetrakis(4-sulfonatophenyl) Porphyrin Nanorods. *The Journal of Physical Chemistry C* **2009**, *113* (5), 1709-1718.

(169) Xie, B.; Cao, Y.; Sun, J.; Yang, X.; Wang, M. Change in aggregation state of a porphyrin-perylene-diimide dyad induced by trifluoroacetic acid. *Chinese Science Bulletin* **2008**, *53* (2), 209-214.

(170) Makhlouf, M. M.; El-Denglawey, A.; Zeyada, H. M.; El-Nahass, M. M. The structural and optical characterizations of tetraphenylporphyrin thin films. *Journal of Luminescence* **2014**, *147*, 202-208.

(171) Gouterman, M. 1 - Optical Spectra and Electronic Structure of Porphyrins and Related Rings. In *The Porphyrins*, Dolphin, D. Ed.; Academic Press, 1978; pp 1-165.

(172) Nguyen, K. A.; Pachter, R. Jahn–Teller triplet excited state structures and spectra of zinc complexes of porphyrin and phthalocyanine: A density functional theory study. *The Journal of Chemical Physics* **2003**, *118* (13), 5802-5810.

(173) Dean, J. C.; Oblinsky, D. G.; Rather, S. R.; Scholes, G. D. Methylene Blue Exciton States Steer Nonradiative Relaxation: Ultrafast Spectroscopy of Methylene Blue Dimer. *The Journal of Physical Chemistry B* **2016**, *120* (3), 440-454.

(174) Chacko, J. V.; Eliceiri, K. W. Autofluorescence lifetime imaging of cellular metabolism: Sensitivity toward cell density, pH, intracellular, and intercellular heterogeneity. *Cytometry Part A* **2019**, *95* (1), 56-69.

(175) Sillen, A.; Engelborghs, Y. The Correct Use of "Average" Fluorescence Parameters. *Photochemistry and Photobiology* **1998**, *67* (5), 475-486.

(176) Kozma, E.; Catellani, M. Perylene diimides based materials for organic solar cells. *Dyes and Pigments* **2013**, *98* (1), 160-179.

(177) Root, S. E.; Savagatrup, S.; Printz, A. D.; Rodriquez, D.; Lipomi, D. J. Mechanical Properties of Organic Semiconductors for Stretchable, Highly Flexible, and Mechanically Robust Electronics. *Chemical Reviews* **2017**, *117* (9), 6467-6499.

(178) Li, G.; Zhao, Y.; Li, J.; Cao, J.; Zhu, J.; Sun, X. W.; Zhang, Q. Synthesis, Characterization, Physical Properties, and OLED Application of Single BN-Fused Perylene Diimide. *The Journal of Organic Chemistry* **2015**, *80* (1), 196-203.

(179) Korevaar, P. A.; Schaefer, C.; De Greef, T. F. A.; Meijer, E. W. Controlling Chemical Self-Assembly by Solvent-Dependent Dynamics. *Journal of the American Chemical Society* **2012**, *134* (32), 13482-13491.

(180) Herkert, L.; Droste, J.; Kartha, K. K.; Korevaar, P. A.; De Greef, T. F. A.; Hansen, M. R.; Fernández, G. Pathway Control in Cooperative vs. Anti-Cooperative Supramolecular Polymers. *Angewandte Chemie International Edition* **2019**, *58* (33), 11344-11349.

(181) Fennel, F.; Wolter, S.; Xie, Z.; Plötz, P.-A.; Kühn, O.; Würthner, F.; Lochbrunner, S. Biphasic Self-Assembly Pathways and Size-Dependent Photophysical Properties of Perylene Bisimide Dye Aggregates. *Journal of the American Chemical Society* **2013**, *135* (50), 18722-18725.

(182) Yang, D.; Ma, D. Development of Organic Semiconductor Photodetectors: From Mechanism to Applications. *Advanced Optical Materials* **2019**, *7* (1), 1800522.

(183) Troisi, A.; Orlandi, G.; Anthony, J. E. Electronic Interactions and Thermal Disorder in Molecular Crystals Containing Cofacial Pentacene Units. *Chemistry of Materials* **2005**, *17* (20), 5024-5031.

(184) Jones, A. C.; Kearns, N. M.; Ho, J.-J.; Flach, J. T.; Zanni, M. T. Impact of non-equilibrium molecular packings on singlet fission in microcrystals observed using 2D white-light microscopy. *Nature Chemistry* **2020**, *12* (1), 40-47.

(185) Illig, S.; Eggeman, A. S.; Troisi, A.; Jiang, L.; Warwick, C.; Nikolka, M.; Schweicher, G.; Yeates, S. G.; Henri Geerts, Y.; Anthony, J. E.; et al. Reducing dynamic disorder in small-molecule organic semiconductors by suppressing large-amplitude thermal motions. *Nature Communications* **2016**, *7* (1), 10736.

(186) Wong, C. Y.; Cotts, B. L.; Wu, H.; Ginsberg, N. S. Exciton dynamics reveal aggregates with intermolecular order at hidden interfaces in solution-cast organic semiconducting films. *Nature Communications* **2015**, *6* (1), 5946.

(187) Würthner, F. Perylene bisimide dyes as versatile building blocks for functional supramolecular architectures. *Chem. Commun.* **2004**, (14), 1564-1579.

(188) Würthner, F.; Saha-Möller, C. R.; Fimmel, B.; Ogi, S.; Leowanawat, P.; Schmidt, D. Perylene Bisimide Dye Assemblies as Archetype Functional Supramolecular Materials. *Chemical Reviews* **2016**, *116* (3), 962-1052.

(189) Görl, D.; Zhang, X.; Stepanenko, V.; Würthner, F. Supramolecular block copolymers by kinetically controlled co-self-assembly of planar and core-twisted perylene bisimides. *Nature Communications* **2015**, *6* (1), 7009.

(190) Chen, S.; Slattum, P.; Wang, C.; Zang, L. Self-Assembly of Perylene Imide Molecules into 1D Nanostructures: Methods, Morphologies, and Applications. *Chem Rev* **2015**, *115* (21), 11967-11998.

(191) Boobalan, G.; Imran, P. M.; Ramkumar, S. G.; Nagarajan, S. Fabrication of luminescent perylene bisimide nanorods. *Journal of Luminescence* **2014**, *146*, 387-393.

(192) Wilson-Kovacs, R. S.; Fang, X.; Hagemann, M. J. L.; Symons, H. E.; Faul, C. F. J. Design and Control of Perylene Supramolecular Polymers through Imide Substitutions. *Chemistry – A European Journal* **2022**, *28* (3), e202103443.

(193) Wehner, M.; Würthner, F. Supramolecular polymerization through kinetic pathway control and living chain growth. *Nature Reviews Chemistry* **2019**, *4* (1), 38-53.

(194) Volek, T. S.; Armstrong, Z. T.; Sowa, J. K.; Wilson, K. S.; Bohlmann Kunz, M.; Bera, K.; Koble, M.; Frontiera, R. R.; Rossky, P. J.; Zanni, M. T.; et al. Structural Disorder at the Edges of Rubrene Crystals Enhances Singlet Fission. *J Phys Chem Lett* **2023**, *14* (50), 11497-11505.

(195) Zhang, M.; Zheng, Z.; Fu, Q.; Chen, Z.; He, J.; Zhang, S.; Yan, L.; Hu, Y.; Luo, W. Growth and characterization of all-inorganic lead halide perovskite semiconductor CsPbBr3 single crystals. **2017**.

(196) Paulino, V.; Cadena, D. M.; Liu, K.; Mukhopadhyay, A.; Roberts, S. T.; Olivier, J.-H. The Length of Molecular Tethers Can Be Used to Control the Structure and Electronic Properties of Stapled Supramolecular Polymers. *Chemistry of Materials* **2022**, *34* (14), 6518-6528.

(197) Ashcraft, A.; Liu, K.; Mukhopadhyay, A.; Paulino, V.; Liu, C.; Bernard, B.; Husainy, D.; Phan, T.; Olivier, J. H. A Molecular Strategy to Lock-in the Conformation of a Perylene Bisimide-Derived Supramolecular Polymer. *Angewandte Chemie International Edition* **2020**, *59* (19), 7487-7493.

(198) Sliz, R.; Czajkowski, J.; Fabritius, T. Taming the Coffee Ring Effect: Enhanced Thermal Control as a Method for Thin-Film Nanopatterning. *Langmuir* **2020**, *36* (32), 9562-9570.

(199) Diao, Y.; Shaw, L.; Bao, Z.; Mannsfeld, S. C. B. Morphology control strategies for solution-processed organic semiconductor thin films. *Energy Environ. Sci.* **2014**, *7* (7), 2145-2159.

(200) Liu, S.-G.; Sui, G.; Cormier, R. A.; Leblanc, R. M.; Gregg, B. A. Self-Organizing Liquid Crystal Perylene Diimide Thin Films: Spectroscopy, Crystallinity, and Molecular Orientation. *The Journal of Physical Chemistry B* **2002**, *106* (6), 1307-1315.

(201) Belova, V.; Wagner, B.; Reisz, B.; Zeiser, C.; Duva, G.; Rozbořil, J.; Novák, J.; Gerlach, A.; Hinderhofer, A.; Schreiber, F. Real-Time Structural and Optical Study of Growth and Packing Behavior of Perylene Diimide Derivative Thin Films: Influence of Side-Chain Modification. *The Journal of Physical Chemistry C* **2018**, *122* (15), 8589-8601.

(202) Zhang, F.; Ma, Y.; Chi, Y.; Yu, H.; Li, Y.; Jiang, T.; Wei, X.; Shi, J. Self-assembly, optical and electrical properties of perylene diimide dyes bearing unsymmetrical substituents at bay position. *Scientific Reports* **2018**, *8* (1).

(203) Zugenmaier, P.; Duff, J.; Bluhm, T. L. Crystal and Molecular Structures of Six Differently with Halogen Substituted Bis (benzylimido) perylene. *Crystal Research and Technology* **2000**, *35* (9), 1095-1115.

(204) Hadicke, E.; Graser, F. Structures of eleven perylene-3,4:9,10-bis(dicarboximide) pigments. *Acta Crystallographica Section C* **1986**, *42* (2), 189-195.

(205) Davydova, D. y.; de la Cadena, A.; Akimov, D.; Dietzek, B. Transient absorption microscopy: advances in chemical imaging of photoinduced dynamics. *Laser & Photonics Reviews* **2016**, *10* (1), 62-81.

(206) Fischer, M. C.; Wilson, J. W.; Robles, F. E.; Warren, W. S. Invited Review Article: Pump-probe microscopy. *Rev Sci Instrum* **2016**, *87* (3), 031101.

(207) Huang, L.; Wong, C.; Grumstrup, E. Time-Resolved Microscopy: A New Frontier in Physical Chemistry. *The Journal of Physical Chemistry A* **2020**, *124* (29), 5997-5998.

(208) Piland, G.; Grumstrup, E. M. High-Repetition Rate Broadband Pump–Probe Microscopy. *The Journal of Physical Chemistry A* **2019**, *123* (40), 8709-8716.

(209) Dean, J. C.; Oblinsky, D. G.; Rafiq, S.; Scholes, G. D. Methylene Blue Exciton States Steer Nonradiative Relaxation: Ultrafast Spectroscopy of Methylene Blue Dimer. *The Journal of Physical Chemistry B* **2016**, *120* (3), 440-454.

(210) Verma, S.; Ghosh, A.; Das, A.; Ghosh, H. N. Ultrafast Exciton Dynamics of J- and H-Aggregates of the Porphyrin-Catechol in Aqueous Solution. *The Journal of Physical Chemistry B* **2010**, *114* (25), 8327-8334.

(211) Kakade, S.; Ghosh, R.; Palit, D. K. Excited State Dynamics of Zinc–Phthalocyanine Nanoaggregates in Strong Hydrogen Bonding Solvents. *The Journal of Physical Chemistry C* **2012**, *116* (28), 15155-15166.

(212) Caplins, B. W.; Mullenbach, T. K.; Holmes, R. J.; Blank, D. A. Intermolecular Interactions Determine Exciton Lifetimes in Neat Films and Solid State Solutions of Metal-Free Phthalocyanine. *The Journal of Physical Chemistry C* **2015**, *119* (49), 27340-27347.

(213) Vauthey, E. Photoinduced Symmetry-Breaking Charge Separation. *ChemPhysChem* **2012**, *13* (8), 2001-2011.

(214) Koch, M.; Myahkostupov, M.; Oblinsky, D. G.; Wang, S.; Garakyaraghi, S.; Castellano, F. N.; Scholes, G. D. Charge Localization after Ultrafast Photoexcitation of a Rigid Perylene Perylenediimide Dyad Visualized by Transient Stark Effect. *Journal of the American Chemical Society* **2017**, *139* (15), 5530-5537.

(215) Leonhardt, H.; Weller, A.

(216) Sundström, V.; Gillbro, T. Excited state dynamics and photophysics of aggregated dye chromophores in solution. *The Journal of Chemical Physics* **1985**, *83* (6), 2733-2743.

(217) Zhu, T.; Wan, Y.; Huang, L. Direct Imaging of Frenkel Exciton Transport by Ultrafast Microscopy. *Accounts of Chemical Research* **2017**, *50* (7), 1725-1733.

(218) Pandya, R.; Chen, R. Y. S.; Gu, Q.; Gorman, J.; Auras, F.; Sung, J.; Friend, R.; Kukura, P.; Schnedermann, C.; Rao, A. Femtosecond Transient Absorption Microscopy of Singlet Exciton Motion in Side-Chain Engineered Perylene-Diimide Thin Films. *The Journal of Physical Chemistry A* **2020**, *124* (13), 2721-2730.

(219) Miller, A.; Abrahams, E. Impurity Conduction at Low Concentrations. *Physical Review* **1960**, *120* (3), 745-755.

(220) Geng, Y.; Li, H.-B.; Wu, S.-X.; Su, Z.-M. The interplay of intermolecular interactions, packing motifs and electron transport properties in perylene diimide related materials: a theoretical perspective. *Journal of Materials Chemistry* **2012**, *22* (39), 20840.

(221) Balzer, D.; Smolders, T.; Blyth, D.; Hood, S. N.; Kassal, I. Delocalised kinetic Monte Carlo for simulating delocalisation-enhanced charge and exciton transport in disordered materials. *Chem Sci* **2020**, *12* (6), 2276-2285.

(222) Mesta, M.; Carvelli, M.; de Vries, R. J.; van Eersel, H.; van der Holst, J. J. M.; Schober, M.; Furno, M.; Lüssem, B.; Leo, K.; Loebl, P.; et al. Molecular-scale simulation of electroluminescence in a multilayer white organic light-emitting diode. *Nature Materials* **2013**, *12* (7), 652-658.

(223) Kaiser, W.; Popp, J.; Rinderle, M.; Albes, T.; Gagliardi, A. Generalized Kinetic Monte Carlo Framework for Organic Electronics. *Algorithms* **2018**, *11* (4), 37.

(224) Groves, C. Simulating charge transport in organic semiconductors and devices: a review. *Reports on Progress in Physics* **2017**, *80* (2), 026502.

(225) Pandya, R.; Chen, R. Y. S.; Gu, Q.; Gorman, J.; Auras, F.; Sung, J.; Friend, R.; Kukura, P.; Schnedermann, C.; Rao, A. Femtosecond Transient Absorption Microscopy of Singlet Exciton Motion in Side-Chain Engineered Perylene-Diimide Thin Films. *J Phys Chem A* **2020**, *124* (13), 2721-2730.